8-2018

Computational Fluid Dynamic Modeling of Catalytic Hydrous Pyrolysis of Biomass to Produce Refinery-Ready Bio-Crude Oil

Ross Wesley Houston
University of Tennessee, rhousto2@vols.utk.edu

Recommended Citation

Houston, Ross Wesley, "Computational Fluid Dynamic Modeling of Catalytic Hydrous Pyrolysis of Biomass to Produce Refinery-Ready Bio-Crude Oil. " Master's Thesis, University of Tennessee, 2018.
https://trace.tennessee.edu/utk_gradthes/5122

To the Graduate Council:

I am submitting herewith a thesis written by Ross Wesley Houston entitled "Computational Fluid Dynamic Modeling of Catalytic Hydrous Pyrolysis of Biomass to Produce Refinery-Ready Bio-Crude Oil." I have examined the final electronic copy of this thesis for form and content and recommend that it be accepted in partial fulfillment of the requirements for the degree of Master of Science, with a major in Biosystems Engineering.

Nourredine H. Abdoulmoumine, Major Professor

We have read this thesis and recommend its acceptance:

Douglas G. Hayes, Nicole Labbe

Accepted for the Council:
Dixie L. Thompson

Vice Provost and Dean of the Graduate School

(Original signatures are on file with official student records.)

Computational Fluid Dynamic Modeling of Catalytic Hydrous Pyrolysis of Biomass to Produce Refinery-Ready Bio-Crude Oil

A Thesis Presented for the
Master of Science
Degree
The University of Tennessee, Knoxville

Ross Wesley Houston
August 2018

ACKNOWLEDGMENTS

I would like to thank my advisors Dr. Nourredine Abdoulmoumine and Dr. Nicole Labbé for everything they have done to help me as I pursued my Master’s degree. Thank you to Dr. Robert Burns, Dr. Neal Schrick, and Dr. Caula Beyl for encouraging me to pursue graduate school and, in turn, helping start this journey. Thank you to the members of my research group with special thanks to Oluwafemi Oyedeji for his continued support in the modeling aspect of my project. Thank you also to Dr. Stuart Daw and his research group at the National Transportation Research Center at ORNL for their collaboration with our group.

I also want to thank the United States Department of Agriculture (USDA) Agriculture and Food Research Initiative for providing the funding for this research.

ABSTRACT

The growing world population continually increases the demand for energy. Currently, the main source of energy production is fossil fuels, which are harmful to the environment and are finite. An exploration of renewable energy to supplement or replace fossil fuels is of great importance. Modern techniques for producing renewable bio-oil consist of converting biomass into bio-oil through pyrolysis, but unfortunately, pyrolysis oil has quality issues (e.g., high oxygen content, viscosity, chemical instability). Therefore, upgrading is necessary to improve quality. Hydropyrolysis is a state of the art technique to deoxygenate bio-oil during pyrolysis to produce petroleum quality bio-oil. A major issue with hydropyrolysis is the expensive cost of hydrogen.

This project aimed to computationally model the hydrous pyrolysis of biomass coupled with an *in-situ* hydrogen generation process. The kinetics of the water-gas shift (WGS) were determined experimentally and modeled using an ordinary differential equation subroutine coupled with a nonlinear regression. A computational fluid dynamic (CFD) model of biomass fast pyrolysis was developed to simulate conventional fast pyrolysis. The final part of this project adapted the CFD model to simulate hydrous pyrolysis and incorporate the determined WGS kinetics. The bio-oil was deoxygenated via a global lumped hydrodeoxygenation (HDO) kinetic scheme.

This WGS was determined to have an agreement with both an empirical power law and a Langmuir-Hinselwood mechanism at conditions similar to that of pyrolysis. The CO conversion reached a maximum value of 94% at higher temps and larger amounts of catalyst. The CFD model of fast pyrolysis predicted a maximum bio-oil yield of 47%, but significantly under-predicted the amount of water present in the oil. The hydrous pyrolysis simulations have not yet reached steady-state and the HDO reactions are just beginning to take place. Further work is needed to explore

more detailed kinetic schemes for the secondary pyrolysis reactions as well as the hydrodeoxygenation kinetics.

TABLE OF CONTENTS

LIST OF TABLES

LIST OF FIGURES

ABBREVIATIONS AND SYMBOLS

H/C	Hydrogen to carbon ratio
O/C	Oxygen to carbon ratio
S/C	Steam to CO molar ratio
CO_2	Carbon dioxide
CO	Carbon monoxide
Cu	Copper
H_2	Hydrogen
H_2O	Water
CH_4	Methane
N_2	Nitrogen
He	Helium
CuO	Copper oxide
ZnO	Zinc oxide
Al_2O_3	Aluminum oxide
BET	Brunauer-Emmett-Teller
TCD	Thermal conductivity detector
FID	Flame ionization detector
FPD	Flame photometric detector
TAN	Total acid number
CFP	Catalytic fast pyrolysis
HDO	Hydrodeoxygenation
GTI	Gas Technology Institute
WGS	Water-gas shift
CFD	Computational fluid dynamics
NiMo	Nickel-Molybdenum
$CoMo/Al_2O_3$	Cobalt-Molybdenum/Aluminum Oxide
TFM	Two-fluid model
DEM	Discrete element method
UDF	User defined function
HTS	High temperature shift
ITS	Intermediate temperature shift
LTS	Low temperature shift
LH	Langmuir-Hinshelwood
ER	Eley-Rideal
TPR	Temperature programreduction
TGA	Thermogravimetric analyzer
DTG	Differential thermogravimetric
PFR	Plug flow reactor
PID	Proportional integral derivative
SV	Space velocity
WHSV	Weight hourly space velocity
ROM	Reduced order model
RMSE	Root mean squared error
MAE	Mean absolute error

FIT	Goodness of fit
AIC	Akaike Information Criterion
α_g/α_{sm}	Gas/Solid phase volume fraction
ρ_g/ρ_{sm}	Material density
U_g	Gas velocity vector
R_g/R_{sm}	Mass transfer source term
τ_g/τ_{sm}	Stress tensor
p	Pressure
β_{gsm}	Gas-solid inter-phase momentum exchange coefficient
β_{slm}	Momentum exchange coefficient between solid phase *l* and *m*
U_{sm}/U_{sl}	Solid phase velocity
ψ_{gsm}	Gas-solid momentum exchange due to mass transfer
g	Gravity vector
C_{pg}/C_{psm}	Heat capacity
T_g/T_{sm}	Temperature of the gas phase
q_g/q_{sm}	Conductive heat flux
h_{gsm}	Gas-solid heat transfer coefficient
ΔH_g	Heat of reactions in the gas phase
Y_{gk}/Y_{smk}	Mass fraction of species k in the each phase
R_{gk}/R_{smk}	Reaction rate of species k in the each phase
t	Time
k	Reaction rate constant
k_0	Pre-exponential constant
E_a	Activation energy
R	Gas constant
T	Temperature
m_i	Mass of particle *i*
v_i	Translational velocity of particle *i*
F_{ij}^{c}	Contact force acting on particle *i* by particle *j* or walls
F_{ik}^{nc}	Non-contact force acting on particle *i* by particle *k* or other sources
F_i^{f}	Particle-fluid interaction force on particle *i*
F_i^{g}	Gravitational force
I_i	Moment of inertia
ω_i	Angular velocity of particle *i*
M_{ij}	Torque acting on particle *i* by particle *j* or walls
ε_g	Gas volume fraction
ρ_g	Gas density
ρ_p	Particle density
m_p	Mass of particle
$\boldsymbol{U}_g$	Gas velocity
S_p	Mass source term
$\boldsymbol{\tau}$	Gas effective stress tensor
$\boldsymbol{g}$	Gravitational vector
S_m	Momentum source term
E	Energy

h_s	Sensible energy
p	Pressure
S_h	Reaction enthalpy source term
$S_{p,h}$	Particle enthalpy source term
S_r	Radiation source term
α_e	Effective dynamic thermal diffusivity
r_{CO}^{obs}	Observed reaction rate
ρ_c	Catalyst density
a'	Specific external surface area of catalyst
k_f	Mass transfer coefficient
C_{CO}^{b}	CO concentration in the bulk phase
R_p	Mean radius of the catalyst particle
C_{As}	CO concentration at the catalyst surface
D_e	Mass Diffusion Constant
D	Diffusion coefficient
φ_p	Porosity of the catalyst particle
σ	Constriction factor
τ	Tortuosity
X	Conversion of CO
$P_i{}^{j}$	Partial pressure of species i, raised to j
β_e	Approach to equilibrium
K_e	Equilibrium constant
N	Number of observations
k	Number of parameters being optimized
y_i	Experimental data
$\text{experimental}_{\text{max}}$	Maximum observed value
$F(k, x_i)$	Values calculated by the model
CO_0	Initial CO concentration
θ	Stoicheometric ratio between steam and CO
K_i	Adsorption constant for species *i*
ΔH_i	Heat of adsorption for species *i*
Y_i	Chemical species mass fraction
S_{p,Y_i}	Particle species source term
S_{Y_i}	Reaction Species Source
μ_g	Gas phase viscosity
μ_t	Turbulent viscosity
I	Identity vector
σ	Turbulent dissipation rate
k	Turbulent energy
C_μ	Empirically constant (Value used is 0.09)
β	Moment exchange
d_p	Particle diameter
$\boldsymbol{U}_p$	Particle velocity
ε_p	Solid volume fraction

C_d	Drag coefficient
Re_p	Reynolds number
h	Heat transfer constant
$\propto_p$	Particle volume fraction
k_g	Thermal conductivity
Nu_p	Nusselt number
Pr	Prandtl number
C_{pg}	Gas heat capacity
$F_{contact}$	Total contact force on a particle
F_n	Normal force on a particle
F_t	Tangential force on a particle

INTRODUCTION

Background

The rapidly growing world population has resulted in a boom in energy demand while the main source of energy, fossil fuels, is a finite resource and will be depleted in the future [1,2]. Shaifee et al., [3] derived a formula from the Klass[4] model to project coal reserves to last until 2112. This dilemma has recently motivated an ever-increasing interest in renewable energy to counter this issue. In turn, interest has led to the exploration of alternative methods to produce fuel, energy, and chemicals from lignocellulosic biomass. Lignocellulosic biomass is the most abundant renewable resource in the U.S. with a net zero carbon dioxide (CO_2) addition into the atmosphere. These materials are readily available and come from a wide range of sources including forest products, agricultural wastes, forest residues, and energy crops. There are several processes (e.g., pyrolysis, torrefaction, gasification, and combustion) available for biomass conversion that produce a form of renewable energy. To maximize the production of bio-oil, pyrolysis is a low-cost, efficient way to convert the biomass. Pyrolysis is the thermal decomposition of biomass by heating in an oxygen-free environment to produce biochar, syngas, and bio-oil. Pyrolysis takes place in one of two ways: slow or fast pyrolysis. Fast pyrolysis is more efficient at producing liquid bio-oil, while slow pyrolysis is more useful for applications such as charcoal production. Conventional fast pyrolysis does not produce liquid bio-oil of quality comparable to that of crude oil, so the vapors must be further processed to improve quality. Catalytic fast pyrolysis (CFP) is essentially conventional fast pyrolysis with the presence of a suitable catalyst. CFP can be designed for *in-situ* or *ex-situ* upgrading to remove many of the reactive and oxidized components of the pyrolysis vapors. This method tends to be expensive due to major issues with catalyst coking and deactivation. Another advanced pyrolysis process that improves the quality of bio-oil is hydropyrolysis. Hydropyrolysis combines pyrolysis with hydrodeoxygenation (HDO) to upgrade pyrolysis vapors to a quality comparable to that of petroleum. Hydropyrolysis requires a HDO catalyst and an adequate supply of hydrogen. Hydropyrolysis is the state-of-the-art advanced pyrolysis process, which is very promising but there are issues that must be addressed.

Biomass fast pyrolysis is a very complex process due to the variable composition of biomass as well as the typical fluidized bed reactor environment. The nature of the reaction makes it difficult to monitor the transport phenomena occurring inside the fluidizied bed reactor. Therefore, computational fluid dynamics (CFD) modelling has recently gained attention as an avenue to investigate and understand the complex reaction environment. This research aims to utilize CFD to model the hydropyrolysis of biomass to produce high quality bio-oil

Problem statement

Bio-oil produced from the pyrolysis of lignocellulosic biomass is not compatible for co-processing in existing petroleum refineries. The bio-oil has several quality issues in comparison to petroleum crude oil, such as high oxygen content, chemical instability, and high total acid number (TAN)[5]. To be able to co-process the bio-oil in a petroleum refinery, pyrolysis bio-oil must undergo further upgrading through either a downstream process or a more advanced pyrolysis process such as catalytic fast pyrolysis or hydropyrolysis. The main issue associated with bio-oil quality is the high oxygen content. Many of the other quality issues stem from the high oxygen content. Oxygenated groups in the bio-oil tend to be more reactive and will gradually polymerize and increase viscosity. The more oxygenated the bio-oil is, the less volatile it will be, which greatly affects distillation and leads to coking. The two most common advanced pyrolysis processes for decreasing bio-oil oxygen content are CFP and hydropyrolysis, which will be discussed in detail later in the proposal. Both processes can remove a significant amount of oxygen from the bio-oil;

however, there are still issues present with each process. CFP has significant issues with catalyst coking and deactivation. Hydropyrolysis is the most effective upgrading process; however, the hydrogen requirement can significantly reduce the economic viability due to the high price of hydrogen.

Research proposal and objectives

The goal of this research is to develop a one-pot solution to produce hydrogen using steam and deoxygenate pyrolysis vapors simultaneously through a new process that will be coined as "hydrous pyrolysis." Current hydropyrolysis processes supply hydrogen to the system to deoxygenate pyrolysis vapors. Hydrous pyrolysis integrates water-gas shift (WGS), hydrodeoxygenation (HDO), and fast pyrolysis with the goal of oxygen removal and hydrocarbon-rich biocrude production. Concretely, an integrated hydrous pyrolysis process in a fluidized bed reactor predominantly employs steam for fluidization as well as to produce hydrogen *in-situ* using carbon monoxide generated by fast pyrolysis. The hydrogen produced *in-situ* is subsequently used to carry out HDO. At the end, water generated through HDO and unreacted steam are separated and recycled thus creating a net-zero water process. The central hypothesis is that steam and the most abundant non-condensable pyrolysis vapor, CO, will produce sufficient hydrogen to deoxygenate condensable pyrolysis vapors in the presence of a hydrodeoxygenation catalyst (sulfided $CoMo/Al_2O_3$) at high pressures. The overall goal of this research will be accomplished through the following three objectives:

Objective 1. To determine the kinetics of hydrogen production on commonly used commercial water-gas shift (WGS) shift catalyst at pyrolysis operating conditions;

Objective 2. To model fast pyrolysis using constitutive pyrolysis kinetic model integrated into a discrete element (DEM) framework.

Objective 3. To integrate hydrodeoxygenation (HDO) reaction kinetics and operating conditions to the fast pyrolysis DEM framework.

Our research objectives are supported by several hypotheses which will guide our experimental approaches and our numerical simulations. These hypotheses are as follow:

Hypothesis 1 (Objective 1): I hypothesize that the WGS is sufficient enough to produce adequate hydrogen for hydrous pyrolysis using carbon monoxide (CO), the most abundant noncondensable gas product of biomass pyrolysis.

Hypothesis 2. (Objective 2): I hypothesize that a computational fluid dynamic model, with a discrete element method, (CFD-DEM) incorporating an extensive reaction scheme is able to model biomass pyrolysis in a bubbling fluidized bed reactor.

Hypothesis 3 (Objective 3): I hypothesize that including the kinetics derived in Objective 1 and secondary HDO kinetics into the CFD-DEM from Objective 2 will model a one-pot hydrous pyrolysis reactor to produce refinery-ready bio-oil.

List of references

(1) Hoel, M.; Kverndokk, S. Depletion of fossil fuels and the impacts of global warming. *Resource and Energy Economics* **1996,** *18* (2), 115.

(2) Withagen, C. Pollution and exhaustibility of fossil fuels. *Resource and Energy Economics* **1994,** *16* (3), 235.

(3) Shafiee, S.; Topal, E. When will fossil fuel reserves be diminished? *Energy Policy* **2009,** *37* (1), 181.

(4) Klass, D. L. *Biomass for Renewable Energy, Fuels, and Chemicals*; Elsevier Science, 1998.

(5) Marker, T. L.; Felix, L. G.; Linck, M. B.; Roberts, M. J.; Ortiz-Toral, P.; Wangerow, J. Integrated hydropyrolysis and hydroconversion (IH2®) for the direct production of gasoline and diesel fuels or blending components from biomass, part 2: Continuous testing. *Environmental Progress & Sustainable Energy* **2014,** *33* (3), 762.

CHAPTER 1 LITERATURE REVIEW

1.1. Introduction

Adequate energy supply continues to be of great importance due to the increasing population and energy consumption throughout the world. Currently, most of the energy consumption worldwide is from fossil fuels, which contribute to greenhouse gas emissions. Therefore, sustainable, renewable energy sources are being investigated to reduce our dependence on fossil fuels, meet increasing energy demands, and help mitigate the anthropogenic contribution to climate change. Biomass has been viewed as an attractive renewable alternative to fossil fuels and is the most widely used type of renewable energy. Biomass sources contribute to approximately 10% of the global energy demand[1,2]. There are two main types of biomass conversion techniques to produce energy: biochemical and thermochemical. Biochemical conversion uses biological agents to breakdown the biomass or biomass intermediates into various products at mild temperatures. Examples of biochemical conversion processes include anaerobic digestion to produce biogas that can be burned for heat, and fermentation of biomass derived sugars to produce either ethanol or butanol[3]. In contrast, thermochemical conversion uses high temperatures with or without a catalyst to convert biomass into intermediates with higher energy density[4]. The primary thermochemical conversion techniques are combustion, gasification, and pyrolysis. These processes differ by their operating temperature range and oxygen requirements. Fast pyrolysis is carried out at moderate temperatures (400-600 °C) in the absence of oxygen; gasification occurs at higher temperatures (650-1000 °C) in a sub-stoichiometric amount of oxygen, and combustion takes places at very high temperatures (>1100 °C) with oxygen in stoichiometric excess. Fast pyrolysis is the most efficient of the thermochemical conversion processes and is seen as the most attractive biomass conversion technique because of the potential to directly produce a liquid transportation fuel with typical yields between 50-70 wt. %[5-7].

1.2. Biomass fast pyrolysis

Fast pyrolysis is simply the decomposition of organic materials at moderate temperatures in the absence of oxygen. It is characterized by high heating rates, carefully controlled temperatures in the range of 400-600 °C, atmospheric pressures, and rapid cooling of the vapors to produce liquid bio-oil, which is the primary product from fast pyrolysis. Typical product yields are 60-75 wt. % bio-oil, 15-25 wt. % char, and 10-20 wt. % non-condensable gases[8]. Generally, bio-oil is made up organic and aqueous fractions. One of the most important characteristics of fast pyrolysis is its vapor residence time, generally requiring a short residence time of fewer than two seconds (< 2 s). For lignocellulosic biomass, comprised of lignin, cellulose, and hemicellulose, the rate and extent of decomposition is dependent on the process parameters, such as temperature and residence time[9]. The product yield of liquid bio-oil is reliant on the extent of secondary reactions, which primarily depends on the residence time. The longer the vapors stay in the reactor, the more they are subject to secondary cracking to produce smaller, non-condensable gases and reduce the overall liquid bio-oil yield. The optimum residence time to maximize bio-oil production was found to be 0.2-0.6 s for most biomass materials[10]. Temperature is also an important parameter to control when optimizing the bio-oil yield. Organic liquid oil yields are maximized in the temperature range of 400-500 °C[9].

Biomass fast pyrolysis can be carried out in several reactor configurations such as a bubbling fluidized bed reactor (BFBR), circulating fluidized bed reactor (CFBR), ablative reactor, and an auger reactor[11]. Fluidized bed reactors provide stable temperature control, efficient heat transfer to the biomass particles, and produce high liquid bio-oil yields. However, regardless of the reactor configuration, fast pyrolysis always produces three products: char, non-condensable gases, and liquid bio-oil.

Bio-oil produced from fast pyrolysis is typically a dark brown liquid with a strong, smoky smell. While it is considered a bio-based alternative to crude petroleum, its chemical composition is significantly different leading to substantial differences in properties and characteristics. For example, unlike crude petroleum which is composed mainly of paraffins and aromatics, bio-oil is made up of highly oxygenated compounds, such as hydroxyaldehydes, phenolics, and acids.[6,12] Its most abundant component is water with concentrations of 15-30 wt. %[13]. However, the most problematic issue with bio-oil is the presence of oxygen[14]. Oxygen can be found within almost all of the different components of bio-oil, which is the primary reason for the significant differences between bio-oil and petroleum properties. These differences such as high oxygen content, chemical instability, a high total acid number (TAN) make it very difficult to co-process bio-oil alongside crude petroleum [15]. Table 1.1 shows a comparison of the characteristics of conventional bio-oil and crude oil, which further shows the disparity between fast pyrolysis bio-oil and crude oil.

1.3. Pyrolysis upgrading

Due to the issues associated with the bio-oil produced through conventional fast pyrolysis, catalytic fast pyrolysis (CFP) has been looked at to upgrade the pyrolysis vapors using a suitable catalyst. The main purpose of CFP is to remove the oxygen from the pyrolysis vapors as oxygen leads to most of the main issues associated with bio-oil[16]. Catalytic fast pyrolysis can be carried out either *in-situ* (catalyst is mixed in directly with the biomass feedstock) or *ex-situ* (catalyst is only in contact with the hot pyrolysis vapors)[17]. Testing conventional and catalytic fast pyrolysis side by side has shown catalytic fast pyrolysis to produce more aromatic hydrocarbons and reduce

Table 1.1. Comparison of conventional bio-oil and crude oil characteristics. Adapted from Dickerson and Soria.[12]

Composition (wt. %)	Bio-oil	Crude Oil
Water	15-30	0.1
C	55-65	83-86
O	58-40	<1
H	5-7	11-14
Ash	<0.2	0.1
H/C (ratio)	0.9-1.5	1.5-2.0

the oxygen content to less than 15 wt. %[15,18]. Yildiz et al. found using a catalyst during fast pyrolysis significantly improved the oxygen removal from bio-oil compared to conventional fast pyrolysis; however, CFP also decreased the total yield of liquid bio-oil and increased the production of char and gas[19]. Due to the complex composition of pyrolysis bio-oil, the necessary upgrading is difficult to achieve in a single technique. The two main pathways for catalytic upgrading are zeolite cracking and hydrodeoxygenation (HDO).

1.3.1. Zeolite cracking

Zeolites are porous oxide structures with a defined pore structure due to high crystallinity. H-ZSM5 is an established zeolite catalyst used to deoxygenate bio-oil[20]. Zeolite cracking is used to remove oxygen from bio-oil to produce hydrocarbons. Cracking breaks the carbon-carbon bonds and releases oxygen in the form of carbon dioxide (CO_2) and water (H_2O) through dehydration, decarboxylation, and decarbonylation.[21,22] An overall, empirical reaction for zeolite cracking of bio-oil can be represented by[23]:

$$C_6H_8O_4 \rightarrow 4.6CH_{1.2} + 1.4CO_2 + 1.2H_2O$$

Zeolite cracking produces aromatics from the oxygenated bio-oil compounds. Due to the aromatic nature of the oil, cracking produces a product with a lower heating value than HDO[12]. The oil is generally thought to have more potential as a chemical feedstock than that produced by HDO[23]. Typical operating temperatures for zeolite cracking range from 350-600 °C. One of the advantages of zeolite cracking is there is no hydrogen requirement as it is carried out at atmospheric pressures. However, there are major issues associated with zeolite cracking. Cracking leads to excessive coke formation on the catalyst site, which then leads to catalyst deactivation[24]. The overall bio-oil yields are drastically reduced upon zeolite cracking. Actual yields from zeolite cracking range from 15-23%[25].

1.3.2. Hydrodeoxygenation

In HDO, hydrogen is introduced to the system at high pressure (up to 200 bar) and the process takes place at moderate temperatures (300-600 °C). Oxygen is removed in the form of H_2O, and occasionally CO_2. Hydrodeoxygenation consists of several different types of reactions such as hydrogenation, cracking, and decarboxylation[26]. However, the most prominent reaction is described by[22,27]:

$$(CH_2O) + H_2 \rightarrow (CH_2) + H_2O$$

Significant work has been done on development and testing of catalysts for HDO. Transition metal sulfides have shown to provide good results when used as the active catalyst, with Ni-Mo and Co-Mo supported on Al_2O_3 are the most widely used catalysts in HDO[27-29]. Due to the sulfur component of these catalysts, sulfur stripping occurs during HDO and leads to catalyst deactivation[30]. Bio-oil has a large oxygen content that could contribute to accelerated catalyst deactivation compared to other HDO applications[31].

Compared to the oil upgraded through zeolite cracking, HDO treated oil has more of a naphtha-like composition and is more energy dense[12]. Water is produced during HDO, which leads to the final liquid product consisting of two phases: aqueous and organic. The O/C ratio in the organic phase after HDO is much lower than the O/C of pyrolysis bio-oil[32]. The organic and aqueous phases are easy to separate upon full hydrodeoxygenation. The maximum liquid yield that can be produced from the complete deoxygenation of pyrolysis oil, based off stoichiometry, is 56-58%[25,33]. However, complete deoxygenation is not always achieved due to the inherit complexity of the HDO process. The extent of deoxygenation is dependent on the residence time inside the reactor. Longer residence times leads to higher degrees of deoxygenation[32,34]. The overall yield of bio-oil from HDO is related to the degree of deoxygenation. Research on HDO over a Co-

MoS_2/Al_2O_3 catalyst showed a decrease in organic liquid yield from 55% to 30% when the degree of deoxygenation increased from 78% to 100%[35].

There are still disadvantages associated with hydrodeoxygenation of bio-oil. Hydrogen is an expensive feedstock to use in an upgrading process. A cheaper source of hydrogen will make HDO an even more attractive pathway for bio-oil upgrading. Another issue with HDO is the high operating pressures. Fast pyrolysis typically takes place at atmospheric pressure. Coupled with HDO, there is a stark pressure difference (70-200 bar), which introduces safety and economic concerns. Catalyst coking and deactivation is another problem frequently encountered with HDO. At increasing residence time and temperature, deoxygenation increases; however, so does catalyst coking[12].

1.3.3. Hydropyrolysis

To mitigate the issues associated with conventional bio-oil upgrading techniques, more advanced processes are needed. Hydropyrolysis is a more recent conversion process that is shown to produce liquid bio-oil with a lower oxygen content than fast pyrolysis. It was first used for increasing the yield from coal liquefaction[36,37]. Hydropyrolysis is similar to the process for conventional and catalytic fast pyrolysis, due to the organic matter quickly degrading under high heating rates and the similar reactor configurations. Unlike pyrolysis, however, hydropyrolysis is carried out under moderately high hydrogen pressure. Hydropyrolysis combines fast pyrolysis and HDO into a single step.

The process can be performed with or without a catalyst; however, hydropyrolysis without a catalyst has not shown a significant difference in the oxygen content of the oil[21,37,38]. Catalytic hydropyrolysis introduces a catalyst for additional upgrading. Catalytic hydropyrolysis removes oxygen in the form of H_2O, CO_2, and CO and eliminates several of the issues concerning polymerization and coking. Once the oxygen is removed, hydrogen is added to the hydrocarbon chain [39]. Hydropyrolysis has also been coupled with secondary hydrotreating reactors to further increase the degree of deoxygenation of the bio-oil[15,39-41]. Hydropyrolysis, similar to HDO, produces two liquid phases: an organic phase and an aqueous phase that are readily separable. The H/C ratio of the treated oil increases compared to fast pyrolysis oil while the O/C ratio decreases for various biomass feedstocks[42]. The chemical composition of the organic products from hydropyrolysis contains more aromatic hydrocarbons and is significantly different than that of fast pyrolysis. The product yield and oil composition from hydropyrolysis vary greatly depending on reaction conditions such as reactor configuration, operating conditions, and catalyst composition[37,43,44]. Increasing reaction temperature and the partial pressure of hydrogen typically decreases the organic oil yield. However, the oxygen content decreases at higher tempertures[37]. A significant difference, in terms of fuel quality, is the total acid number (TAN) of the hydropyrolysis oil. Oak Ridge National Lab found that hydropyrolysis drastically reduces the TAN from 119 to 14 for wood when compared to fast pyrolysis[45]. Hydropyrolysis coupled with secondary hydrotreating has been shown to drastically reduced the average molecular weight[39].

Several studies have explored catalytic hydropyrolysis without any further *ex-situ* upgrading downstream. Overall, catalytic hydropyrolysis was found to significantly increase the amount of deoxygenation of the liquid bio-oil and results in oxygen levels as low as 4%[37]. The main issue with catalytic hydropyrolysis without *ex-situ* upgrading is achieving the maximum amount of deoxygenation while still maintaining the highest decomposition of lignin. Hydrogenation is an exothermic reaction, so it is not favorable at higher temperatures. The optimum temperature found for hydrogenation is 300°C. This temperature allows for the hydrogenation of the aromatic hydrocarbons, such as benzene. However, it must be run at higher temperatures (400°C) to prevent low decomposition rates for lignin [44]. These issues make it very difficult to achieve full decomposition of the biomass while simultaneously fully deoxygenating the bio-oil in a one-pot solution; therefore, secondary HDO reactors have been investigated to increase the degrees of deoxygenation.

Catalytic hydropyrolysis coupled with a secondary hydrodeoxygenation reactor has been reported to produce oil with composition closer to that of gasoline and diesel than conventional pyrolysis oil[15]. The Gas Technology Institute (GTI) developed a state-of-the-art process, known as IH^2, which combines catalytic hydropyrolysis with a secondary hydrotreating reactor. The IH^2 process produced high quality oil with an oxygen content of less than 0.4 wt. % that met or exceeded several gasoline standard specifications[15]. An initial proof of concept study found that most of the deoxygenation occurred in the hydropyrolysis step, decreasing the oxygen content to less than 10% and the secondary reactor served to further reduce the oxygen content to that of petroleum quality. The specifics of the study such as catalyst composition and liquid product composition was not reported; but this work provides promising results on the potential utility of this advanced process.

1.3.3.1. Water-gas shift as a hydrogen source

Hydropyrolysis requires an adequate supply of hydrogen to optimize the hydrogenation of the product vapors. Hydrogen is an expensive material to bring in from an outside source. Therefore, it is more economical and efficient to produce hydrogen on site using readily available starting materials. Several well-documented reactions yield hydrogen as the main product, such as steam methane reforming, partial oxidation, and water-gas shift (WGS). GTI’s IH^2 process makes use of steam reforming to convert the light gases from hydropyrolysis to produce the hydrogen supplied to the system[15,46]. Steam reforming takes place at high temperatures (700-1000°C) [47].

Methane reacts with steam in the presence of a catalyst to produce hydrogen and CO. It has been determined that two reactions are involved in methane reforming. The primary steam reforming reaction involved methane reacting with steam to produce CO. The CO produced is further reacted with steam and is known as the water-gas shift (WGS) reaction.

$$CH_4 + H_2O \leftrightarrow 3H_2 + CO$$

$$CO + H_2O \leftrightarrow H_2 + CO_2$$

CO is reacted with steam (at a 1:1 stoichiometric ratio) in the presence of a catalyst to produce hydrogen and CO_2. In a stand-alone reaction, WGS takes place at lower temperatures than methane reforming (200-500 °C), which is closer to the operating conditions of hydropyrolysis [48]. The WGS reaction allows for the overall process temperature for hydrogen production and hydropyrolysis to be much closer and more easily integrated into a single process.

1.4. Computational modeling of pyrolysis

Conventional and advanced pyrolysis processes are very complex systems especially upon scaling up beyond the Pyro-GC/MS scale. Pyrolysis inside a fluidized bed reactor (FBR) introduces additional complexity to the pyrolysis system. The pyrolysis environment is made up of three phases: sand, biomass, and a gas/vapor phase. Inside an FBR, biomass and an inert bed material (sand) is fluidized by an inert gas entering at the bottom of the reactor. The sand in an FBR provides efficient and controlled heat transfer to the biomass particles as they mix together in the reactor. The interactions and forces between the three phases, coupled with the complex chemistry of pyrolysis complicates the overall understanding of pyrolysis by experimentation. Experimentally testing fast pyrolysis requires a significant time and financial investment. Numerical simulation and modeling have recently been seen as a potential avenue to strengthen the understanding of the phenomena that occur during pyrolysis and complement experimental testing. Computational fluid dynamics (CFD) is a numerical simulation technique that directly solves partial differential equations, such as the Navier Stokes and governing transport equations, to analyze complex problems involving fluid flows[49].

There are multiple mathematical methods that have been adopted to simulate pyrolysis inside a fluidized bed reactor. The two main methods are Eulerian-Eulerian, also known as a two-fluid model (TFM) or multi-fluid model (MFM), and Eulerian-Lagrangian, or a discrete element method (DEM). The numerical method chosen for a simulation determines how the transport equations and governing conservation equations will be solved. This chapter looks at work using both methods for comprehensive modeling for pyrolysis as well as simulations pertaining to advanced pyrolysis processes.

1.4.1. Eulerian-Eulerian

The Eulerian-Eulerian method treats all phases, regardless of whether it is a gas or solid, as continua. The individual phases can contain any number of chemical species. Pyrolysis simulations have one or two solid phases, depending on whether the sand and biomass are treated as separate phases. The MFM, expanded from the TFM proposed by Ishii and Mashima, solves the governing conservation equations for mass, momentum, energy for each chemical species and phase and accounts for the interdependence of the phases by incorporating source terms into the equations[50]. The governing conservation equations are listed in Table 1.2. Lathouwers and Bellan were the first to develop Eulerian-Eulerian method to model biomass fast pyrolysis in a FBR[51]. This model was then used to simulate and analyze the scaling up of pyrolysis to a pilot and commercial scale[52]. The pyrolysis reaction scheme adopted was that of Miller and Bellan, which is based on superimposed reactions, shown below, for each biomass major component: cellulose, hemicellulose, and lignin[53].

Table 1.2. Governing equation for each phase in Eulerian modeling. Adapted from Xiong et al.[58]

	Gas Phase	**Solid Phase**
Continuity	$\frac{\partial \alpha_g \rho_g}{\partial t} + \nabla(\alpha_g \rho_g U_g) = R_g$	$\frac{\partial \alpha_{sm} \rho_{sm}}{\partial t} + \nabla(\alpha_{sm} \rho_{sm} U_{sm}) = R_{sm}$
Momentum	$\frac{\partial(\alpha_g \rho_g U_g)}{\partial t} + \nabla(\alpha_g \rho_g U_g U_g)$ $= \nabla \tau_g - \alpha_g \nabla p + \sum_{m=1}^{M} \beta_{gsm}(U_{sm} - U_g) + \sum_{m=1}^{M} \psi_{gsm}$ $+ \alpha_g \rho_g g$	$\frac{\partial(\alpha_{sm} \rho_{sm} U_{sm})}{\partial t} + \nabla(\alpha_{sm} \rho_{sm} U_{sm} U_{sm})$ $= \nabla \tau_{sm} - \alpha_{sm} \nabla p + \beta_{gsm}(U_g - U_{sm}) + \sum_{l=1, l \neq m}^{M} \beta_{slm}(U_{sl} - U_{sm}) + \psi_{gsm}$ $+ \alpha_{sm} \rho_{sm} g$
Energy	$\frac{\partial(\alpha_g \rho_g C_{pg} T_g)}{\partial t} + \nabla(\alpha_g \rho_g C_{pg} T_g U_g) = \nabla q_g + \sum_{m=1}^{M} h_{gsm}(T_{sm} - T_g) + \Delta H_g$	$\frac{\partial(\alpha_{sm} \rho_{sm} C_{psm} T_{sm})}{\partial t} + \nabla(\alpha_{sm} \rho_{sm} C_{psm} T_{sm} U_{sm}) = \nabla q_{sm} + h_{gsm}(T_g - T_{sm}) + \Delta H_{sm}$
Species	$\frac{\partial \alpha_g \rho_g Y_{gk}}{\partial t} + \nabla(\alpha_g \rho_g Y_{gk} U_g) = R_{gk}$	$\frac{\partial \alpha_{sm} \rho_{sm} Y_{smk}}{\partial t} + \nabla(\alpha_{sm} \rho_{sm} Y_{smk} U_{sm}) = R_{smk}$

α_g/α_{sm}=Gas/Solid phase volume fraction, ρ_g/ρ_{sm}= Material density, U_g= Gas velocity vector, R_g/R_{sm}= Mass transfer source term, τ_g/τ_{sm} = Stress tensor, p=Pressure, β_{gsm}= Gas-solid inter-phase momentum exchange coefficient, β_{slm}= Momentum exchange coefficient between solid phase l and m, U_{sm}/U_{sl} = Solid phase velocity, ψ_{gsm}= Gas-solid momentum exchange due to mass transfer, g =Gravity vector, C_{pg}/C_{psm} = Heat capacity, T_g/T_{sm} = Temperature of the each phase, q_g/q_{sm} = Conductive heat flux, h_{gsm} = Gas-solid heat transfer coefficient, ΔH_g=Heat of reactions in gas phase, Y_{gk}/Y_{smk}= Mass fraction of species k in each phase, R_{gk}/R_{smk} = Reaction rate of species k in each phase, t = time

$$Virgin(s) \overset{k_1}{\rightarrow} Active(s)$$

$$Active(s) \overset{k_2}{\rightarrow} Tar(g)$$

$$Active(s) \overset{k_3}{\rightarrow} xChar(s) + (1 - x)Gas(g)$$

$$Tar(g) \overset{k_4}{\rightarrow} Gas(g)$$

Xue et al. performed significant work on simulating biomass fast pyrolysis in a FBR on the lab scale using MFIX, an open-source CFD software from the National Energy Technology Laboratory (NETL) [54-56]. The pyrolysis simulations were carried out over various operating conditions and validated using a lab-scale FBR. Xue et al. found the operating temperature, superficial gas velocity, and the particle size distribution play significant roles in determining the overall yields[55]. Mellin et al. developed a three-dimensional (3D) model in ANSYS Fluent that focused on the vapor phase by studying the interaction between the biomass and sand mixture and vapor phase in a FBR[57]. This study assumed the sand particles have the largest effect on the gas phase, which allowed for a combination of the biomass and sand phases to one granular phase. The pyrolysis model showed that at moderate temperatures, the fluidization velocity did not have a significant effect on the bio-oil yield; but, the liquid yield decreased at higher temperatures. Xiong et al., at Iowa State University, have researched computational modeling of biomass fast pyrolysis[58-63]. To easily facilitate implementation of individual submodels into a CFD code, Xiong et al. used the existing OpenFOAM CFD structure to develop a new open-source program, BIOTC, with the goal of simulating pyrolysis using the MFM[58,62]. The BIOTC simulation provided general agreement with both the results found from the bench scale experiment as well as simulations carried out in MFIX with the same kinetic scheme. BIOTC was used to study the effect of operating conditions and different interphase transport coefficients on pyrolysis using the Miller and Bellan reaction scheme[61,63]. The submodel used for the particle drag force had a much larger effect on the bio-oil yield than the heat transfer submodel used. Based on the results from the previous work, a validation study was performed to simulate a BFBR located at an Agricultural Research Service (ARS) laboratory of the United States Department of Agriculture (USDA)[63,64]. The validated case served as a reference state for simulations investigating the effects of operating conditions such as reactor temperature, particle diameter, and fluidizing gas velocity. Temperature for both the reactor and fluidizing gas had the largest effect on the product yield distribution. Xue and Fox incorporated a quadrature based moment method (QBMM) to account for the particle size distribution (PSD) and variable particle density into a MFM CFD model[56]. Simulations with a PSD showed slightly higher yields than a single size while overall product yields were comparable to lab scale experimental results. Xiong et al. investigated the effect of hydrodynamics on the bio-oil vapors at the outlet of the reactor[60]. Due to the hydrodynamic instability of a FBR, operating conditions will not only affect the product yield but will also cause fluctuations at the outlet. Increased fluidizing gas velocity, bed particle size, and bed height increased the bio-oil yield while also increasing the amount of fluctuation. The Miller and Bellan kinetic scheme and the CFD works mentioned above assume the kinetics proceed through an Arrhenius reaction rate:

$$k = k_0 e^{-\frac{E_a}{RT}}$$

Xiong et al. adapted their existing MFM CFD model to incorporate a distributed activation energy model (DAEM) to account for the diverse nature of biomass. The DAEM predicted higher bio-oil yields and fluctuations compared to conventional single-value kinetics due to the diversity of the activation energies within the DAEM. One of the disadvantages of an Eulerian-Eulerian approach is it is difficult to account for transport on the particle scale. Dong et al. aimed to use a MFM approach to account for intra-particle heat conduction between particles while modeling the fast pyrolysis of corn stalks[65]. The reaction rates for each step (i.e. biomass to active) were modified to take the heat penetration rate into account. The heat penetration model was found to be valid for modeling conduction; but, more work is needed to improve product yield predictions.

CFD studies on pyrolysis have incorporated other schemes than the one proposed by Miller and Bellan. Recent work in Eulerian-Eulerian MFM simulations have also incorporated a two-step semi-global lumped kinetic model, which served as the basis for the former scheme[66-68].

$$Biomass(s) \overset{k_1}{\rightarrow} Bio-oil(g)$$

$$Biomass(s) \overset{k_2}{\rightarrow} Gas(g)$$

$$Biomass(s) \overset{k_3}{\rightarrow} Char(s)$$

$$Bio-oil(g) \overset{k_4}{\rightarrow} Gas(g)$$

$$Bio-oil(g) \overset{k_5}{\rightarrow} Char(s)$$

Lee at al. compared a lumped model of pyrolysis with a hybrid CFD model and found the accuracy of the results were greatly improved in the CFD model[69]. Sharma et al. also used this scheme in ANSYS FLUENT and studied the effect of temperature and fluidization velocity[70]. An important characteristic in BFBR is the bubble behavior inside the bed. Lee at al. used the semi-global lumped kinetic model with MFIX to study the behavior of bubbles in an FBR during pyrolysis and how that affects the overall process[71]. The dimensions of the FBR had a significant effect on the formation of bubbles, which influenced the yields of pyrolysis. Xiong et al. compared three pyrolysis reaction schemes using the MFM approach[72]. The two-step semi-global kinetic model as well as the Miller and Bellan model were compared. The third model only considered the primary (first three) reactions of the semi-global scheme and did not account for secondary cracking reactions. The Miller and Bellan scheme provided the closest product predictions to experimental results; but, the choice of scheme did not appear to have a significant effect on the hydrodynamics of the process.

A simple one-step scheme for biomass fast pyrolysis has also been used for CFD MFM simulations. The product coefficients, x_g x_{BO}, and x_c, are the species' respective mass fraction.

$$Biomass \rightarrow x_g Gas + x_{BO} Bio - oil + x_c Char$$

Zhong et al. adopted the single step kinetic scheme, based on coal devolitilization[73,74], and developed a MFM that assumed a varying particle size model to account for particle shrinkage during pyrolysis[75]. The particle shrinkage effect had an impact on the char entrainment, char yield, and biomass conversion. A weaker shrinkage effect would lead to increased entrainment and yield of char while decreasing overall biomass conversion. The pyrolysis of algal biomass has also been investigated using CFD and the one-step pyrolysis reaction scheme. The reaction kinetics of algal biomass are slightly different than the scheme shown above and kinetics were adopted from previous experimental work on algal pyrolysis[76-78]. Azizi and Mowla developed an Eulerian-Eulerian CFD model to model novel flash pyrolysis of algae using inert heat carrier particles[79].

An expanded version of the single-step kinetic scheme was proposed by Zhou et al[80]. The gas species was further decomposed into the major components of pyrolysis non-condensable gases.

$$Gas = \gamma_1 CO + \gamma_2 CO_2 + \gamma_3 CH_4 + \gamma_4 H_2 + \gamma_5 C_2H_4$$

Boateng and Mtui modeled biomass fast pyrolysis in a FBR developed at ARS to investigate the evolution of products throughout the length of the reactor[81].

One of the drawbacks of the semi-global and lumped kinetic scheme is the inability to have any indication on the composition of bio-oil. Simplifying a scheme introduces the risk of reducing the overall accuracy. Recent CFD studies have begun to incorporate more comprehensive reaction schemes into their models, such as Ranzi et al. (Figure 1.1), that breaks down bio-oil into individual “model” compounds such as levoglucosan and glyoxal and accounts for secondary cracking reactions of the bio-oil[82]. Mellin et al. expanded their previous Eulerian-Eulerian model to incorporate a more complex kinetic scheme and add a third Eulerian phase[83-85]. The comprehensive scheme was readily incorporated into a MFM CFD model; but, the secondary cracking reactions proposed did not account for the high amount of water that is typically seen duirng pyrolysis. The effect of fluidizing gas (nitrogen versus steam) on the pyrolysis process was determined[85]. Steam did not have a significant effect on the pyrolysis product yields; but, more work is required to determine the effect of steam on secondary cracking reactions. Other fluidizing gases, such as CO, CO_2, and H_2, were also simulated and the latter affected the reactions differently than the others; therefore, more work is needed to improve the model’s reliability[84]. Biomass contains inorganics that can significantly affect the pyrolysis process. Eri et al. investigated the role of potassium on the fast pyrolysis of cellulose[86]. The cellulose pyrolysis kinetics were modeled via a modified version of the Ranzi scheme proposed by Trendewicz et al.[87] The concentration of potassium had a negative effect on the bio-oil yield, which is expected due to the catalytic effect of inorganics. Ranganathan and Gu compared three kinetic schemes for their ability to model experimental data[88]. A simple model, proposed by Di Blasi, was compared alongside the Miller and Bellan

Initial solid components: cellulose (Cell), hemicellulose (Hcell), carbon-rich lignin (LignC), hydrogen-rich lignin (LignH), and oxygen-rich lignin(LignO)
Activated solids: activated cellulose (CellA), activated hemicellulose 1 (HCell1), activated hemicellulose (HCell2), carbon-rich lignin 2 (LignCC), OH-rich lignin (LignOH)
Vapors: levoglucosan (LVG), hydroxyacetaldehyde (HAA), 5-hydroxymethyl-furfural (HMFU), paracoumaryl alcohol (p-Coumaryl), sinapaldehyde (Lumped-phenol)

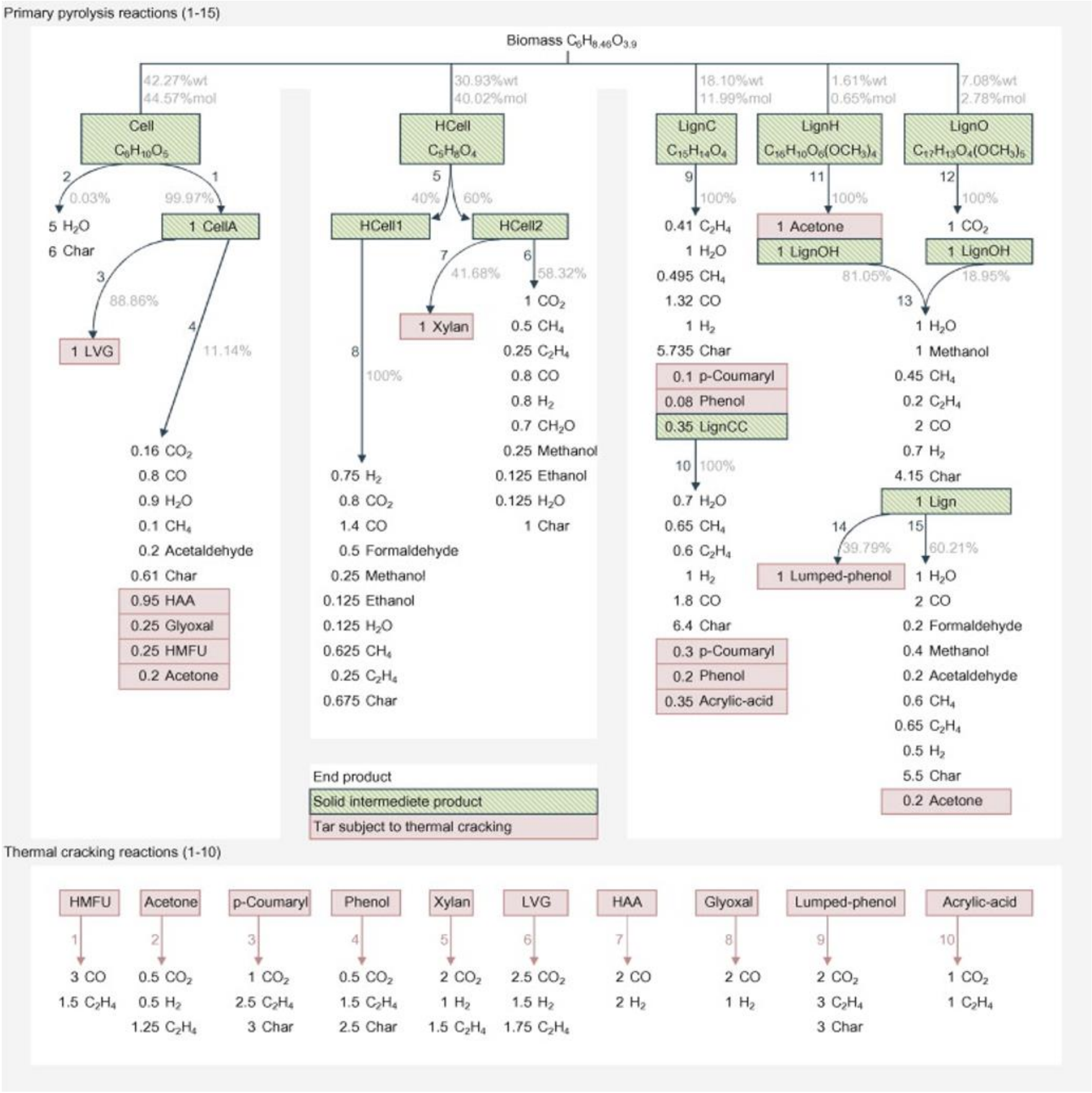

Figure 1.1. Illustration of the comprehensive pyrolysis "Ranzi" reaction scheme. Adapted from Mellin et al[83]. (with permission from Elsevier for use in this thesis). Copyright 2014 Elsevier.

model as well as the primary Ranzi scheme[53,82,89]. The Ranzi scheme resulted in an improved prediction of the yield of products.

Typically, CFD models are difficult to incorporate into macroscopic, large scale process simulations. Trendewicz et al. developed a one-dimensional (1D) CFD model using the Ranzi scheme, without the secondary cracking reactions, that can be used with existing biorefinery process models[90]. The 1D model is seen as attractive due to the relative agreement between existing two-dimensional (2D) models. Humbird et al. created a 1D fast pyrolysis reactor model to be incorporated into an overall pyrolysis process model using Aspen Plus (Aspen Technology, Bedford, MA, USA) with the hope of facilitating future development through modeling and optimization[91].

1.4.2. Eulerian-Lagrangian

The Eulerian-Lagrangian approach in CFD typically treats the gas phase as a continuum, with each individual solid particle modeled in a Lagrangian manner. The interactions between the two phases are accounted for as source terms in the conservation equations. The solid particles are modeled using a different set of equations than the Eulerian phase. Newton's second law of motion is used to solve for the movement and transport of the individual solid particle[92].The equations for translational and rotational motion of shown below:

$$m_i \frac{dv_i}{dt} = \sum_j F_{ij}^c + \sum_k F_{ik}^{nc} + F_i^f + F_i^g$$

$$I_i \frac{d\omega_i}{dt} = \sum_j M_{ij}$$

where m_i is the mass of the particle, v_i is the translational velocity of particle i, F_{ij}^{c} is the contact force acting on the particle by another particle or the wall, F_{ik}^{nc} is the non-contact force on the particle from particle k or other sources, F_i^f is the particle-fluid interaction force on the particle, F_i^g is the gravitational force, ω_i is the angular velocity of particle i, I_i is the moment of inertia, and M_{ij} is the torque on particle i by particle k or walls[92]. Sub models are used to calculate specific parameters that can be incorporated into a DEM simulation compared to a MFM, such as a particle shrinkage model, the drag force, and the contact force acting on a particle. Depending on the simulation setup, the DEM may need to simulate over a million individual particles. The DEM approach provides more detailed information about the process than the MFM approach but requires higher computational costs. Due to the large particle tracking requirement, DEM is not practical for modeling industrial scale applications, but can be very useful on the lab scale.

Initial work on Eulerian-Lagrangian modeling of biomass pyrolysis focused on different reactor setups, such as an entrained flow reactor, a drop tube reactor, and a vortex reactor[93-103]. Fluidized bed reactors introduce additionally complexity to a CFD-DEM simulation. Fluidized bed reactors add another solid phase, which if simulated using Lagrangian methods greatly increases computational costs.

Papadikis et al. modeled pyrolysis in a FBR using CFD-DEM[104-111]. For the initial model, a single cellulose particle was modeled in a fluidized bed located in Aston University using a Broido-Shafizadeh kinetic scheme[112].

$$Cellulose \overset{k_1}{\rightarrow} Active\ Cellulose$$

$$Active\ Cellulose \overset{k_2}{\rightarrow} Char\ and\ Gas$$

$$Active\ Cellulose \overset{k_3}{\rightarrow} Vapours\ and\ Water$$

$$Vapours\ and\ Water \overset{k_4}{\rightarrow} Gas$$

The effect of sand was not accounted for in the simulation and the fluidizing gas was the only source of heat transfer to the particle. Following up on the preliminary CFD-DEM model, a two-part study to develop a complete model of biomass fast pyrolysis of a single biomass particle using in ANSYS Fluent[107,111]. In Part A, the heat and momentum transfer of a single particle in both 2D and 3D setups were compared, while Part B incorporated reaction pyrolysis reaction kinetics to develop a complete model of pyrolysis on a single biomass particle in a FBR. The sand phase was modeled as a second Eulerian phase with only the biomass particle being tracked in a discrete manner. Pyrolysis reaction kinetics were represented using the two-stage semi-global mechanism described earlier[66-68]. The single particle CFD model produced yields similar to that of previous single particle models. The simulations assumed that the biomass particle was perfectly spherical and did not account for any particle shrinkage due to drying and volatilization. Particle shrinkage has been shown to have a significant effect on pyrolysis reactions[113]. Papadikis et al. investigated the effect of different particle shrinkage parameters during pyrolysis[106]. Lagrangian particle tracking was able to calculate the positions of a particle throughout the reactor, which allowed for analysis of char entrainment in the reactor. Various particle sizes were simulated to visualize how size affects flow behavior[108]. Particle size also had significant impact on heat transfer to the biomass during pyrolysis with smaller particles typically being preferred for pyrolysis in a FBR[109]. Rabinovich et al. also found the size of the biomass particle was inversely proportional to the biomass conversion achieved with larger particles[114]. Biomass particles were assumed to have a sphericity of one in CFD-DEM simulations. Simulations carried out with different particle shape (cubical and tetrahedral) found that particle shape significantly affected flow behavior and residence time in the reactor[110]. Bruchmüller et al. incorporated the Miller and Bellan pyrolysis scheme into a CFD-DEM model that simulated more than just a single particle[115,116]. Segregation was seen to occur at lower fluidization velocities, leading to poorer mixing and heat transfer. Mixing and heat transfer both affected the overall oil yield and quality from biomass pyrolysis[116].

Much of the CFD-DEM work involving biomass pyrolysis in a FBR assumed sand behaved as an Eulerian phase. The number of biomass particles in a FBR are orders of magnitude smaller than the number of sand particles. Individually tracking the sand particles greatly increases the computation cost for modeling of pyrolysis. Modeling the sand as a continuous phase reduces the computational cost at the expense of more detailed information of biomass-sand particle interactions.

1.5. Computational modeling of upgrading processes

Advances in computational power have made it possible to model biomass fast pyrolysis with increasing accuracy. However, fast pyrolysis modeling does not account for the bio-oil upgrading that is required to produce a useful fuel. Hydrodeoxygenation has been experimentally tested in several ways; but, there is little literature available on the numerical modeling of HDO. Gollakota et al. was one of the first to simulate HDO of bio-oil using CFD-MFM[117]. The effect of the catalyst type on HDO was investigated over several operating conditions. A lumped kinetic approach was adopted in the model, for which “heavy” non-volatiles (HNV) are deoxygenated to “light” non-volatiles (LNV), alkanes and aromatics through five reactions[118].

$$HNV \overset{k_1}{\rightarrow} LNV$$

$$HNV \overset{k_2}{\rightarrow} Alkane + Aromatic$$

$$LNV \overset{k_3}{\rightarrow} Phenol$$

$$Phenol \overset{k_4}{\rightarrow} Alkane + Aromatic$$

$$Alkane + Aromatic \overset{k_5}{\rightarrow} Coke + Water\ Vapor + Gases$$

The catalyst was shown to have a significant effect on phase behavior and product evolution. Subramanyam et al. used the same reactor geometry to simulate the HDO of pyrolytic oil over a Pt/Al_2O_3 catalyst[119]. Of the varied operating conditions, an increase of pressure was shown to produce the greatest increases of production for the favorable products (alkanes and aromatics). Numerical models have been explored as ways to simulate the HDO of bio-oil. Chu et al. modeled the HDO process applied to camelina, carinata, and used cooking oil to produce renewable jet fuel[120]. Conversion reactions were modeled using Microsoft Excel using HDO reactions from Snåre et al. (Table 1.3) [121]. The process energy requirements for the HDO process were also calculated using Aspen Plus.

To the best of my knowledge there is no literature available dealing with CFD modeling of biomass hydropyrolysis. Hydropyrolysis was initially employed for converting coal into valuable compounds, and Ma et al. developed a CFD-DEM model to simulate hydropyrolysis of coal in a rotating plasma reactor[122]. The results from this novel model compared well with experimental testing and can serve as the groundwork for further optimization of the process.

There is a gap in the literature pertaining to modeling of advanced pyrolysis processes, mainly the CFD modeling of hydropyrolysis. There is promising progress being made in modeling fast pyrolysis. The complexity of HDO kinetics for bio-oil upgrading makes implementation into a numerical model difficult. CFD modeling of these advanced pyrolysis processes have the

Table 1.3. Reactions present in the hydrodeoxygenation process. Adapted from Chu et al.[120]

Reaction		Heat of reaction (kJ/mol)
Decarboxylation	$C_nH_{2n}O_2 \rightarrow C_{n-1}H_{2n} + CO_2$	9.2
Decarbonylation	$C_nH_{2n}O_2 + H_2 \rightarrow C_{n-1}H_{2n} + CO + H_2O$	179.1
Hydrodeoxygenation	$C_nH_{2n}O_2 \rightarrow C_nH_{2n+2} + 2H_2O$	-115.0
Methanation	$CO_2 + 4H_2 \leftrightarrow CH_4 + 2H_2O$	-177.2
	$CO + 3H_2 \leftrightarrow CH_4 + H_2O$	-216.4
Water-gas shift	$CO + 4H_2O \rightarrow H_2 + CO_2$	-39.2

potential to play an integral role moving forward in the optimization of high-quality bio-oil production.

1.6. Conclusions

Pyrolysis of biomass produces a bio-oil that, after significant deoxygenation, can serve as a renewable alternative to petroleum fuels. Advanced pyrolysis processes, such as catalytic fast pyrolysis and hydropyrolysis, have been explored to develop an optimized, one-step process to deoxygenate pyrolysis vapors to produce high quality fuels. The complexity of pyrolysis makes it hard to analyze the behavior of the reaction environment. Therefore, computational modeling has become an increasingly popular tool to help understand and optimize the process to maximize the yield and quality of bio-oil. Both MFM and DEM approaches have been taken to simulate pyrolysis in a FBR. DEM provides a more detailed description of the phenomena occurring at the particle scale; but, the computational cost makes it very difficult to model larger scale problems. Work continues to be done on improving the CFD modeling of biomass fast pyrolysis; however, little literature is available for CFD modeling of the advanced pyrolysis processes. CFD modeling of both pyrolysis and hydropyrolysis will play an important part of understanding the process and designing future reactors.

List of references

(1) Mathioudakis, V.; Gerbens-Leenes, P. W.; Van der Meer, T. H.; Hoekstra, A. Y. The water footprint of second-generation bioenergy: A comparison of biomass feedstocks and conversion techniques. *Journal of Cleaner Production* **2017,** *148*, 571.

(2) Khan, A. A.; de Jong, W.; Jansens, P. J.; Spliethoff, H. Biomass combustion in fluidized bed boilers: Potential problems and remedies. *Fuel Processing Technology* **2009,** *90* (1), 21.

(3) Cheng, J.; Boca Raton : CRC Press: Boca Raton, 2010.

(4) Pandey, A.; Bhaskar, T.; Stöcker, M.; Sukumaran, R. *Recent Advances in Thermochemical Conversion of Biomass*; Elsevier, 2015.

(5) Kan, T.; Strezov, V.; Evans, T. J. Lignocellulosic biomass pyrolysis: A review of product properties and effects of pyrolysis parameters. *Renewable and Sustainable Energy Reviews* **2016,** *57*, 1126.

(6) Czernik, S.; Bridgwater, A. V. Overview of applications of biomass fast pyrolysis oil. *Energy & Fuels* **2004,** *18* (2), 590.

(7) Bridgwater, A. V. Review of fast pyrolysis of biomass and product upgrading. *Biomass Bioenergy* **2012,** *38*, 68.

(8) Mohan, D.; Pittman, C. U.; Steele, P. H. Pyrolysis of Wood/Biomass for Bio-oil: A Critical Review. *Energy & Fuels* **2006,** *20* (3), 848.

(9) Bridgwater, A. V.; Meier, D.; Radlein, D. An overview of fast pyrolysis of biomass. *Organic Geochemistry* **1999,** *30* (12), 1479.

(10) Scott, D. S.; Majerski, P.; Piskorz, J.; Radlein, D. A second look at fast pyrolysis of biomass—The RTI process. *Journal of Analytical and Applied Pyrolysis* **1999,** *51* (1–2), 23.

(11) Venderbosch, R. H.; Prins, W. Fast pyrolysis technology development. *Biofuels, Bioproducts and Biorefining* **2010,** *4* (2), 178.

(12) Dickerson, T.; Soria, J. Catalytic fast pyrolysis: A review. *Energies* **2013,** *6* (1), 514.

(13) Westerhof, R. J. M.; Kuipers, N. J. M.; Kersten, S. R. A.; van Swaaij, W. P. M. Controlling the Water Content of Biomass Fast Pyrolysis Oil. *Industrial & Engineering Chemistry Research* **2007,** *46* (26), 9238.

(14) Talmadge, M. S.; Baldwin, R. M.; Biddy, M. J.; McCormick, R. L.; Beckham, G. T.; Ferguson, G. A.; Czernik, S.; Magrini-Bair, K. A.; Foust, T. D.; Metelski, P. D.et al. A perspective on oxygenated species in the refinery integration of pyrolysis oil. *Green Chemistry* **2014,** *16* (2), 407.

(15) Marker, T. L.; Felix, L. G.; Linck, M. B.; Roberts, M. J.; Ortiz-Toral, P.; Wangerow, J. Integrated hydropyrolysis and hydroconversion (IH2®) for the direct production of gasoline and diesel fuels or blending components from biomass, part 2: Continuous testing. *Environmental Progress & Sustainable Energy* **2014,** *33* (3), 762.

(16) Ruddy, D. A.; Schaidle, J. A.; Ferrell Iii, J. R.; Wang, J.; Moens, L.; Hensley, J. E. Recent advances in heterogeneous catalysts for bio-oil upgrading via "ex situ catalytic fast pyrolysis": Catalyst development through the study of model compounds. *Green Chemistry* **2014,** *16* (2), 454.

(17) Liu, C.; Wang, H.; Karim, A. M.; Sun, J.; Wang, Y. Catalytic fast pyrolysis of lignocellulosic biomass. *Chemical Society Reviews* **2014,** *43* (22), 7594.

(18) Zhang, H.; Xiao, R.; Huang, H.; Xiao, G. Comparison of non-catalytic and catalytic fast pyrolysis of corncob in a fluidized bed reactor. *Bioresource Technology* **2009,** *100* (3), 1428.

(19) Yildiz, G.; Ronsse, F.; Prins, W.; Assink, D.; Gerritsen, L.; van Duren, R.; Rosso-Vasic, M. 19th European Biomass Conference and Exhibition, Berlin, Germany, 2011; p 1145.

(20) Imran, A.; Bramer, E.; Seshan, K.; Brem, G. Catalytic Flash Pyrolysis of Biomass Using Different Types of Zeolite and Online Vapor Fractionation. *Energies* **2016,** *9* (3), 187.

(21) Thangalazhy-Gopakumar, S.; Adhikari, S.; Gupta, R. B.; Tu, M.; Taylor, S. Production of hydrocarbon fuels from biomass using catalytic pyrolysis under helium and hydrogen environments. *Bioresource Technology* **2011,** *102* (12), 6742.

(22) Gollakota, A. R. K.; Reddy, M.; Subramanyam, M. D.; Kishore, N. A review on the upgradation techniques of pyrolysis oil. *Renewable and Sustainable Energy Reviews* **2016,** *58*, 1543.

(23) Bridgwater, A. V. Catalysis in thermal biomass conversion. *Applied Catalysis A: General* **1994,** *116* (1), 5.

(24) Williams, P. T.; Horne, P. A. The influence of catalyst regeneration on the composition of zeolite-upgraded biomass pyrolysis oils. *Fuel* **1995,** *74* (12), 1839.

(25) Bridgwater, A. V. Production of high grade fuels and chemicals from catalytic pyrolysis of biomass. *Catalysis Today* **1996,** *29* (1), 285.

(26) Bulushev, D. A.; Ross, J. R. H. Catalysis for conversion of biomass to fuels via pyrolysis and gasification: A review. *Catalysis Today* **2011,** *171* (1), 1.

(27) Furimsky, E. Catalytic hydrodeoxygenation. *Applied Catalysis A: General* **2000,** *199* (2), 147.

(28) Topsøe, H.; Clausen, B. S.; Massoth, F. E. In *Catalysis: Science and Technology*; Anderson, J. R.;Boudart, M., Eds.; Springer Berlin Heidelberg: Berlin, Heidelberg, 1996.

(29) Şenol, O. İ.; Viljava, T. R.; Krause, A. O. I. Hydrodeoxygenation of methyl esters on sulphided NiMo/γ-Al2O3 and CoMo/γ-Al2O3 catalysts. *Catalysis Today* **2005,** *100* (3), 331.

(30) Gutierrez, A.; Kaila, R. K.; Honkela, M. L.; Slioor, R.; Krause, A. O. I. Hydrodeoxygenation of guaiacol on noble metal catalysts. *Catalysis Today* **2009,** *147* (3), 239.

(31) Şenol, O. İ.; Ryymin, E. M.; Viljava, T. R.; Krause, A. O. I. Reactions of methyl heptanoate hydrodeoxygenation on sulphided catalysts. *Journal of Molecular Catalysis A: Chemical* **2007,** *268* (1), 1.

(32) Venderbosch, R. H.; Ardiyanti, A. R.; Wildschut, J.; Oasmaa, A.; Heeres, H. J. Stabilization of biomass-derived pyrolysis oils. *Journal of Chemical Technology & Biotechnology* **2010,** *85* (5), 674.

(33) Mortensen, P. M.; Grunwaldt, J. D.; Jensen, P. A.; Knudsen, K. G.; Jensen, A. D. A review of catalytic upgrading of bio-oil to engine fuels. *Applied Catalysis A: General* **2011,** *407* (1), 1.

(34) Elliott, D. C. Historical Developments in Hydroprocessing Bio-oils. *Energy & Fuels* **2007,** *21* (3), 1792.

(35) Samolada, M. C.; Baldauf, W.; Vasalos, I. A. Production of a bio-gasoline by upgrading biomass flash pyrolysis liquids via hydrogen processing and catalytic cracking. *Fuel* **1998,** *77* (14), 1667.

(36) Ladelfa, C. J.; Greene, M. I. Economic evaluation of synthetic natural gas production by short residence time hydropyrolysis of coal. *Fuel Processing Technology* **1978,** *1* (3), 187.

(37) Dayton, D. C.; Carpenter, J.; Farmer, J.; Turk, B.; Gupta, R. Biomass hydropyrolysis in a pressurized fluidized bed reactor. *Energy & Fuels* **2013,** *27* (7), 3778.

(38) Venkatakrishnan, V. K.; Degenstein, J. C.; Smeltz, A. D.; Delgass, W. N.; Agrawal, R.; Ribeiro, F. H. High-pressure fast-pyrolysis, fast-hydropyrolysis and catalytic hydrodeoxygenation of cellulose: production of liquid fuel from biomass. *Green Chemistry* **2014,** *16* (2), 792.

(39) Marker, T. L.; Felix, L. G.; Linck, M. B.; Roberts, M. J. Integrated hydropyrolysis and hydroconversion (IH2®) for the direct production of gasoline and diesel fuels or blending components from biomass, part 1: Proof of principle testing. *Environmental Progress & Sustainable Energy* **2012,** *31* (2), 191.

(40) Venkatakrishnan, V. K.; Delgass, W. N.; Ribeiro, F. H.; Agrawal, R. Oxygen removal from intact biomass to produce liquid fuel range hydrocarbons via fast-hydropyrolysis and vapor-phase catalytic hydrodeoxygenation. *Green Chemistry* **2015,** *17* (1), 178.

(41) Melligan, F.; Hayes, M. H. B.; Kwapinski, W.; Leahy, J. J. A study of hydrogen pressure during hydropyrolysis of Miscanthus x giganteus and online catalytic vapour upgrading with Ni on ZSM-5. *Journal of Analytical and Applied Pyrolysis* **2013,** *103,* 369.

(42) Balagurumurthy, B.; Oza, T. S.; Bhaskar, T.; Adhikari, D. K. Renewable hydrocarbons through biomass hydropyrolysis process: challenges and opportunities. *Journal of Material Cycles and Waste Management* **2013,** *15* (1), 9.

(43) He, S.; Boom, J.; van der Gaast, R.; Seshan, K. Hydro-pyrolysis of lignocellulosic biomass over alumina supported Platinum, Mo2C and WC catalysts. *Frontiers of Chemical Science and Engineering* **2018,** *12* (1), 155.

(44) Resende, F. L. P. Recent advances on fast hydropyrolysis of biomass. *Catalysis Today* **2016,** *269,* 148.

(45) Roberts, M.; Marker, T.; Ortiz-Toral, P.; Linck, M.; Felix, L.; Wangerow, J.; Swanson, D.; McLeod, C.; Del Paggio, A.; Urade, V.et al. "Refinery Upgrading of Hydropyrolysis Oil From Biomass,"; Gas Technology Institute, Des Plaines, IL (United States), 2015.

(46) Tan, E. C. D.; Marker, T. L.; Roberts, M. J. Direct production of gasoline and diesel fuels from biomass via integrated hydropyrolysis and hydroconversion process—A techno-economic analysis. *Environmental Progress & Sustainable Energy* **2014,** *33* (2), 609.

(47) Dicks, A. L.; Pointon, K. D.; Siddle, A. Intrinsic reaction kinetics of methane steam reforming on a nickel/zirconia anode. *Journal of Power Sources* **2000,** *86* (1–2), 523.

(48) Grenoble, D. C.; Estadt, M. M.; Ollis, D. F. The chemistry and catalysis of the water gas shift reaction. *Journal of Catalysis* **1981,** *67* (1), 90.

(49) Cummings, R. M.; Mason, W. H.; Morton, S. A.; McDaniel, D. R. *Applied Computational Aerodynamics: A Modern Engineering Approach*; Cambridge University Press, 2015.

(50) Ishii, M.; Mishima, K. Two-fluid model and hydrodynamic constitutive relations. *Nuclear Engineering and Design* **1984,** *82* (2), 107.

(51) Lathouwers, D.; Bellan, J. Modeling of dense gas–solid reactive mixtures applied to biomass pyrolysis in a fluidized bed. *International Journal of Multiphase Flow* **2001,** *27* (12), 2155.

(52) Lathouwers, D.; Bellan, J. Yield Optimization and Scaling of Fluidized Beds for Tar Production from Biomass. *Energy & Fuels* **2001,** *15* (5), 1247.

(53) Miller, R. S.; Bellan, J. A Generalized Biomass Pyrolysis Model Based on Superimposed Cellulose, Hemicelluloseand Liqnin Kinetics. *Combustion Science and Technology* **1997,** *126* (1-6), 97.

(54) Xue, Q.; Heindel, T. J.; Fox, R. O. A CFD model for biomass fast pyrolysis in fluidized-bed reactors. *Chemical Engineering Science* **2011,** *66* (11), 2440.

(55) Xue, Q.; Dalluge, D.; Heindel, T. J.; Fox, R. O.; Brown, R. C. Experimental validation and CFD modeling study of biomass fast pyrolysis in fluidized-bed reactors. *Fuel* **2012,** *97*, 757.

(56) Xue, Q.; Fox, R. O. Computational Modeling of Biomass Thermochemical Conversion in Fluidized Beds: Particle Density Variation and Size Distribution. *Industrial & Engineering Chemistry Research* **2015,** *54* (16), 4084.

(57) Mellin, P.; Zhang, Q.; Kantarelis, E.; Yang, W. An Euler–Euler approach to modeling biomass fast pyrolysis in fluidized-bed reactors – Focusing on the gas phase. *Applied Thermal Engineering* **2013,** *58* (1), 344.

(58) Xiong, Q.; Kong, S.-C.; Passalacqua, A. Development of a generalized numerical framework for simulating biomass fast pyrolysis in fluidized-bed reactors. *Chemical Engineering Science* **2013,** *99*, 305.

(59) Xiong, Q.; Zhang, J.; Xu, F.; Wiggins, G.; Stuart Daw, C. Coupling DAEM and CFD for simulating biomass fast pyrolysis in fluidized beds. *Journal of Analytical and Applied Pyrolysis* **2016,** *117*, 176.

(60) Xiong, Q.; Xu, F.; Ramirez, E.; Pannala, S.; Daw, C. S. Modeling the impact of bubbling bed hydrodynamics on tar yield and its fluctuations during biomass fast pyrolysis. *Fuel* **2016,** *164*, 11.

(61) Xiong, Q.; Kong, S.-C. Modeling effects of interphase transport coefficients on biomass pyrolysis in fluidized beds. *Powder Technology* **2014,** *262*, 96.

(62) Xiong, Q.; Aramideh, S.; Passalacqua, A.; Kong, S.-C. BIOTC: An open-source CFD code for simulating biomass fast pyrolysis. *Computer Physics Communications* **2014,** *185* (6), 1739.

(63) Xiong, Q.; Aramideh, S.; Kong, S.-C. Modeling Effects of Operating Conditions on Biomass Fast Pyrolysis in Bubbling Fluidized Bed Reactors. *Energy & Fuels* **2013,** *27* (10), 5948.

(64) Boateng, A. A.; Daugaard, D. E.; Goldberg, N. M.; Hicks, K. B. Bench-Scale Fluidized-Bed Pyrolysis of Switchgrass for Bio-Oil Production. *Industrial & Engineering Chemistry Research* **2007,** *46* (7), 1891.

(65) Dong, N. H.; Luo, K. H.; Wang, Q. Modeling of biomass pyrolysis in a bubbling fluidized bed reactor: Impact of intra-particle heat conduction. *Fuel Processing Technology* **2017,** *161*, 199.

(66) Chan, W.-C. R.; Kelbon, M.; Krieger, B. B. Modelling and experimental verification of physical and chemical processes during pyrolysis of a large biomass particle. *Fuel* **1985,** *64* (11), 1505.

(67) Di Blasi, C. Analysis of Convection and Secondary Reaction Effects Within Porous Solid Fuels Undergoing Pyrolysis. *Combustion Science and Technology* **1993,** *90* (5-6), 315.

(68) Liden, A. G.; Berruti, F.; Scott, D. S. A kinetic model for the production of liquids from the flash pyrolysis of biomass. *Chemical Engineering Communications* **1988,** *65* (1), 207.

(69) Lee, Y. R.; Choi, H. S.; Park, H. C.; Lee, J. E. A numerical study on biomass fast pyrolysis process: A comparison between full lumped modeling and hybrid modeling combined with CFD. *Computers & Chemical Engineering* **2015,** *82*, 202.

(70) Sharma, A.; Wang, S.; Pareek, V.; Yang, H.; Zhang, D. Multi-fluid reactive modeling of fluidized bed pyrolysis process. *Chemical Engineering Science* **2015,** *123*, 311.

(71) Lee, J. E.; Park, H. C.; Choi, H. S. Numerical Study on Fast Pyrolysis of Lignocellulosic Biomass with Varying Column Size of Bubbling Fluidized Bed. *ACS Sustainable Chemistry & Engineering* **2017,** *5* (3), 2196.

(72) Xiong, Q.; Aramideh, S.; Kong, S. C. Assessment of devolatilization schemes in predicting product yields of biomass fast pyrolysis. *Environmental Progress & Sustainable Energy* **2014,** *33* (3), 756.

(73) Armstrong, L. M.; Gu, S.; Luo, K. H.; Mahanta, P. Multifluid Modeling of the Desulfurization Process within a Bubbling Fluidized Bed Coal Gasifier. *AIChE Journal* **2013,** *59* (6), 1952.

(74) Zhou, W.; Zhao, C. S.; Duan, L. B.; Qu, C. R.; Chen, X. P. Two-dimensional computational fluid dynamics simulation of coal combustion in a circulating fluidized bed combustor. *Chemical Engineering Journal* **2011,** *166* (1), 306.

(75) Zhong, H.; Zhang, J.; Zhu, Y.; Liang, S. Multi-fluid Modeling Biomass Fast Pyrolysis in the Fluidized-Bed Reactor Including Particle Shrinkage Effects. *Energy & Fuels* **2016,** *30* (8), 6440.

(76) Gai, C.; Zhang, Y.; Chen, W.-T.; Zhang, P.; Dong, Y. Thermogravimetric and kinetic analysis of thermal decomposition characteristics of low-lipid microalgae. *Bioresource Technology* **2013,** *150*, 139.

(77) Kim, S.-S.; Ly, H. V.; Choi, G.-H.; Kim, J.; Woo, H. C. Pyrolysis characteristics and kinetics of the alga Saccharina japonica. *Bioresource Technology* **2012,** *123*, 445.

(78) López-González, D.; Fernandez-Lopez, M.; Valverde, J. L.; Sanchez-Silva, L. Pyrolysis of three different types of microalgae: Kinetic and evolved gas analysis. *Energy* **2014,** *73*, 33.

(79) Azizi, S.; Mowla, D. In *International Journal of Chemical Reactor Engineering*, 2016; Vol. 14.

(80) Zhou, H.; Jensen, A. D.; Glarborg, P.; Jensen, P. A.; Kavaliauskas, A. Numerical modeling of straw combustion in a fixed bed. *Fuel* **2005,** *84* (4), 389.

(81) Boateng, A. A.; Mtui, P. L. CFD modeling of space-time evolution of fast pyrolysis products in a bench-scale fluidized-bed reactor. *Applied Thermal Engineering* **2012,** *33-34*, 190.

(82) Ranzi, E.; Cuoci, A.; Faravelli, T.; Frassoldati, A.; Migliavacca, G.; Pierucci, S.; Sommariva, S. Chemical kinetics of biomass pyrolysis. *Energy & Fuels* **2008,** *22* (6), 4292.

(83) Mellin, P.; Kantarelis, E.; Yang, W. Computational fluid dynamics modeling of biomass fast pyrolysis in a fluidized bed reactor, using a comprehensive chemistry scheme. *Fuel* **2014,** *117, Part A*, 704.

(84) Mellin, P.; Yu, X.; Yang, W.; Blasiak, W. Influence of Reaction Atmosphere (H2O, N2, H2, CO2, CO) on Fluidized-Bed Fast Pyrolysis of Biomass Using Detailed Tar Vapor Chemistry in Computational Fluid Dynamics. *Industrial & Engineering Chemistry Research* **2015,** *54* (33), 8344.

(85) Mellin, P.; Kantarelis, E.; Zhou, C.; Yang, W. Simulation of Bed Dynamics and Primary Products from Fast Pyrolysis of Biomass: Steam Compared to Nitrogen as a Fluidizing Agent. *Industrial & Engineering Chemistry Research* **2014,** *53* (30), 12129.

(86) Eri, Q.; Zhao, X.; Ranganathan, P.; Gu, S. Numerical simulations on the effect of potassium on the biomass fast pyrolysis in fluidized bed reactor. *Fuel* **2017,** *197*, 290.

(87) Trendewicz, A.; Evans, R.; Dutta, A.; Sykes, R.; Carpenter, D.; Braun, R. Evaluating the effect of potassium on cellulose pyrolysis reaction kinetics. *Biomass and Bioenergy* **2015,** *74*, 15.

(88) Ranganathan, P.; Gu, S. Computational fluid dynamics modelling of biomass fast pyrolysis in fluidised bed reactors, focusing different kinetic schemes. *Bioresource Technology* **2016,** *213*, 333.

(89) Di Blasi, C. Kinetic and Heat Transfer Control in the Slow and Flash Pyrolysis of Solids. *Industrial & Engineering Chemistry Research* **1996,** *35* (1), 37.

(90) Trendewicz, A.; Braun, R.; Dutta, A.; Ziegler, J. One dimensional steady-state circulating fluidized-bed reactor model for biomass fast pyrolysis. *Fuel* **2014,** *133*, 253.

(91) Humbird, D.; Trendewicz, A.; Braun, R.; Dutta, A. One-Dimensional Biomass Fast Pyrolysis Model with Reaction Kinetics Integrated in an Aspen Plus Biorefinery Process Model. *ACS Sustainable Chemistry & Engineering* **2017,** *5* (3), 2463.

(92) Zhu, H. P.; Zhou, Z. Y.; Yang, R. Y.; Yu, A. B. Discrete particle simulation of particulate systems: Theoretical developments. *Chemical Engineering Science* **2007,** *62* (13), 3378.

(93) Miller, R. S.; Bellan, J. Numerical Simulation of Vortex Pyrolysis Reactors for Condensable Tar Production from Biomass. *Energy & Fuels* **1998,** *12* (1), 25.

(94) Brown, A. L.; Dayton, D. C.; Nimlos, M. R.; Daily, J. W. Design and Characterization of an Entrained Flow Reactor for the Study of Biomass Pyrolysis Chemistry at High Heating Rates. *Energy & Fuels* **2001,** *15* (5), 1276.

(95) Simone, M.; Biagini, E.; Galletti, C.; Tognotti, L. Evaluation of global biomass devolatilization kinetics in a drop tube reactor with CFD aided experiments. *Fuel* **2009,** *88* (10), 1818.

(96) Ren, B.; Zhong, W.; Jin, B.; Yuan, Z.; Lu, Y. Computational Fluid Dynamics (CFD)–Discrete Element Method (DEM) Simulation of Gas–Solid Turbulent Flow in a Cylindrical Spouted Bed with a Conical Base. *Energy & Fuels* **2011,** *25* (9), 4095.

(97) Ku, X.; Li, T.; Løvås, T. Effects of Particle Shrinkage and Devolatilization Models on High-Temperature Biomass Pyrolysis and Gasification. *Energy & Fuels* **2015,** *29* (8), 5127.

(98) Li, T.; Wang, L.; Ku, X.; Güell, B. M.; Løvås, T.; Shaddix, C. R. Experimental and Modeling Study of the Effect of Torrefaction on the Rapid Devolatilization of Biomass. *Energy & Fuels* **2015,** *29* (7), 4328.

(99) Wagenaar, B. M.; Prins, W.; van Swaaij, W. P. M. Pyrolysis of biomass in the rotating cone reactor: modelling and experimental justification. *Chemical Engineering Science* **1994,** *49* (24, Part 2), 5109.

(100) Tchapda, A. H.; Pisupati, S. V. Characterization of an entrained flow reactor for pyrolysis of coal and biomass at higher temperatures. *Fuel* **2015,** *156*, 254.

(101) Johansen, J. M.; Gadsbøll, R.; Thomsen, J.; Jensen, P. A.; Glarborg, P.; Ek, P.; De Martini, N.; Mancini, M.; Weber, R.; Mitchell, R. E. Devolatilization kinetics of woody biomass at short residence times and high heating rates and peak temperatures. *Applied Energy* **2016,** *162*, 245.

(102) Ku, X.; Li, T.; Løvås, T. Eulerian–Lagrangian Simulation of Biomass Gasification Behavior in a High-Temperature Entrained-Flow Reactor. *Energy & Fuels* **2014,** *28* (8), 5184.

(103) Papadikis, K.; Gu, S.; Bridgwater, A. V.; Gerhauser, H. Application of CFD to model fast pyrolysis of biomass. *Fuel Processing Technology* **2009,** *90* (4), 504.

(104) Papadikis, K.; Gerhauser, H.; Bridgwater, A. V.; Gu, S. CFD modelling of the fast pyrolysis of an in-flight cellulosic particle subjected to convective heat transfer. *Biomass and Bioenergy* **2009,** *33* (1), 97.

(105) Papadikis, K.; Gu, S.; Fivga, A.; Bridgwater, A. V. Numerical Comparison of the Drag Models of Granular Flows Applied to the Fast Pyrolysis of Biomass. *Energy & Fuels* **2010,** *24* (3), 2133.

(106) Papadikis, K.; Gu, S.; Bridgwater, A. V. CFD modelling of the fast pyrolysis of biomass in fluidised bed reactors: Modelling the impact of biomass shrinkage. *Chemical Engineering Journal* **2009,** *149* (1), 417.

(107) Papadikis, K.; Gu, S.; Bridgwater, A. V. CFD modelling of the fast pyrolysis of biomass in fluidised bed reactors. Part B: Heat, momentum and mass transport in bubbling fluidised beds. *Chemical Engineering Science* **2009,** *64* (5), 1036.

(108) Papadikis, K.; Gu, S.; Bridgwater, A. V. A CFD approach on the effect of particle size on char entrainment in bubbling fluidised bed reactors. *Biomass and Bioenergy* **2010,** *34* (1), 21.

(109) Papadikis, K.; Gu, S.; Bridgwater, A. V. Computational modelling of the impact of particle size to the heat transfer coefficient between biomass particles and a fluidised bed. *Fuel Processing Technology* **2010,** *91* (1), 68.

(110) Papadikis, K.; Gu, S.; Bridgwater, A. V. 3D simulation of the effects of sphericity on char entrainment in fluidised beds. *Fuel Processing Technology* **2010,** *91* (7), 749.

(111) Papadikis, K.; Bridgwater, A. V.; Gu, S. CFD modelling of the fast pyrolysis of biomass in fluidised bed reactors, Part A: Eulerian computation of momentum transport in bubbling fluidised beds. *Chemical Engineering Science* **2008,** *63* (16), 4218.

(112) Bradbury, A. G. W.; Sakai, Y.; Shafizadeh, F. A kinetic model for pyrolysis of cellulose. *Journal of Applied Polymer Science* **1979,** *23* (11), 3271.

(113) Babu, B. V.; Chaurasia, A. S. Heat transfer and kinetics in the pyrolysis of shrinking biomass particle. *Chemical Engineering Science* **2004,** *59* (10), 1999.

(114) Rabinovich, O. S.; Borodulya, V. A.; Vinogradov, L. M.; Korban, V. V. Fast pyrolysis of an ensemble of biomass particles in a fluidized bed. *Journal of Engineering Physics and Thermophysics* **2010,** *83* (4), 742.

(115) Bruchmüller, J.; van Wachem, B. G. M.; Gu, S.; Luo, K. H.; Brown, R. C. Modeling the thermochemical degradation of biomass inside a fast pyrolysis fluidized bed reactor. *AIChE Journal* **2012,** *58* (10), 3030.

(116) Bruchmüller, J.; Luo, K. H.; van Wachem, B. G. M. Tar formation variations during fluidised bed pyrolytic biomass conversion. *Proceedings of the Combustion Institute* **2013,** *34* (2), 2373.

(117) Gollakota, A. R. K.; Subramanyam, M. D.; Kishore, N.; Gu, S. CFD simulations on the effect of catalysts on the hydrodeoxygenation of bio-oil. *RSC Advances* **2015,** *5* (52), 41855.

(118) Sheu, Y.-H. E.; Anthony, R. G.; Soltes, E. J. Kinetic studies of upgrading pine pyrolytic oil by hydrotreatment. *Fuel Processing Technology* **1988,** *19* (1), 31.

(119) Subramanyam, M. D.; Gollakota, A. R. K.; Kishore, N. CFD simulations of catalytic hydrodeoxygenation of bio-oil using Pt/Al2O3 in a fixed bed reactor. *RSC Advances* **2015,** *5* (110), 90354.

(120) Chu, P. L.; Vanderghem, C.; MacLean, H. L.; Saville, B. A. Process modeling of hydrodeoxygenation to produce renewable jet fuel and other hydrocarbon fuels. *Fuel* **2017,** *196*, 298.

(121) Snåre, M.; Kubičková, I.; Mäki-Arvela, P.; Eränen, K.; Murzin, D. Y. Heterogeneous Catalytic Deoxygenation of Stearic Acid for Production of Biodiesel. *Industrial & Engineering Chemistry Research* **2006,** *45* (16), 5708.

(122) Ma, J.; Zhang, M.; Su, B.; Wen, G.; Yang, Y.; Yang, Q.; Ren, Q. Numerical simulation of the entrained flow hydropyrolysis of coal in magnetically rotating plasma reactor. *Energy Conversion and Management* **2017,** *148*, 431.

CHAPTER 2 INTERMEDIATE TEMPERATURE WATER-GAS SHIFT KINETICS FOR HYDROGEN PRODUCTION

This chapter has been prepared as a manuscript for submission to an academic journal upon completion of the thesis.

I am the lead author on this manuscript. I was responsible for design and conducting the experimental kinetic testing. I was responsible for interpreting the experimental data and fitting the results to existing kinetic models. The other authors on this work are Drs. Nourredine Abdoulmoumine and Nicole Labbé.

Abstract

Biomass pyrolysis vapors have limited applications due chiefly to the high oxygen content. Hydrodeoxygenation has shown to be an efficient method to remove oxygen from pyrolysis vapors without sacrificing carbon. The goal of this chapter is to investigate hydrogen production for deoxygenation via the water-gas shift (WGS) reaction using carbon monoxide (CO), one of the significant non-condensable gases of pyrolysis, and steam, a by-product of hydrodeoxygenation, as reactants. The WGS reaction is typically carried out as a low-temperature shift (LTS;150-300 °C) or a high-temperature shift (HTS; 300-500 °C) with each shift using a different catalyst. In this chapter, the WGS experiments were performed at an intermediate temperature range of 200-400 °C over a copper (Cu) based catalyst using a bench-scale catalytic plug flow reactor (PFR) in a CO-lean environment (70 vol. % steam, 20 vol. % He, and 10 vol. % CO). The experimental temperatures were tested over three different weight hourly space velocities (WHSV =1220, 2040, and 6110 cm^3/g-min). Our results show that CO conversion increases with increasing temperature and catalyst weight, with a maximum CO conversion of 94% for temperatures >300 °C. Experimental conversion data were fitted to three proposed mechanistic models, two Langmuir-Hinshelwood (LH) and one redox mechanism, as well as a reduced order empirical power law model (ROM). The second LH model provided the best fit for each WHSV with apparent

activation energy between 45 and 65 kJ/mol. The ROM yielded activation energies between 20 and 41 kJ/mol.

2.1. Introduction

Over the past few decades, increasing environmental concern about climate change coupled with the energy and fuel demand of emerging economies, the forecasted depletion of crude petroleum reserves and the continuous instabilities in major oil-producing regions encouraged the development of sustainable and renewable energy systems[1,2]. In this regard, the production of bio-oil or biocrude through pyrolysis is attractive as an alternative to crude petroleum[3-5]. In general, when bio-oil is produced through conventional pyrolysis, it contains high oxygen content (~40-50 wt. %) while crude petroleum oil contains less than 1 wt. % [6,7]. The high oxygen content of bio-oil presents a problem for co-processing it with crude petroleum in existing refineries. Thus, bio-oil deoxygenation is vital to unlock its potential and leverage the capital already invested in existing refineries. It is presently carried out through hydrodeoxygenation (HDO) via either *ex-situ* on condensed bio-oil[8-10] or *in-situ* on vapors through advanced pyrolysis processes like hydropyrolysis[11,12]. In these advanced hydropyrolysis processes, external hydrogen is commonly introduced into the pyrolysis reactor at moderate pressures (20-40 bar) in the presence of an HDO catalyst to upgrade bio-oil vapors *in-situ*[13,14]. The derived bio-oil reportedly has significantly less oxygen content than conventional bio-oil with reported values as low as 0.4 wt. % [15]. The main drawback of these advanced processes is their hydrogen demand which at the moment is met by reforming natural gas and light hydrocarbons generated during pyrolysis[11,16]. Of these two sources of hydrogen, the former reduces the overall sustainability of the process by introducing a fossil-based fuel in the process, and the latter is not sufficient alone to meet the total hydrogen demand. Hydrous pyrolysis addresses this dilemma by integrating catalytic fast pyrolysis with the water-gas shift (WGS) reaction to produce additional hydrogen and HDO for oxygen removal in one-pot. This article is the first of a series that explores the feasibility of this concept through a combination of experimental and computational fluid dynamics coupled with discrete element modeling (CFD/DEM).

The WGS reaction, shown below, is widely used in several industrial applications to generate hydrogen as shown below. Carbon monoxide (CO) reacts with steam (H_2O) in the presence of a catalyst to produce carbon dioxide and hydrogen. This reaction is especially fitting in the context of pyrolysis since carbon monoxide is the most abundant non-condensable gas product during fast pyrolysis and water is produced during HDO.[17]

$$CO + H_2O \leftrightarrow H_2 + CO_2$$

When using syngas with a high concentration of carbon monoxide as observed in fast pyrolysis syngas (>50 vol. %)[17], the reaction is usually separated into two stages for increased conversion: high-temperature shift (HTS) and low-temperature shift (LTS)[18]. The high- and low-temperature shift are characterized by the reaction temperature as well as the catalyst used. The HTS takes place above 300 °C, and the most common catalyst used is an iron/chromium oxide [19,20]. The LTS occurs in the range of 150 to 300 °C and typically utilizes a copper-based catalyst[21]. Multiple kinetic models, such as the Langmuir-Hinshelwood (LH) and Eley-Rideal (ER), are available to calculate the rate of reaction for WGS[22]. The kinetics of the WGS reaction have been heavily investigated, however, there is still not a clear consensus on the kinetic model that best describes the kinetics[23,24]. In previous studies, Langmuir-Hinshelwood type models have been shown to provide the best experimental fit for the LTS over a Cu-based catalyst[22,25,26]. However, these types of models are not well-suited to be incorporated in computationally expensive pyrolysis process models (*i.e.,* CFD and DEM models). Furthermore, processes, like hydrous pyrolysis that are better represented by intermediate temperature shift (ITS) that covers both LTS and HTS temperature domains, must rely on several kinetic models to cover their reaction conditions space. This study looks to explore the middle ground between the LTS and HTS by developing mechanistic kinetics for WGS at intermediate temperatures (200-400 °C) approaching that of biomass pyrolysis and generating a unified reduced order model more easily and inexpensively integrated into hydrous pyrolysis reactor process models.

2.2. Materials and experimental methodology

2.2.1. Catalyst preparation and characterization

A commercial copper based, low-temperature WGS catalyst (HiFUEL® W220) was obtained from Alfa Aesar (Haverhill, MA, USA) and used for this study. The catalyst was first size reduced by a mortar and pestle and sieved to particle sizes between 0.425 and 0.595 mm (30-40 mesh). The catalyst was then characterized by physisorption of N_2 for surface area and pore volume. A Beckman Coulter surface area analyzer was used to determine the catalyst's Brunauer-Emmett-Teller (BET) surface area and total pore volume using nitrogen (N_2) as an adsorbate. The catalyst samples were outgassed for 60 min at 120 °C[27]. Additionally, the catalyst was tested for the optimal reduction temperature using a temperature program reduction (TPR) by a thermogravimetric analyzer (TGA) (Perkin Elmer, Pyris 1, Waltham, MA, USA)[28-30]. Approximately 30 mg of catalyst were placed on the sample pan to undergo TPR. The sample was then outgassed by heating to 105 °C at 25 °C/min, under a flow of helium, and maintained for 45 min to remove any adsorbate present in and on the catalyst. The outgassed sample was then heated from 105 to 400 °C at a rate of 2 °C/min while a reducing gas (90% N_2, 10% H_2) was flowed through the system. Upon completion, the sample's differential thermogravimetric curve was generated, using fityk software, and the peak minima, indicative of the maximum mass loss, was taken at the reduction temperature. All experiments were conducted in triplicate.

2.2.2. WGS experiments

The WGS experiments were carried in a plug flow reactor (PFR) system outfitted with a feed water delivery and steam generation system, as illustrated in Figure 2.1. The system consists of helium (He) and carbon monoxide (CO) supply lines, each equipped with a mass flow controller, a syringe pump for delivering water (Chemyx Inc., 10060, TX, USA), an evaporator for generating steam, a ½ inch (12.7 mm) tube plug flow reactor (PFR) housed in a split tubular furnace (Applied Test Systems, 3210, PA, USA), a set of condensers in series, and gas scrubbing tubes with activated carbon and drierite. The catalytic experiments were carried out at temperatures ranging from 200 to 400 °C in 50 °C temperature intervals. The temperature of the bed was monitored by a K-type thermocouple, which fed back to a proportional integral derivative (PID) controller that controls the furnace. In addition to the temperature, the space velocity (SV), reported as weight hourly space velocity (WHSV, $cm^3/(min\text{-}g)$), varied from 6110, 2040, and 1220. These WHSVs were calculated using the run conditions for 200 °C at 0.1 g, 0.3 g, and 0.5 g of active catalyst, respectively. An increase in the active catalyst weight at a given temperature reduces the WHSV. The reactor bed consisted of the copper-based catalyst diluted with alumina (γ-Al_2O_3), of the same particle size, for catalyst quantities under 0.5 g to provide the desired space velocity and avoid channeling in the reactor. Before every experiment, the catalyst is reduced *in-situ* using a gas mixture containing 10 vol. % hydrogen in nitrogen for 2 hours at the appropriate reduction temperature. Afterward, the CO and carrier gas (He) streams were controlled by two mass flow controllers before combining with a stream of water pumped into the evaporator by the syringe pump. The evaporator served to convert the water to steam as well as preheat the gases before

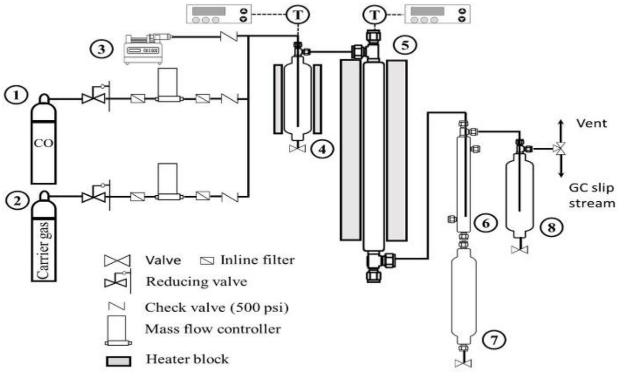

Figure 2.1. Experimental catalytic reactor setup. **1.** Carbon monoxide delivery lines; **2.** Inert gas (He) delivery line; **3.** High-pressure syringe water pump; **4.** Onboard steam generator with PID controlled heaters; **5.** Packed bed reactor with PID controller furnace heater; **6.** Shell and tube heat exchanger; **7.** Liquid collection reservoir with bottom drain valve; **8.** Overflow reservoir with a bottom drain valve.

reaching the reactor. Upon entering the reactor, the CO and steam reacted with the catalyst to produce hydrogen and carbon monoxide. The product gases were sent to a condenser to remove any excess steam from the product stream. In this chapter, the WGS experiments were carried out in a CO-lean environment (70 vol. % water, 20 vol. % He, and 10 vol. % CO) with a steam to carbon monoxide ratio (S/C) ranging from 5 to 7. This setup favors higher CO conversion due to CO acting as the limiting reactant.

At the outlet of the reactor, a slip stream of the effluent gas was continuously delivered to a 6 port actuating valve with a 1 ml sampling loop connected to a SRI TCD/FID/FPD gas chromatograph (GC) (SRI Instruments Inc., 8610C CA, USA) where the gas composition is analyzed continuously while the rest is vented to the exhaust. The thermal conductivity detector (TCD), with helium as the eluent, was used to analyze the products on a two-column system. The first column, a molecular sieve 13x column, analyzes a majority of the products, mainly H_2 and CO, while the second column, Hayesep-N column, is used to separate the CO_2.The temperature program was set with an initial temperature of 40 °C and is held for 10 minutes before ramping to 80 °C with a rate of 20 °C/min. The only peak of interest was the CO peak. Before each experiment, the GC was calibrated by using a calibration gas cylinder with the following concentrations: 5 vol. % CO, 5 vol. % CO_2, 5 vol. % N_2, 4 vol. % oxygen (O_2), 4 vol. % methane (CH_4), 4 vol. % H_2, and balance helium. The GC sampling loop was flushed with the calibration gas and the analysis was repeated at least three times. The area under the CO peaks was averaged to generate a single point calibration curve. Before starting each experiment, the initial flowrates of CO and He were sent to the GC to determine the initial concentration of the CO entering the reactor. The product stream was analyzed in the GC and the final CO concentration and conversion was determined for each experimental condition.

2.3. Kinetic analysis and modeling

2.3.1. Kinetic data analysis

Using well-documented WGS reaction mechanisms and data obtained from the laboratory scale experiments, kinetic parameters, such as the reaction order, rate constant, and activation energy, were derived [31]. Preliminary screening was carried out to test for external mass transfer and diffusion limitations for the proposed operating conditions. The mass transfer coefficient is inversely proportional to the boundary layer thickness. At lower velocities, the boundary layer is thick and the mass transfer rate limits the overall reaction rate while at higher velocities, reactants and products diffuse across the boundary layer quickly and mass transfer no longer limits the reaction[31]. If there are external mass transfer limitations, the higher gas velocities will lead to a higher conversion of CO.

External mass transfer limitations were assessed using the Carberry number (Ca)[32]. Ca is a ratio of the observed reaction rate to the maximum external mass transfer rate, shown below

$$Ca = \frac{\left(-r_{CO}^{obs}\right)\rho_c}{a' k_f C_{CO}^{b}} < 0.05$$

where $-r_{CO}^{obs}$ is the observed reaction rate, ρ_c is the density of the catalyst particle, a' is the specific external surface area of the catalyst particle, k_f is the mass transfer coefficient, and C_{CO}^{b} is the CO concentration in the bulk phase[33]. Furthermore, internal diffusion limitations tests were carried out using the Weisz-Prater criterion.

$$\frac{\left(-r_{CO}^{obs}\rho_c R_p^2\right)}{\left(D_e C_{As}\right)} \ll 1$$

where R_p is the mean radius of the catalyst particle (m), D_e is the effective diffusivity of CO in the catalyst (m^2/s), and C_{As} is the CO concentration on the catalyst surface. The effective diffusivity is calculated value using properties of the catalyst

$$D_e = \frac{\mathrm{D}\varphi_p \sigma}{\tau}$$

where D is the diffusion coefficient of CO in steam, φ_p is the porosity of the catalyst particle that is the product of the pore volume and the effective particle density and has a typical value of 0.4 for a catalyst pellet. σ is the constriction factor with a typical value of 0.8, and τ is the tortuosity with a typical value of 3.0[34,35]. If the criteria are satisfied, there is no external or internal diffusion limitation.

A nonlinear regression analysis was run on the data for each rate law tested. Model discrimination was carried out by applying multiple statistical tests, such as an F test, root mean squared error (RMSE), mean absolute error (MAE), a goodness of fit (FIT), and the Akaike Information Criterion (AIC). The optimum parameters were determined by minimizing the RMSE, MAE, and FIT.

2.3.2. Thermodynamic analysis

The WGS reaction is a reversible, exothermic reaction and thermal equilibrium is more rapidly achieved at higher temperatures[20]. Due to the exothermic nature of the reaction, the equilibrium constant as well as the carbon monoxide tend to decrease as temperature increases[36]

$$K_{eq} = \frac{[H_2]_{eq}[CO_2]_{eq}}{[CO]_{eq}[H_2O]_{eq}}$$

The equilibrium conversion of CO depends on the molar ratio of steam to CO supplied to the system. Therefore, the equilibrium constant can be rewritten

$$K_{eq} = \frac{X^2}{(1-X)(\frac{S}{C}-X)}$$

where X is the conversion of CO and S/C is the molar ratio of steam to CO (>1)[18]. A Matlab code was developed to determine the theoretical equilibrium constant and equilibrium conversion.

2.3.3. Kinetic models

Multiple kinetic models have been explored to determine the reaction kinetics and rate of reaction for the WGS reaction[22]. The mechanism of the WGS is primarily believed to proceed via one of two pathways: an associative mechanism or a redox mechanism. At lower temperatures (150-300 °C), the associative mechanism is accepted as prevalent at lower temperatures; however, the prevalent mechanism at high temperature (300-500 °C) is still debated with no consensus yet reached[37,38]. In the case of ITS, there are no proposed mechanisms specifically for the temperature range between LTS and HTS. Therefore, the kinetic mechanisms investigated were the ones that have shown to fit either the LTS or HTS. Three mechanistic models and one empirical model were proposed to fit the experimental results. In all models, the Arrhenius equation was used to model the temperature dependence of rate constants.

$$k = A_0 e^{\frac{-E_A}{RT}}$$

2.3.3.1. Langmuir-Hinshelwood mechanism and model

Armstrong and Hilditch proposed a model based on the Langmuir-Hinshelwood (LH) mechanism, which is of the associative form, in 1920[39] where CO and H_2O undergo adsorption onto the catalyst surface to produce intermediates that desorb off the catalyst into the products of CO_2 and H_2[40]. Researchers have tried to prove the exact form of the intermediates on the catalyst surface, such as formates[36,41]. Eight possible LH mechanisms with different active sites and intermediate formation steps were looked at for WGS kinetic modeling of the LTS and two associative mechanisms were shown to give the best fit[25]. Each LH mechanism was derived through the elementary reactions of the WGS. The first LH mechanism (LH1) is described by the following general reactions, where S represents a vacant adsorbing site on the catalyst and S* is indicative of an adsorbed species (note: the S* bonds are not true covalent bonds, therefore, the octet rule is not violated[25,40]:

$$CO + S \leftrightarrow CO * S$$

$$H_2O + S \leftrightarrow H_2O * S$$

$$CO * S + H_2O * S \leftrightarrow CO_2 * S + H_2 * S$$

$$H_2 * S \leftrightarrow H_2 + S$$

$$CO_2 * S \leftrightarrow CO_2 + S$$

For the LH1, the rate-limiting step (RLS) is the reaction between adsorbed species. The second LH mechanism (LH2) undergoes the same initial reactions of CO and H_2O adsorbing onto an active site. The differences between the two mechanisms occur from the adsorbed species reacting to form the intermediate and are carried on through the formation of CO_2 and H_2.

$$CO + S \leftrightarrow CO * S$$

$$H_2O + S \leftrightarrow H_2O * S$$

$$CO*S + H_2O*S \leftrightarrow COOH*S + H*S$$

$$COOH*S \leftrightarrow CO_2 + H*S$$

$$2H*S \leftrightarrow H_2 + 2S$$

The RLS for the second mechanism is also the surface reaction between the adsorbed species; however, this time to produce a formate intermediate and adsorbed hydrogen.

2.3.3.2. Redox mechanism and model

In 1949, Kulkova and Temkin hypothesized that the WGS proceeded through a series of reduction and oxidation reactions where water disassociated onto the catalyst surface to produce hydrogen, and then CO reduced the catalyst surface to produce CO_2.

$$H_2O + * \leftrightarrow H_2 + O*$$

$$CO + O* \leftrightarrow CO_2 + *$$

where * represents a vacant active site similar to in the associate mechanism[42]. The RLS for the proposed reduction mechanism consists of water adsorbing on an active site and releasing hydrogen while oxidizing the vacant site[26]. The regenerative, or reduction, mechanism provides a better fit for the HTS experiments rather than the LTS[43]. While the LH mechanisms have a consensus for being the mechanism for the LTS, the predominant mechanism is still up for debate. The HTS is typically thought to proceed through either a redox mechanism or an LH mechanism[44,45]. The intermediate nature of these experiments requires looking at models that have been proposed for both LTS and HTS.

2.3.3.3. Reduced order model

In addition to the mechanistic models, the experimental data were fit to a reduced order model (ROM) to better facilitate incorporation of the derived WGS kinetics into pyrolysis process models. ROMs are not dependent on specific reaction mechanism and are limited to specific operating conditions[24,40]. Consequently, the rate expression is based on experimental data and provides a simpler expression that is computationally lighter than the mechanistic expressions[46]. The rate expression for the empirical power law is represented by

$$-r_{CO} = kP_{CO}^{a}P_{H_2O}^{b}P_{H_2}^{c}P_{CO_2}^{d}(\beta)$$

where a, b, c, and d are the reaction orders for CO, H_2O, H_2, and CO_2, respectively. P_i is the partial pressure of each species. The approach to equilibrium, β, is described below.

$$\beta = 1 - \frac{P_{H_2}P_{CO_2}}{P_{CO}P_{H_2O}}\frac{1}{K_e}$$

2.3.4. Parameter estimation and model discrimination

A numerical optimization method was adopted for estimating the parameters of both the mechanistic models and the empirical power law. A Matlab code was developed that utilizes an ordinary differential equation (ODE) subroutine and non-linear regression analysis, using the non-linear least squares solver function (lsqcurvefit), which has been used previously for kinetic studies. The code was used to fit the experimental data to the proposed kinetic models[47]. The lsqcurvefit function solves for parameters by minimizing the sum of squared residuals. Initial guesses for parameters were taken from existing kinetic studies on the LTS WGS[25,26,40]. Minimizing the RMSE, MAE, FIT, and AIC was the criteria for determining the optimum parameters.

$$RMSE = \sqrt{\frac{1}{N}\sum_{i=1}^{N}\left(y_i - F(k, x_i)\right)^2}$$

$$MAE = \frac{1}{N}\sum_{i=1}^{N}\left|y_i - F(k, x_i)\right|$$

$$FIT = 100\,\frac{\sum_{i=1}^{N}\frac{\left(y_i - F(k, x_i)\right)^2}{N^2}}{experimental_{max}}$$

$$AIC = N * log\left(\frac{\sum\left(y_i - F(k, x_i)\right)^2}{N}\right) + 2k$$

where $F(k, x_i)$ are the values calculated by the model, k is the number of parameters being optimized, N is the number of observations, and y_i is the experiental data, and $experimental_{max}$ is the maximum observed value[48,49]. Conversion data from the GC is only available for every 13 minutes. Therefore, data points for the range of CO conversion were interpolated using a piecewise cubic Hermite interpolating polynomial (PCHIP) function. After interpolating, 100 data points were used for parameter optimization.

Model discrimination was carried out through comparison of the results of all the statistical tests. The AIC[50] takes the number of parameters and the sample size and the residual sum of squares into account. This model allows for discrimination of different models with varying numbers of parameters. A low AIC value correlates to a good statistical fit for the model. Therefore, the model with the lowest AIC was determined to fit the data best.

2.4. Results

2.4.1. Catalyst characterization

The composition of the WGS catalyst used in this study is shown in Table 2.1. It is comprised of copper (II) oxide, zinc oxide, aluminum oxide, and carbon in a weight percent ratio of 52:30:17:1, respectively. Cu-based catalysts have been studied extensively for low-temperature WGS reactions; however, the chemical composition of the oxide components can differ greatly. Previous studies have used similar catalysts containing $CuO/ZnO/Al_2O_3$, but with a lower CuO content[24,25,36]. Others impregnated copper onto a supported metal oxide with a maximum loading of 20 wt. %[21,51,52]. The results of the BET surface area analysis are shown in Table 2.2. Gines et al. characterized several $CuO/ZnO/Al_2O_3$ catalysts for BET surface area with compositions relatively comparable to the catalyst in this study and found them to have slightly lower surface areas (50-55 m^2/g), which can be attributed to the difference in CuO/ZnO wt. % ratio[53]. Ayastuy et al. reported a BET surface area of 92 m^2/g and a pore volume of 0.29 cm^3/g but used a catalyst with a significant difference in elemental composition as well (24.9/43.7/31.4 wt. % $CuO/ZnO/Al_2O_3$)[25]. Shen et al. used a $CuO/ZnO/Al_2O_3$ catalyst with a BET surface area of 77 m^2/g, which is closer to what has been measured here[54].

Additionally, the catalyst was tested for the optimal reduction temperature using temperature program reduction (TPR). TPR produced a thermogravimetric (TG) curve mapping the mass loss of the sample versus temperature. The TG data were then converted to a differential thermogravimetric (DTG) curve, which showed the rate of mass loss versus temperature, and fit to a curve using fityk software. A peak for the derivative of mass loss is indicative of reduction because the catalyst is initially oxidized. As hydrogen is flown over the catalyst at increasing temperatures, hydrogen will reduce the catalyst and remove the oxygen present in the oxide

Table 2.1. Composition of the commercial Cu-based catalyst.

Species	**Percent (wt. %)**
Copper Oxide (CuO)	52.0
Zinc Oxide (ZnO)	30.0
Aluminum Oxide (Al_2O_3)	17.0
Graphite (C)	1.0

Table 2.2. Catalyst characterization results.

Property	**Fresh**
Total Pore Volume (ml/g)	0.22(0.01)
BET Surface Area (m^2/g)	62.2(0.95)

()- indicates standard deviation

resulting in a reduction of the catalyst as well as a loss of mass. The derivative of the mass loss peak is therefore indicative of the true reduction temperature for the catalyst. The TPR results are shown below in Figure 2.2 with an optimal TPR temperature of 256 ± 8 °C. This value was similar to the catalyst supplier recommended maximum reduction temperature of 270 °C.

2.4.2. Mass transfer and diffusion limitations

The reaction setup was tested for external mass transfer and internal diffusion limitations. External mass transfer limitations were tested for using the Carberry number (Ca)[55,56]. Ca is a ratio of the observed reaction rate to the maximum external mass transfer rate. The values for Ca were found to be significantly lower than 0.05; therefore, it can be assumed external mass transfer limitations were not present[55]. The diffusion transfer limitations were tested for using the Wheeler-Weisz criterion. The Wheeler-Weisz yielded values significantly less than 0.10. Therefore, diffusion limitations were not present in the WGS experiments.

2.4.3. Effect of temperature and catalyst weight on carbon monoxide conversion

The bench-scale WGS reaction was carried out for five temperatures at three different WHSVs for a total of 15 experiments. Figure 2.3 displays CO conversion as a function of temperature for each WHSV. The conversion of CO was seen to be affected by both temperature and catalyst weight (decreasing WHSV). In this study, CO conversion increased with increased temperature and catalyst weight until reaching a maximum conversion of 94% at temperatures greater than 300 °C. For conditions hotter than 300 °C, the difference in CO conversion between the varying WHSVs decreased to a point where there was no significant difference in conversion between WHSV #2 (2040 cm^3/g-min) and WHSV #3 (1220 cm^3/g-min).

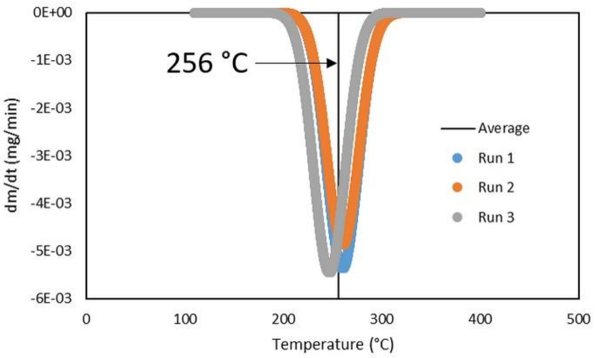

Figure 2.2. Results from the TPR of the commercial Cu-based catalyst showing derivate of mass as a function of temperature.

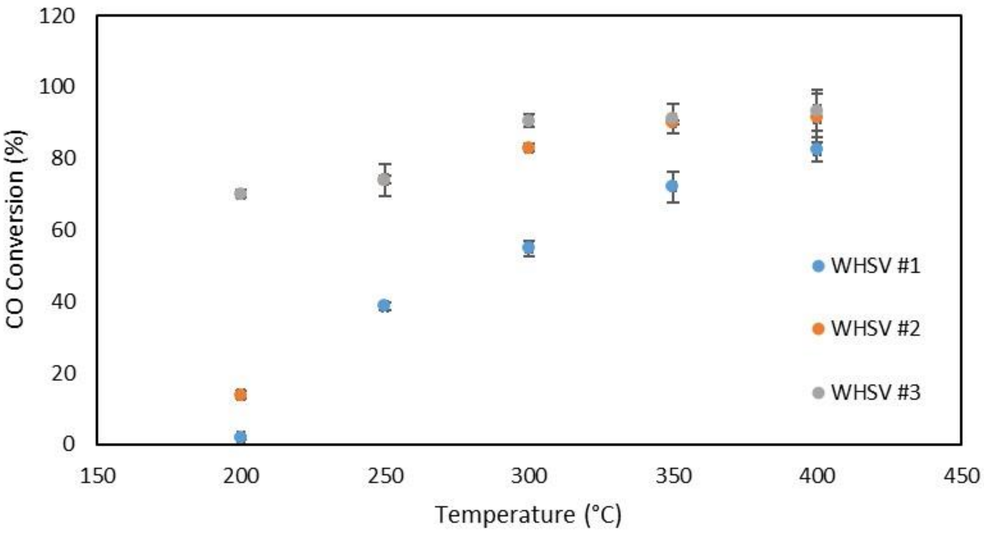

Figure 2.3 CO conversion (%) as a function of temperature (°C) over different WHSVs (WHSV #1 = 1220 cm^3/g-min, WHSV #2 = 2040 cm^3/g-min, and WHSV #3 = 6110 cm^3/g-min).

WHSV #1 (6110 cm^3/g-min) produced significantly less CO conversion than the other two. This can be attributed to the small amount of active catalyst present in the reactor bed. To determine how catalyst weight affects CO conversion, Figure 2.4 maps the inverse WHSV (W/F), where W is the weight of active catalyst (g) and F is the total flow rate (cm^3/min) against CO conversion. Much like in Figure 2.3, the overall trend of increasing CO conversion with increased catalyst weight and temperature remains the same. The conversion plateau around 94% still appeared, with 350 °C producing a higher conversion than 400 °C. The conversion drop at 400 °C is most likely due to experimental error as 400 °C had a higher standard deviation (8%) compared to the other temperatures (<5%). This behavior is in agreement with that CO conversion increases with an increasing time factor, which corresponds to an increase in residence time[18]. Overall, the increase of CO conversion with increasing catalyst weight and temperature is in agreement with previous studies[25,26,57,58].

2.4.4. Kinetic model parameter optimization

Four possible kinetic models were evaluated through non-linear regression to obtain optimized parameters that best fit the experimental data. The rate expressions for each model are shown in Table 2.3. The experiments were carried out by measuring CO concentration and volumetric flow rate without partial pressure measurements. Therefore, assuming the gases behave ideally, the ideal gas law was used to convert the partial pressure of each species into terms of initial CO concentration (CO_0), CO conversion (X), the molar ratio of steam to CO (θ), the ideal gas law constant (R), and temperature (T).

$$P_{CO} = CO_0(1 - X)RT$$

$$P_{H_2O} = CO_0(\theta - X)RT$$

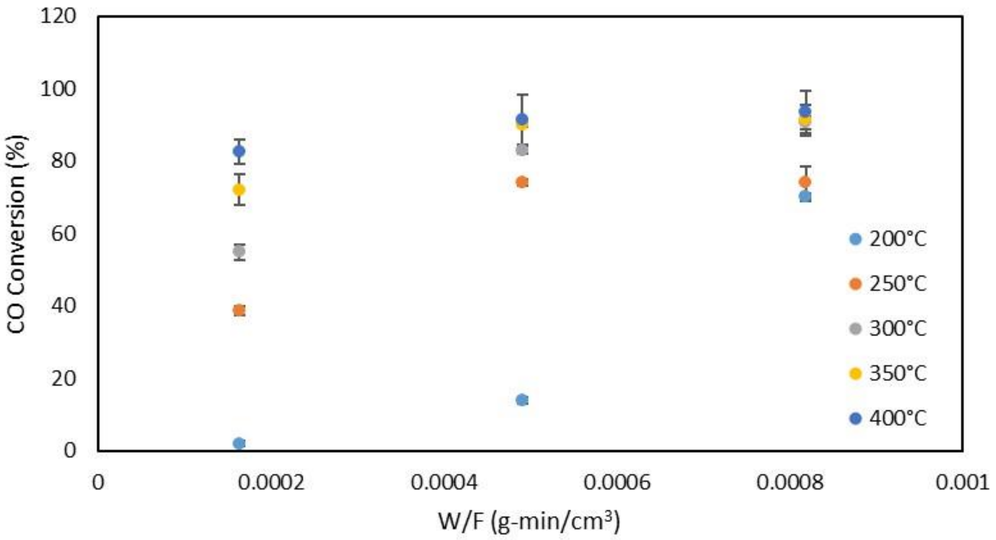

Figure 2.4 CO conversion as a function of inverse WHSV (g-min/cm^3) from 200-400 °C.

Table 2.3. Rate law expressions for each kinetic model tested.

Kinetic Model	Rate Equation
Langmuir-Hinshelwood 1	$-r_{CO} = \dfrac{k\left(P_{CO}P_{H_2O} - \dfrac{P_{CO_2}P_{H_2}}{K_e}\right)}{\left(1 + K_{CO}P_{CO} + K_{H_2O}P_{H_2O} + K_{H_2}P_{H_2} + K_{CO_2}P_{CO_2}\right)^2}$
Langmuir-Hinshelwood 2	$-r_{CO} = \dfrac{k\left(P_{CO}P_{H_2O} - \dfrac{P_{CO_2}P_{H_2}}{K_e}\right)}{\left(1 + K_{CO}P_{CO} + K_{H_2O}P_{H_2O} + {K_{H_2}}^{0.5}{P_{H_2}}^{0.5} + K_{CO_2}P_{CO_2}{P_{H_2}}^{0.5}\right)^2}$
Redox	$-r_{CO} = \dfrac{k\left(P_{H_2O} - \dfrac{P_{CO_2}P_{H_2}}{P_{CO}K_e}\right)}{1 + \dfrac{K_{CO}P_{CO_2}}{P_{CO}}}$
Power-Law	$-r_{CO} = kP_{CO}^{a}P_{H_2O}^{b}P_{H_2}^{c}P_{CO_2}^{d}(1-\beta)$

$$P_{H_2} = P_{CO_2} = CO_0(X)RT$$

The first associate mechanism proposed, LH1, did not provide a good fit for several of the experimental conditions and was eliminated on that basis (AIC = -226 and FIT = 1.49). LH2 has ten parameters to be optimized while the redox mechanism has four, and the power law has five. Kinetic parameters were determined for each WHSV over the range from 200-400 °C, and the results are shown in Table 2.4, Table *2.5*, and Table *2.6*. For all models, the activation energy decreased as the catalyst weight was increased. The estimated activation energy for the LH2, power law, and redox models ranged from 45-65 kJ/mol, 20-41 kJ/mol, and 73-76 kJ/mol, respectively, depending on the WHSV. For the power law, the reaction order with respect to carbon monoxide and steam was shown to be the most sensitive to experimental conditions fluctuating between 0.467-1.029 and 0.472-0.634 respectively, whereas the reaction orders for the others remained relatively constant.

2.4.5. Model discrimination

The mean absolute error (MAE), root mean squared error (RMSE), and goodness of fit (FIT) analyses were used to compare how well each model fit the experimental data. Further discrimination of the models was accomplished using the Akaike information criterion (AIC). This allowed for comparison between models with a different number of parameters.The results of each statistical test are shown in Table 2.7. All of the tests are negatively-oriented, therefore lower values indicate a better fit. Upon comparison of the three tests, the three models give similar values. However, the LH2 model provided the best overall fit to the experimental data over each WHSV for averaged conditions between 200-400 °C. The empirical power law is the second best fit to the experimental data over each WHSV. An associative mechanism as well as an empirical power law

Table 2.4. Calculated parameters for WHSV #1, 6170 cm^3/(min-g), for the proposed kinetic models.

Parameter	Langmuir-Hinshelwood 2	Redox	Power Law
$\ln(k_0)$	17.0 (0.15)	17.0 (0.23)	3.18 (0.79)
E_a	65.5 (5.4)	76.2 (6.7)	40.8 (1.6)
$\ln(K_{co})$	-2.26 (0.68)		-
ΔH_{co}	18.9 (9.9)		-
$\ln(K_{H_2O})$	-3.81 (1.6)	-	-
ΔH_{H_2O}	14.6 (2.8)	-	-
$\ln(K_{H_2})$	-3.53 (0.53)	-	-
ΔH_{H_2}	21.2 (12.5)	-	-
$\ln(K_{CO_2})$	-3.53 (4.1)	-2.14 (1.27)	-
ΔH_{CO_2}	38.3 (9.3)	-39.4 (12.6)	-
a	-	-	0.47 (0.14)
b	-	-	0.52 (0.13)
c	-	-	-0.46 (0.11)
d	-	-	-0.65 (0.15)

Note: Values in parenthesis represent the standard deviation

Table 2.5. Calculated parameters for WHSV #2, 2036 cm^3/(min-g), for the proposed kinetic models.

Parameter	Langmuir-Hinshelwood 2	Redox	Power Law
$\ln(k_0)$	16.9 (0.32)	17.1 (1.2)	3.97 (1.8)
E_a	49.4 (6.3)	76.0 (4.4)	32.7 (4.2)
$\ln(K_{co})$	-2.23 (2.7)	-	-
ΔH_{co}	19.5 (12.8)	-	-
$\ln(K_{H_2O})$	-1.43 (0.86)	-	-
ΔH_{H_2O}	15.9 (5.2)	-	-
$\ln(K_{H_2})$	-1.48 (0.91)	-	-
ΔH_{H_2}	30.1 (20.8)	-	-
$\ln(K_{CO_2})$	-1.21 (1.1)	-3.98 (2.2)	-
ΔH_{CO_2}	36.1 (8.8)	-45.1 (14.1)	-
a	-	-	0.95 (0.43)
b	-	-	0.47 (0.15)
c	-	-	-0.55 (0.08)
d	-	-	-0.70 (0.063)

Note: Values in parenthesis represent the standard deviation

Table 2.6. Calculated parameters for WHSV #3, 1221 cm^3/(min-g), for the proposed kinetic models.

Parameter	Langmuir-Hinshelwood 2	Redox	Power Law
$\ln(k_0)$	17.3 (1.0)	16.8 (0.19)	1.42 (0.60)
E_a	44.7 (1.7)	73.4 (4.0)	20.2 (2.1)
$\ln(K_{co})$	0.491 (0.84)	-	-
ΔH_{co}	26.6 (4.5)	-	-
$\ln(K_{H_2O})$	-2.25 (1.1)	-	-
ΔH_{H_2O}	14.1 (3.9)	-	-
$\ln(K_{H_2})$	-3.23 (2.8)	-	-
ΔH_{H_2}	18.8 (5.0)	-	-
$\ln(K_{CO_2})$	-0.954 (0.57)	-5.46 (2.9)	-
ΔH_{CO_2}	40.3 (5.4)	-47.8 (8.6)	-
a	-	-	1.03 (0.22)
b	-	-	0.63 (0.14)
c	-	-	-0.50 (0.015)
d	-	-	-0.67 (0.040)

Note: Values in parenthesis represent the standard deviation

Table 2.7. Goodness of fit results for kinetic models over each WHSV.

	Langmuir-Hinshelwood 2			Redox			Power Law		
	WHSV1	WHSV2	WHSV3	WHSV1	WHSV2	WHSV3	WHSV1	WHSV2	WHSV3
RMSE	0.045	0.048	0.034	0.059	0.060	0.071	0.064	0.056	0.074
MAE	0.038	0.040	0.030	0.050	0.049	0.058	0.053	0.045	0.052
FIT	0.004	0.003	0.001	0.007	0.005	0.007	0.010	0.004	0.007
AIC	-273.7	-270.5	-274.1	-261.5	-252.4	-254.4	-276.5	-231.1	-222.8

have been shown to provide the best fits in several previous works[25,26,41]. The power law provides a simpler kinetic expression than the LH2 mechanism and makes for a lighter computational load when incorporated into a process simulation. Moving forward, the empirical power law will be the most useful for determining the amount of hydrogen that can be generated from the non-condensable gases, mainly CO, produced during biomass pyrolysis while still maintaining kinetic accuracy.

2.5. Conclusions

The kinetics of the water-gas shift reaction over a Cu-based catalyst at intermediate conditions, near hydrous pyrolysis operating temperatures, were explored. At temperatures from 200-400°C, three WHSVs, two mechanistic kinetic models, and an empirical power law were fit to the experimental data. Comparing goodness of fit tests and the AIC, the associated Langmuir-Hinshelwood mechanism was shown to be the best fit. The LH2 model yielded apparent activation energy between 45-65 kJ/mol over varying WHSVs whereas the power law yielded activation energies between 20-41. The reaction order for CO_2, H_2, and H_2O remained stable over all WHSVs while the exponents for CO fluctuated from 0.46-1.00. The next step in this research is to use the CO concentration in pyrolysis vapors to determine the amount of hydrogen that will be available for hydrous pyrolysis.

List of references

(1) Klass, D. L. *Biomass for Renewable Energy, Fuels, and Chemicals*; Elsevier Science, 1998.
(2) Abas, N.; Kalair, A.; Khan, N. Review of fossil fuels and future energy technologies. *Futures* **2015,** *69*, 31.
(3) Blin, J.; Volle, G.; Girard, P.; Bridgwater, T.; Meier, D. Biodegradability of biomass pyrolysis oils: Comparison to conventional petroleum fuels and alternatives fuels in current use. *Fuel* **2007,** *86* (17), 2679.
(4) Safana, A.; Idowu, I. I.; Saadu, I.; Adamu, B.; Musa, I. M.; Habibu, S. Potential Application of Pyrolysis Bio-Oil as a Substitute for Diesel and Petroleum Fuel. *Journal of Petroleum Engineering & Technology* **2018,** *7* (3), 19.
(5) Makarfi Isa, Y.; Ganda, E. T. Bio-oil as a potential source of petroleum range fuels. *Renewable and Sustainable Energy Reviews* **2018,** *81*, 69.
(6) Oasmaa, A.; Czernik, S. Fuel oil quality of biomass pyrolysis oils-State of the art for the end users. *Energy & Fuels* **1999,** *13* (4), 914.
(7) Dayton, D. C.; Carpenter, J.; Farmer, J.; Turk, B.; Gupta, R. Biomass hydropyrolysis in a pressurized fluidized bed reactor. *Energy & Fuels* **2013,** *27* (7), 3778.
(8) Lee, H.; Kim, H.; Yu, M. J.; Ko, C. H.; Jeon, J.-K.; Jae, J.; Park, S. H.; Jung, S.-C.; Park, Y.-K. Catalytic Hydrodeoxygenation of Bio-oil Model Compounds over Pt/HY Catalyst. *Scientific Reports* **2016,** *6*, 28765.
(9) Cheng, S.; Wei, L.; Julson, J.; Rabnawaz, M. Upgrading pyrolysis bio-oil through hydrodeoxygenation (HDO) using non-sulfided Fe-Co/SiO2 catalyst. *Energy Conversion and Management* **2017,** *150*, 331.
(10) Shemfe, M. B.; Gu, S.; Ranganathan, P. Techno-economic performance analysis of biofuel production and miniature electric power generation from biomass fast pyrolysis and bio-oil upgrading. *Fuel* **2015,** *143*, 361.
(11) Marker, T. L.; Felix, L. G.; Linck, M. B.; Roberts, M. J. Integrated hydropyrolysis and hydroconversion (IH2) for the direct production of gasoline and diesel fuels or blending components from biomass, part 1: Proof of principle testing. *Environmental Progress & Sustainable Energy* **2012,** *31* (2), 191.
(12) Balagurumurthy, B.; Oza, T. S.; Bhaskar, T.; Adhikari, D. K. Renewable hydrocarbons through biomass hydropyrolysis process: challenges and opportunities. *Journal of Material Cycles and Waste Management* **2013,** *15* (1), 9.
(13) Resende, F. L. P. Recent advances on fast hydropyrolysis of biomass. *Catalysis Today* **2016,** *269*, 148.
(14) Balagurumurthy, B.; Singh, R.; Oza, T. S.; Shiva Kumar, K. L. N.; Saran, S.; Bahuguna, G. M.; Chauhan, R. K.; Bhaskar, T. Effect of pressure and temperature on the hydropyrolysis of cotton residue. *Journal of Material Cycles and Waste Management* **2014,** *16* (3), 442.
(15) Marker, T. L.; Felix, L. G.; Linck, M. B.; Roberts, M. J.; Ortiz-Toral, P.; Wangerow, J. Integrated hydropyrolysis and hydroconversion (IH2®) for the direct production of gasoline and diesel fuels or blending components from biomass, part 2: Continuous testing. *Environmental Progress & Sustainable Energy* **2014,** *33* (3), 762.
(16) Linck, M.; Felix, L.; Marker, T.; Roberts, M. Integrated biomass hydropyrolysis and hydrotreating: a brief review. *Wiley Interdisciplinary Reviews: Energy and Environment* **2014,** *3* (6), 575.

(17) Mante, O. D.; Agblevor, F. A.; Oyama, S. T.; McClung, R. The influence of recycling non-condensable gases in the fractional catalytic pyrolysis of biomass. *Bioresource Technology* **2012,** *111*, 482.

(18) Chein, R. Y.; Lin, Y. H.; Chen, Y. C.; Chyou, Y. P.; Chung, J. N. Study on water–gas shift reaction performance using Pt-based catalysts at high temperatures. *International Journal of Hydrogen Energy* **2014,** *39* (33), 18854.

(19) Rhodes, C.; Peter Williams, B.; King, F.; Hutchings, G. J. Promotion of Fe3O4/Cr2O3 high temperature water gas shift catalyst. *Catalysis Communications* **2002,** *3* (8), 381.

(20) LeValley, T. L.; Richard, A. R.; Fan, M. The progress in water gas shift and steam reforming hydrogen production technologies – A review. *International Journal of Hydrogen Energy* **2014,** *39* (30), 16983.

(21) Grenoble, D. C.; Estadt, M. M.; Ollis, D. F. The chemistry and catalysis of the water gas shift reaction. *Journal of Catalysis* **1981,** *67* (1), 90.

(22) Podolski, W. F.; Kim, Y. G. Modeling the Water-Gas Shift Reaction. *Industrial & Engineering Chemistry Process Design and Development* **1974,** *13* (4), 415.

(23) Fujita, S.-I.; Usui, M.; Takezawa, N. Mechanism of the reverse water gas shift reaction over Cu/ZnO catalyst. *Journal of Catalysis* **1992,** *134* (1), 220.

(24) Salmi, T.; Hakkarainen, R. Kinetic Study of the Low-Temperature Water-Gas Shift Reaction over a Cu—ZnO Catalyst. *Applied Catalysis* **1989,** *49* (2), 285.

(25) Ayastuy, J. L.; Gutiérrez-Ortiz, M. A.; González-Marcos, J. A.; Aranzabal, A.; González-Velasco, J. R. Kinetics of the Low-Temperature WGS Reaction over a CuO/ZnO/Al2O3 Catalyst. *Industrial & Engineering Chemistry Research* **2005,** *44* (1), 41.

(26) Mendes, D.; Chibante, V.; Mendes, A.; Madeira, L. M. Determination of the Low-Temperature Water−Gas Shift Reaction Kinetics Using a Cu-Based Catalyst. *Industrial & Engineering Chemistry Research* **2010,** *49* (22), 11269.

(27) Li, S.; Lu, Y.; Guo, L.; Zhang, X. Hydrogen production by biomass gasification in supercritical water with bimetallic Ni–M/γAl2O3 catalysts (M = Cu, Co and Sn). *International Journal of Hydrogen Energy* **2011,** *36* (22), 14391.

(28) Bhatia, S.; Beltramini, J.; Do, D. D. Temperature programmed analysis and its applications in catalytic systems. *Catalysis Today* **1990,** *7* (3), 309.

(29) Umegaki, T.; Kojima, Y.; Omata, K. Effect of Oxide Coating on Performance of Copper-Zinc Oxide-Based Catalyst for Methanol Synthesis via Hydrogenation of Carbon Dioxide. *Materials* **2015,** *8* (11), 5414.

(30) Zhang, C.-H.; Yang, Y.; Teng, B.-T.; Li, T.-Z.; Zheng, H.-Y.; Xiang, H.-W.; Li, Y.-W. Study of an iron-manganese Fischer–Tropsch synthesis catalyst promoted with copper. *Journal of Catalysis* **2006,** *237* (2), 405.

(31) Fogler, H. S. *Essentials of Chemical Reaction Engineering*; Prentice Hall, 2011.

(32) Carberry, J. J. In *Catalysis: Science and Technology*; Anderson, J. R.;Boudart, M., Eds.; Springer Berlin Heidelberg: Berlin, Heidelberg, 1987, DOI:10.1007/978-3-642-93278-6_3 10.1007/978-3-642-93278-6_3.

(33) Hanefeld, U.; Lefferts, L. *Catalysis: An Integrated Textbook for Students*; Wiley, 2017.

(34) Prasad, V.; Karim, A. M.; Arya, A.; Vlachos, D. G. Assessment of Overall Rate Expressions and Multiscale, Microkinetic Model Uniqueness via Experimental Data Injection: Ammonia Decomposition on Ru/γ-Al2O3 for Hydrogen Production. *Industrial & Engineering Chemistry Research* **2009,** *48* (11), 5255.

(35) Fogler, H. S. *Elements of Chemical Reaction Engineering*; Prentice Hall PTR, 2006.

(36) Rhodes, C.; Hutchings, G. J.; Ward, A. M. Water-gas shift reaction: finding the mechanistic boundary. *Catalysis Today* **1995,** *23* (1), 43.

(37) Smirniotis, P.; Gunugunuri, K. *Water Gas Shift Reaction: Research Developments and Applications*; Elsevier Science, 2015.

(38) Zhu, M.; Wachs, I. E. Iron-Based Catalysts for the High-Temperature Water–Gas Shift (HT-WGS) Reaction: A Review. *ACS Catalysis* **2016,** *6* (2), 722.

(39) Armstrong, E.; Hilditch, T. A Study of Catalytic Actions at Solid Surfaces. IV. The Interaction of Carbon Monoxide and Steam as Conditions by Iron Oxide and by Copper. *Proceedings of the Royal Society of London. Series A, Containing Papers of a Mathematical and Physical Character (1905-1934)* **1920,** *97* (684), 265.

(40) Mohammady Maklavany, D.; Shariati, A.; Roozbehani, B.; Khosravi Nikou, M. R. Kinetic Modeling of Low Temperature Water-Gas Shift Reaction using gPROMS. *American Journal of Oil and Chemical Technologies* **2016,** *4* (2).

(41) Choi, Y.; Stenger, H. G. Water gas shift reaction kinetics and reactor modeling for fuel cell grade hydrogen. *Journal of Power Sources* **2003,** *124* (2), 432.

(42) Kulkova, N. V.; Temkin, M. I. J. *Zhurnal Fizicheskoi Khimii* **1949,** *23*, 695.

(43) Salmi, T.; Lindfors, L. E.; Boström, S. Modelling of the high temperature water gas shift reaction with stationary and transient experiments. *Chemical Engineering Science* **1986,** *41* (4), 929.

(44) Lei, Y.; Cant, N. W.; Trimm, D. L. Kinetics of the water–gas shift reaction over a rhodium-promoted iron–chromium oxide catalyst. *Chemical Engineering Journal* **2005,** *114* (1), 81.

(45) Keiski, R. L.; Salmi, T.; Niemistö, P.; Ainassaari, J.; Pohjola, V. J. Stationary and transient kinetics of the high temperature water-gas shift reaction. *Applied Catalysis A: General* **1996,** *137* (2), 349.

(46) Gökaliler, F.; Önsan, Z. I.; Aksoylu, A. E. Power-law type rate expression for WGS reaction over Au–Re/CeO2 catalyst under realistic fuel processor conditions. *Catalysis Communications* **2013,** *39* (Supplement C), 70.

(47) Castaño, P.; Arandes, J. M.; Pawelec, B.; Fierro, J. L. G.; Gutiérrez, A.; Bilbao, J. Kinetic Model Discrimination for Toluene Hydrogenation over Noble-Metal-Supported Catalysts. *Industrial & Engineering Chemistry Research* **2007,** *46* (23), 7417.

(48) Oyedeji, O.; Daw, C. S.; Labbe, N.; Ayers, P.; Abdoulmoumine, N. Kinetics of the release of elemental precursors of syngas and syngas contaminants during devolatilization of switchgrass. *Bioresource Technology* **2017,** *244* (Part 1), 525.

(49) Granada, E.; Eguía, P.; Comesaña, J. A.; Patiño, D.; Porteiro, J.; Miguez, J. L. Devolatilization behaviour and pyrolysis kinetic modelling of Spanish biomass fuels. *Journal of Thermal Analysis and Calorimetry* **2013,** *113* (2), 569.

(50) Akaike, H. A new look at the statistical model identification. *IEEE Transactions on Automatic Control* **1974,** *19* (6), 716.

(51) Yahiro, H.; Murawaki, K.; Saiki, K.; Yamamoto, T.; Yamaura, H. Study on the supported Cu-based catalysts for the low-temperature water–gas shift reaction. *Catalysis Today* **2007,** *126* (3), 436.

(52) Jeong, D.-W.; Jang, W.-J.; Shim, J.-O.; Han, W.-B.; Roh, H.-S.; Jung, U. H.; Yoon, W. L. Low-temperature water–gas shift reaction over supported Cu catalysts. *Renewable Energy* **2014,** *65*, 102.

(53) Ginés, M. J. L.; Amadeo, N.; Laborde, M.; Apesteguía, C. R. Activity and structure-sensitivity of the water-gas shift reaction over CuZnAl mixed oxide catalysts. *Applied Catalysis A: General* **1995,** *131* (2), 283.

(54) Shen, J.-P.; Song, C. Influence of preparation method on performance of Cu/Zn-based catalysts for low-temperature steam reforming and oxidative steam reforming of methanol for H2 production for fuel cells. *Catalysis Today* **2002,** *77* (1), 89.

(55) Yuan, G.; Keane, M. A. Liquid phase catalytic hydrodechlorination of 2,4-dichlorophenol over carbon supported palladium: an evaluation of transport limitations. *Chemical Engineering Science* **2003,** *58* (2), 257.

(56) Pérez-Ramírez, J.; Berger, R. J.; Mul, G.; Kapteijn, F.; Moulijn, J. A. The six-flow reactor technology: A review on fast catalyst screening and kinetic studies. *Catalysis Today* **2000,** *60* (1), 93.

(57) Kumar, P.; Idem, R. A Comparative Study of Copper-Promoted Water−Gas-Shift (WGS) Catalysts. *Energy & Fuels* **2007,** *21* (2), 522.

(58) Ginés, M. J. L.; Marchi, A. J.; Apesteguía, C. R. Kinetic study of the reverse water-gas shift reaction over CuO/ZnO/Al2O3 catalysts. *Applied Catalysis A: General* **1997,** *154* (1), 155.

CHAPTER 3 DETAILED BIOMASS FAST PYROLYSIS KINETICS INTEGRATED INTO A COMPUTATIONAL FLUID DYNAMICs (CFD) AND DISCRETE ELEMENT MODELING FRAMEWORK

This chapter has been prepared as a manuscript for submission to an academic journal upon completion of the thesis.

I am the primary author on this manuscript. I was responsible for development of the computational model using existing models as a framework. I monitored the simulations throughout the run time. I analyzed and interpreted the results of the simulations and compared the results to other reports in literature. The other authors on this manuscript are Oluwafemi Oyedeji, Dr. Nourredine Abdoulmoumine, and Dr. Nicole Labbé.

Abstract

Biomass has been seen as an attractive alternative to help reduce the global dependence on petroleum fuels as it can be converted into a liquid biocrude, i.e. bio-oil, through fast pyrolysis. Fast pyrolysis is an intricate process due to the variability and anisotropy of biomass and the complicated chemistry and physics at play during conversion in a bubbling fluidized bed reactor (BFBR). The complexity of biomass fast pyrolysis lends itself well to computational fluid dynamics (CFD) and discrete element (DEM) analysis which helps to reduce experimental time and, thus, its associated cost.

This chapter investigates switchgrass fast pyrolysis simulated by computational fluid dynamics coupled with discrete element method to track individual reacting biomass particles throughout a BFBR reactor that geometrically matches an existing bench-scale unit for validation of resulting simulations. Additionally, fast pyrolysis chemistry is incorporated in this chapter through a mechanistic reaction scheme with secondary cracking reactions and this chapter assesses the impact of operational conditions on the steady state yields of liquid bio-oil, non-condensable gases (NCG), and char. Temperatures were varied from 450 to 550 °C and fluidization velocities, reported as ratio to the minimum fluidization velocity (Umf) were tested at 1.91, 3, and 4.5 Umf.

At higher fluidization velocities, biomass particle's residence time ranged between 7 and 14 s. The simulations reached steady-state after 8 s. At steady-state, the maximum bio-oil yield of 47 wt. % was achieved at 500 °C and 3 Umf and was validated at the bench-scale. Levoglucosan is the primary bio-oil component, derived from cellulose, the major constituent of switchgrass. The simulated bio-oil only contained approximately 5-9 wt. % water, which is significantly lower than seen experimentally. The predicted bio-oil yield increased to 54 wt. % when the secondary cracking reactions were turned off during the simulations suggesting that the vapor residence time is too long. Another possible explanation is the secondary cracking scheme does not adequately account for the formation of water during pyrolysis.

3.1. Introduction

As the world population continues to increase, the demand for energy also increases. Fossil fuels, the predominant current energy source, is finite and introduces greenhouse gases (GHGs), a major source of environmental concerns[1]. As a result, greater emphasis has been devoted to developing alternative, renewable energy technology to reduce the dependence on fossil fuels. In that regard, biomass is an attractive source of alternative energy due to its abundance, ubiquity and availability for year-round supply[2]. Several conversion technologies are being actively developed to transform biomass into bio-fuels, bio-energy, and bio-materials. Fast pyrolysis is one such technology and has the merit of producing a biocrude, also known as bio-oil, analogous to crude petroleum. Biomass conversion through fast pyrolysis is very complicated for several reasons. Biomass has a complex composition that differs between feedstocks, and during fast pyrolysis, biomass decomposes according to complex reaction pathways. In addition, bubbling fluidized bed reactors, commonly used in biomass fast pyrolysis, further complicate the process due to the multiphase nature that arises as a result of the interactions between the gas and solid phases inside the reactor. These complications lead to more difficult transport and hydrodynamic equations.

Currently, the common approach of determining a biomass feedstock and reactor's performance during fast pyrolysis is to carry out time and cost intensive experiments over varying operating conditions. However, this approach is ill-suited to future biorefineries which are predicted to rely on a portfolio of feedstocks with inherent variability in properties. Furthermore, often, laboratory scale experiments are not necessarily scalable directly to industrial scale systems. Thus, accurate, numerical models to simulate pyrolysis are needed to reduce the time and cost associated with experiments and generate scalable results. Until recently, most of the computational fluid dynamics (CFD) simulations of fast pyrolysis focused on specific aspects of the pyrolysis process, such as reaction kinetics, particle shrinkage, and effect of biomass composition[3,4]. More recent works aimed to incorporate all of these aspects into a comprehensive CFD model. These works adopted an Eulerian-Eulerian method, which modeled both the gas and multiple solid phases as continua[5,6]. This approach is chosen when the biomass is assumed not to be large enough to have a significant effect on the other phases (sand and gas).

This chapter is the second of a series that explores the feasibility of hydrous pyrolysis, a concept that integrates catalytic fast pyrolysis with the water-gas shift (WGS) reaction to produce additional hydrogen for hydrodeoxygenation (HDO) of vapors in one-pot. This chapter aims to develop a computational fluid dynamics model integrating a comprehensive mechanistic pyrolysis reaction scheme with a discrete element modeling (DEM) framework to simulate switchgrass fast pyrolysis. Switchgrass was chosen as the feedstock to more closely reflect the operating conditions on the experimental bench-scale system. By developing a comprehensive CFD-DEM model for fast pyrolysis, it lays the foundation for integrating the kinetics of the WGS (Chapter II) with HDO

(Chapter IV) reactions to assess the feasibility of hydrous pyrolysis. Additionally, this chapter aims to assess the effect of select operating conditions on the important outputs, e.g. yields, quality of bio-oil, and residence time distributions for the reactor. Finally, selected operating conditions were validated on a bench-scale reactor geometrically similar to the simulated reactor.

The DEM framework is synonymous with using a Lagrangian approach for modeling both the biomass and the sand particles. An Eulerian-Lagrangian approach has been used before for modeling fast pyrolysis in a fluidized bed reactor[4,7]. However, these models utilized a simple lumped kinetic scheme as opposed to the comprehensive scheme used in this chapter[8,9].

3.2. Methodology

This chapter based the simulation setup after a fast pyrolysis bench-scale bubbling fluidized bed reactor available to the investigators and located in the Center for Renewable Carbon (CRC) at the University of Tennessee. The reactor geometry used in the simulations is identical to that of the aforementioned bench-scale reactor and its details are presented in next sections. Additionally, an Eulerian-Lagrangian approach was adopted and implemented in OpenFOAM, an open-source CFD software, with the intention of public release upon validation. In this implementation, the fluid phase is modeled as a continuum by solving the Navier-Stokes equations, while the solid phase, i.e. biomass, biochar, and sand, is modeled using the discrete element method, i.e. the Lagrangian approach, characterized by Newton’s laws of motion. This approach enables tracking of each reacting and unreacting solid particle, which increases the ability to capture the physics of individual particles[10]. All of the simulations were carried out on the Joint Institute for Computational Sciences (JICS) High-Performance Computer (HPC) to significantly decrease the computational time.

The raw results from the simulations were exported and were post-processed in ParaView (Kitware Inc., Clifton Park, NY, USA) for visualization. Gas phase data at the outlet of the reactor were exported to determine the yield of the bio-oil vapors and non-condensable gases (NCG) and char yield was determined by difference. Solid biomass particle residence time analysis was performed using the statistical software R. Physical properties for both the gas and solid phases were analyzed for each simulation. Also, total product distributions for the pyrolysis process were investigated as well as the individual composition of the liquid bio-oil.

3.2.1. Simulation setup and feedstock characteristics

The simulated reactor geometry is identical in diameter, overall length as well as gas and solid entry to the bench-scale reactor proposed for validation of simulation results. Its dimensions are as follow: inner diameter of 38.1 mm (1.5 in.), height of 749.3 mm (29.5 in.) and height of biomass injection of 188 mm (7.4 in.). A schematic of the reactor geometry is shown in Figure 3.1. The biomass feedstock used in both the simulation and experimental validation is switchgrass with a moisture content of 10 wt. %, wet basis. The chemical composition of the feedstock was determined according to ASTM standards (E1768-01)[11] using the procedures for biomass carbohydrates set out by the National Renewable Energy Laboratory (NREL)[12]. Figure 3.1 lists the values input in the simulation. The biomass is reported as a mixture of cellulose, hemicellulose and lignin. The lignin is further subclassified as hydrogen-rich(LigninH), carbon-rich (LigninC), and oxygen-rich (LigninO) lignin. A biomass feeding rate of 10 g/min was used in both the simulation and experiments. This feeding rate represents a theoretical maximum feeding rate for the bench-scale reactor. Each simulation or experiment used 200 g of sand as bed material with uniform particle size of 500 μm. The envelope density of the biomass and sand is 650 and 2,650 kg/m^3, respectively. The operating conditions are at atmospheric pressure over three different

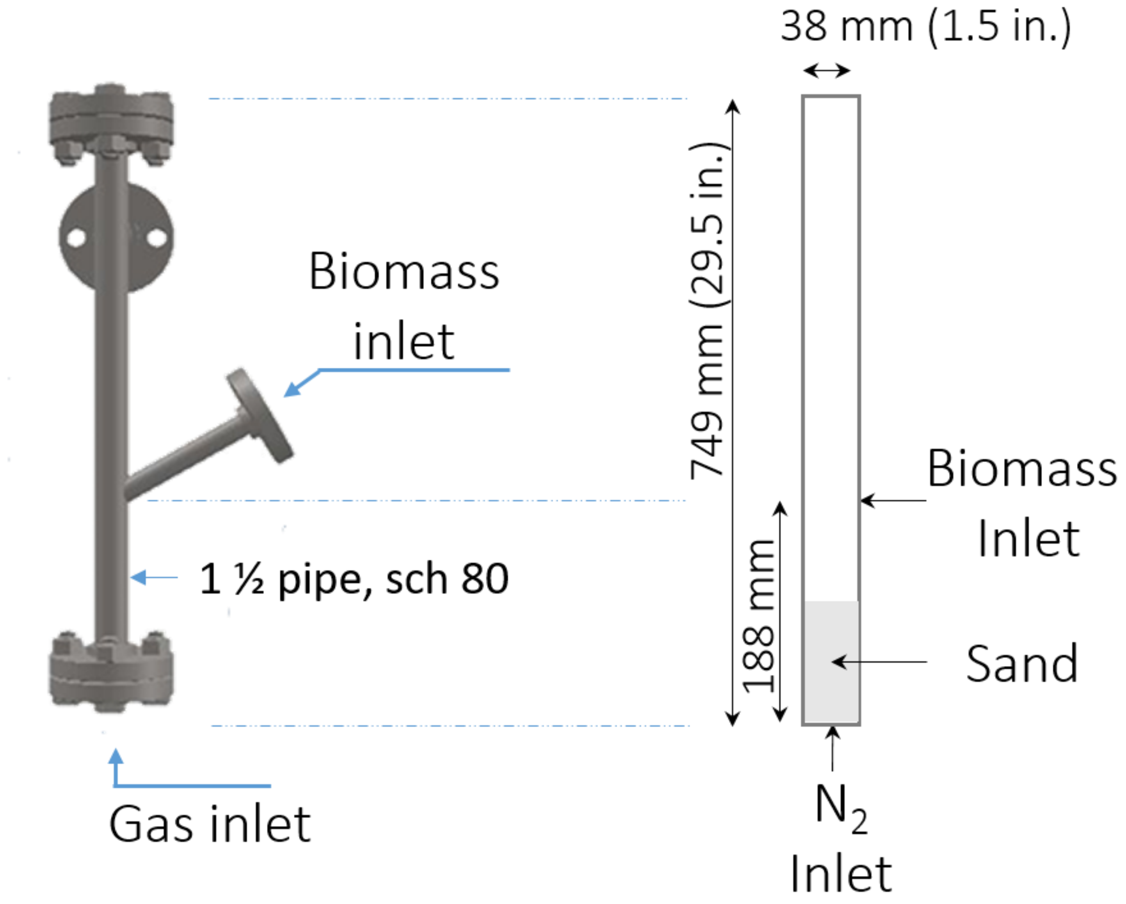

Figure 3.1. Geometry of experimental and simulation bubbling fluidized bed reactor.

Table 3.1. Biomass feedstock composition according to ASTM standard and NREL protocol on an extractive free basis.

Components	**Feedstocks (wt. %, dry basis)**
	Switchgrass
Structural components	
Cellulose	41.76 (0.6)
Hemicellulose	30.60 (0.2)
LigninC[a]	8.53 (0.0)
LigninH[a]	8.53 (0.0)
LigninO[a]	8.53 (0.0)
Proximate analysis	
Ash	2.04 (0.07)

Moisture is assumed to be 10 wt. % on a wet basis

[a] The composition of the total lignin was assumed to be equally divided between the three lignin components

temperatures: 450, 500, and 550 °C. The operating temperatures control the temperature for the walls of the reactor, the sand, and the fluidizing gas. Biomass enters the reactor at approximately room temperature (26 °C). Nitrogen serves as the inert fluidizing gas. The physical properties of biomass and sand are shown in Table 3.2. Due to the inherent complexity of biomass pyrolysis in a fluidized bed reactor, several factors have the potential ability to affect the yield of products. In addition to temperature, the fluidization velocity plays a major role when using a bubling fluidized bed reactor. Thus, for each temperature, three different fluidization velocities, reported as multipliers of the minimum fluidization velocity (Umf), (1.91, 3, and 4.5 Umf) were simulated. In total nine conditions (three temperatures and three fluidization velocities) will be simulated to assess their effect on the liquid oil yield. Secondary cracking reaction kinetics were turned off for the 3 Umf condition at each temperature to determine the effect of cracking kinetics on the overall liquid bio-oil yield. Upon completion of the simulations, the bio-oil and biochar yields are validated against the experimental results for a set of temperature and Umf.

3.2.2. Reaction scheme and kinetics

The fast pyrolysis chemistry of lignocellulosic biomass is defined using a comprehensive mechanistic reaction scheme that includes reactions involving the three main structural components of biomass, i.e. cellulose, hemicellulose, and lignin[13]. This reaction scheme is a multicomponent, multistep scheme proposed by Ranzi and colleagues[13-15]. Unlike lumped reaction schemes for biomass fast pyrolysis, it is detailed enough to enable tracking of specific evolved gas species in the vapors[16]. The detailed scheme is illustrated in Figure 3.2 and is one of the most comprehensive pyrolysis reaction mechanism available to date.[17] The reactions in the "Ranzi" scheme are assumed to proceed via a first-order Arrhenius reaction rate.

Table 3.2. Solid parameters and feeding rate for sand and biomass assumed in the simulation.

Properties	**Sand**	**Biomass**
Particle diameter (mm)	0.5	0.8
Density (kg/m^3)	2,650	650
Initial temperature (°C)	Reaction temp (450, 500, or 550)	26
Heat capacity (J/kg-K)	830	1,500
Mass	200 g (batch)	10 g/min

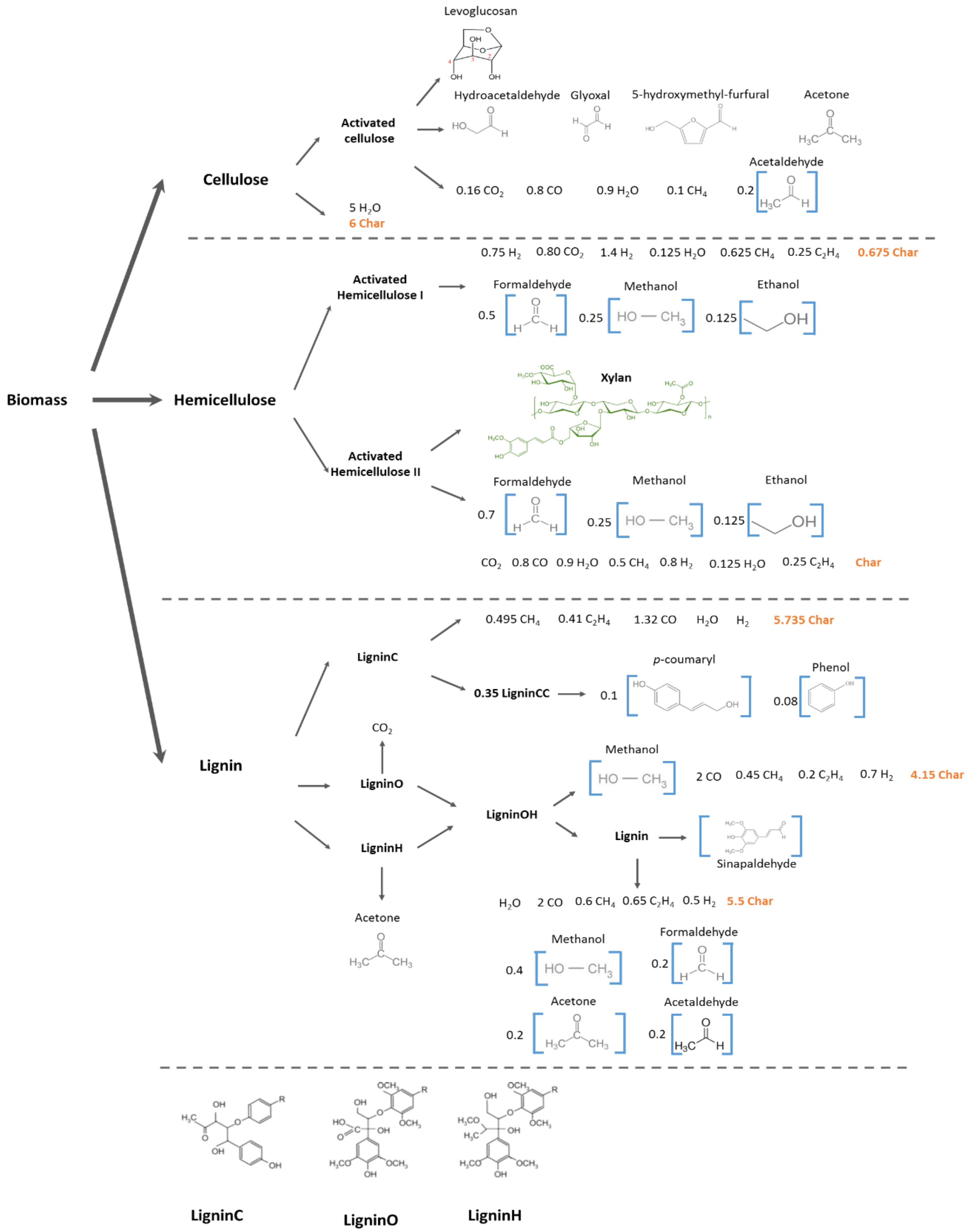

Figure 3.2. Illustration of the comprehensive pyrolysis "Ranzi" reaction scheme with stoichiometric coefficients.

In addition of the structural components, the scheme considers the biomass as a mixture of moisture and ash. However, the impact of ash on kinetics is not yet accounted in the scheme and is not evaluated in this study. Lignin is further subdivided as a combination of three reference components with different degrees of methoxylation: hydrogen (LigninH), oxygen (LigninO) and carbon (LigninC) rich lignin, respectively[18]. The reaction mechanism assumes that the initial structural components become "activated" through an initial reaction before undergoing a range of homogeneous and heterogeneous secondary pyrolysis reactions to produce the primary pyrolysis products. The reactions and the specific rate constant relationships are summarized in Table 3.3. Similarly to previous pyrolysis modeling work, this scheme does not include the gases that are thought to be produced inside the biomass particle and desorbed later but instead assumes they are immediately released to the vapor phase[5,6,17]. The larger gaseous molecules produced during the primary pyrolysis reactions further undergo secondary cracking reactions as they proceed along the length of the reactor. The longer the vapor residence time, the greater the amount of secondary reactions that take place. Secondary cracking reaction mechanisms and kinetics for select bio-oil compounds are shown in Table 3.4[19]. The reaction rates for the secondary reaction kinetics are based on a lumped kinetic model proposed by Di Blasi that assumes that bio-oil further reacts to produce gas resulting in identical pre-exponential factor and reaction rates for all cracking reaction[16,20]. The implementation of the fast pyrolysis chemistry in this study omits the water evaporation step in the kinetics of the scheme[13]. Instead, an existing built-in water evaporation model in OpenFOAM was used in this work.

Table 3.3. Primary pyrolysis reactions used in the CFD model, values from [17].

Reaction		**Reaction Rate (1/s)**	**ΔH_R^0 (J/kg)**
1	Cellulose → Activated cellulose	$4\text{x}10^{13}e^{(-188,000/RT)}$	0
2	Cellulose → 5 H_2O + 6 Char	$4\text{x}10^{7}e^{(-163,000/RT)}$	-1,913
3	Activated cellulose → Levoglucosan	$1.8Te^{(-41,800/RT)}$	364
4	Activated cellulose → 0.8 Glycolaldehyde + 0.20 Glyoxal + 0.1 Acetaldehyde +0.25 Hydroxymethyl furfural + 0.3 Acetone + 0.21 CO_2 + 0.1 H_2 + 0.4 Formaldehyde +0.16 CO + 0.83 H_2O + 0.02 Formic-acid + 0.61 Char	$5\text{x}10^{8}e^{(-121,000/RT)}$	620
5	Hemicellulose → 0.4 Activated hemicellulose I + 0.6 Activated hemicellulose II	$3.3\text{x}10^{9}e^{(-130,000/RT)}$	100
6	Activated hemicellulose I → 0.025 H_2O + 0.775 CO_2 + 0.025 Formic-acid + 0.9 CO + 0.8 Formaldehyde + 0.125 Ethanol + 0.55 Methanol + 0.25 C_2H_4 + 0.525 H_2 + 0.325 CH_4 + + 0.875 Char	$1\text{x}10^{9}e^{(-134,000/RT)}$	-92
7	Activated hemicellulose I → 0.25 H_2O + 0.75 CO_2 + 0.05 Formic-acid + 2.15 CO + 1.7 H_2 + 0.625 CH_4 + 0.375 C_2H_4 + 0.675 Char	$0.05Te^{(-33,500/RT)}$	-1,860
8	Activated hemicellulose I → Xylan	$0.9Te^{(-46,000/RT)}$	588
9	Activated hemicellulose II → 0.2 H_2O + 1.1 CO + 0.675 CO_2 + 0.5 Formaldehyde + 0.1 Ethanol + 0.2 Glycolaldehyde + 0.025 Formic-acid + 0.25 CH_4 + 0.3 Methanol + 0.275 C_2H_4 + 0.925 H_2 + Char	$3.3\text{x}10^{9}e^{(-138,000/RT)}$	212
10	LigninC→0.35 LigninCC + 0.1 Coumaryl + 0.08 Phenol + 0.41 C_2H_4 + H_2O + 0.3 Formaldehyde + 0.495 CH_4 + 1.02 CO + 0.7 H_2 + 5.735 Char	$1.33\text{x}10^{15}e^{(-203,000/RT)}$	-490
11	LigninH → LignOH + Acetone	$6.7\text{x}10^{12}e^{(-157,000/RT)}$	100
12	LigninO → LignOH + CO_2	$3.3\text{x}10^{8}e^{(-107,000/RT)}$	446
13	LigninCC → 0.3 Coumaryl + 0.2 Phenol + 0.35 Glycolaldehyde + 0.7 H_2O + 0.65 CH_4 + 0.6 C_2H_4 + 1.8 CO + H_2 + 6.75 Char	$1.6\text{x}10^{6}e^{(-132,000/RT)}$	-503
14	LigninOH → Lign + 0.9 H_2O + Methanol + 0.45 CH_4 +0.05 CO_2 + 0.2 C_2H_4 + 0.05 Formic-acid + 1.9 CO + 0.75 H_2 + 4.15 Char	$5\text{x}10^{7}e^{(-126,000/RT)}$	-120
15	LigninOH → 1.5 H_2O + 6 CO + 1.75 CH_4 + 4.4 H_2 + 0.3 C_2H_4 + 0.5 Methanol + 10.15 Char	$33e^{(-62,800/RT)}$	-1,604
16	Lign → Lumped phenol[a]	$2.4Te^{(-50,200/RT)}$	686
17	Lign→0.95 H_2O + 0.2 Formaldehyde + 0.4 Methanol + 1.95 CO + 0.6 CH_4 + 0.05 Formic-acid + 0.65 C_2H_4 + 0.5H_2 + 0.2 Acetaldehyde + 0.2 Acetone + 5.5 Char	$4\text{x}10^{8}e^{(-126,000/RT)}$	-470
18	Lign → 0.6 H_2O + 2.6 CO + 0.6 CH_4 + 0.4 Formaldehyde + 0.5 C_2H_4 + 0.4 Methanol + 2 H_2 + 6 Char	$0.083Te^{(-33,500/RT)}$	-1663

[a] Lumped phenol is a secondary pyrolysis reaction product of lignin with the molecular structure of $C_{11}H_{12}O_4$

*Activation energies are in kJ/kmol

Table 3.4. Secondary cracking reactions and kinetics of bio-oil vapors. Adapted from Blondeau and Jeanmart[19].

Reaction		Reaction Rate (1/s)
1	Hydroxymethyl furfural → 3 CO + 1.5 C_2H_4	$4.28 \times 10^6 e^{(-108/RT)}$
2	Acetone → 0.5 CO_2 + 0.5 H_2 + 1.25 C_2H_4	$4.28 \times 10^6 e^{(-108/RT)}$
3	Coumaryl → CO_2 + 2.5 C_2H_4 + 3 Char	$4.28 \times 10^6 e^{(-108/RT)}$
4	Phenol → 0.5 CO_2 + 1.5 C_2H_4 + 2.5 Char	$4.28 \times 10^6 e^{(-108/RT)}$
5	Xylan → 2 CO_2 + H_2 + 1.5 C_2H_4	$4.28 \times 10^6 e^{(-108/RT)}$
6	Levoglucosan → 2.5 CO_2 + 1.5 H_2 + 1.75 C_2H_4	$4.28 \times 10^6 e^{(-108/RT)}$
7	Glycolaldehyde → 2 CO + 2 H_2	$4.28 \times 10^6 e^{(-108/RT)}$
8	Glyoxal → 2 CO + H_2	$4.28 \times 10^6 e^{(-108/RT)}$
9	Lumped-phenol → 2 CO_2 + 3 C_2H_4 + 3 Char	$4.28 \times 10^6 e^{(-108/RT)}$

3.2.3. Governing equations

3.2.3.1. Gas phase

The gas phase is modeled using an Eulerian approach treating the gas phase as a continuum. For every time step, the governing equations must be solved for every cell in the model. The governing conservation equations of mass, momentum, energy, and chemical species are detailed below:

Mass: $$\frac{\partial}{\partial t}\left(\varepsilon_g \rho_g\right) + \nabla \cdot \left(\varepsilon_g \rho_g \boldsymbol{U}_g\right) = S_p$$

Momentum: $$\frac{\partial}{\partial t}\left(\varepsilon_g \rho_g \boldsymbol{U}_g\right) + \nabla \cdot \left(\varepsilon_g \rho_g \boldsymbol{U}_g \boldsymbol{U}_g\right) = -\nabla \mathrm{p} + \nabla \cdot \left(\varepsilon_g \boldsymbol{\tau}\right) + \varepsilon_g \rho_g \boldsymbol{g} - S_m$$

Energy: $$\frac{\partial}{\partial t}\left(\varepsilon_g \rho_g E\right) + \nabla \cdot \left(\varepsilon_g \boldsymbol{U}_g \left(\rho_g E + p\right)\right) = \nabla \cdot \left(\varepsilon_g \alpha_e \nabla h_s\right) + S_h + S_{p,h} + S_r$$

Species: $$\frac{\partial}{\partial t}\left(\varepsilon_g \rho_g Y_i\right) + \nabla \cdot \left(\varepsilon_g \rho_g \boldsymbol{U}_g Y_i\right) = \nabla \cdot \left(\varepsilon_g \rho_g D_e \nabla Y_i\right) + S_{p,Y_i} + S_{Y_i}$$

where $E = h_s - \frac{p}{\rho_g} + \frac{\boldsymbol{U}_g^2}{2}$. ε_g is the gas volume fraction, ρ_g is the density of the gas, $\boldsymbol{U}_g$ is the gas velocity, S_p is the mass source term, p is pressure, τ is the gas effective stress tensor, $\boldsymbol{g}$ is the gravitational vector, $S_m$is the momentum source term, E is the energy term, α_e is the effective dynamic thermal diffusivity, h_s is the sensible energy, S_h is the reaction enthalpy source term, $S_{p,h}$ is the particle enthalpy source term, S_r is the radiation source term, Y_i is the mass fraction of chemical species i, D_e is the mass diffusion constant, S_{p,Y_i} is the particle species source term, and S_{Y_i} is the reaction species source term. The various S terms represent specific source terms that account for the interaction between phases. The gas phase density and viscosity are determined based on the pressure and temperature values according to gas equation of state. The turbulence associated with the Eulerian phase is modeled using a k-ε turbulence model.

3.2.3.2. Discrete particle phase

Each solid particle is accounted for in the CFD-DEM simulations. The Lagrangian approach solves Newton's equations of motion for each particle at each time step. To accurately model the biomass-sand interactions, such as particle-particle and particle-wall, multiple modes must be incorporated into the framework. This also means that certain assumptions about the discrete particles must be made. The particles are assumed to be perfectly spherical, and particle shrinkage occurs through a mass-proportional shrinkage model. As the mass of the particle, m_p, shrinks due to pyrolysis reactions, the diameter of the particle, d_p, shrinks proportionally.

$$d_p = \left(\frac{6m_p}{\pi\rho_p}\right)^{0.333}$$

For simulations where inter-particle (Van der Waals, electrostactic) forces are negligible, the dominant forces affecting the Lagrangian phase include the contact forces from interactions (particle-particle and particle-wall) and the drag force[21]. The relevant models used to calculate these forces are discussed below.

3.2.3.2.1. Contact force

The boundary conditions for the reactor were set to a no-slip condition on the reactor walls. Therefore, the contact forces present between the particles and the walls of the reactor are calculated using a no-slip, elastic contact model. The particle contact model is also responsible for solving the behavior of particle-particle interactions. The Hertz-Mindlin is a Hertzian variation of the linear spring-dashpot model that deals with particles of a spherical shape. Hertz's theory applies to contact in the normal direction while Mindlin and Deresiewicz accounted for the tangential direction[22,23]. The total contact force acting on each particle is equal to the sum of the normal force, F_n, and the tangential force, F_t, applied to the particle.

$$F_{contact} = F_n + F_t$$

3.2.3.2.2. Drag force

The Gidaspow drag model was chosed to account for the interphase momentum between the gas and solid phases. The Gidaspow model combines the existing Wen and Yu drag models with the Ergun equation[24]. The Wen and Yu model uses a correlation based on data from Richardson and Zaki and is valid when the viscous forces dictate the flow behavior[25,26]. The momentum exchange coefficient, β, is modeled as proposed by Gidaspow using the following equations

$$\beta = \begin{cases} 150\frac{\varepsilon_p^2 \mu_g}{\varepsilon_g^2 d_p^2} + 1.75\frac{\varepsilon_p \rho_g}{\varepsilon_g d_p}\left|\boldsymbol{U}_g - \boldsymbol{U}_p\right|, & \varepsilon_g < 0.8 \\ 0.75 C_d \frac{\varepsilon_p \rho_g}{d_p}\left|\boldsymbol{U}_g - \boldsymbol{U}_p\right| \varepsilon_g^{-2.65}, & \varepsilon_g \geq 0.8 \end{cases}$$

where β is the momentum exchange coefficient, ε_p is the solid volume fraction, $\boldsymbol{U}_p$ is the velocity of the particle, and C_d is the drag coefficient.

The momentum exchange coefficient represents the drag force between the phases and is incorporated into the momentum equation as a source term, S_m [27]. The Ergun equation is used for the momentum exchange coefficient when the gas volume fraction is less than 0.8. Any other value requires the use of the Wen and Yu model equation. The drag coefficient is dependent upon the Reynolds number (Re_p).

$$C_d = \begin{cases} \frac{24}{Re_p}\left(1 + 0.15 Re_p^{0.687}\right), & Re_p < 1{,}000 \\ 0.44, & Re_p \geq 1{,}000 \end{cases}$$

$$Re_p = \frac{\varepsilon_g \rho_g d_p \left|\boldsymbol{U}_g - \boldsymbol{U}_p\right|}{\mu_g}$$

3.2.3.2.3. Heat transfer

The heat transfer between the Eulerian and Lagrangian phase is solved by using the Ranz Marshall submodel that makes use of the Nusselt number (Nu_p).

$$h = \frac{6 \propto_p k_g Nu_p}{d_p^2}$$

$$Pr = \frac{C_{pg}\mu_g}{k_g}$$

$$Nu_p = 2 + 0.6Re_p^{0.5}Pr^{0.33}$$

The heat transfer constant (h) is determined from the particle volume fraction ($\propto_p$), thermal conductivity (k_g), the Nusselt number, and the particle diameter. The Nusselt number is calculated from both the Reynolds number and the Prandtl number (Pr), which depends on the gas heat capacity (C_{pg}), the gas phase viscosity, and the thermal conductivity.

3.2.4. Computational conditions and assumptions

The model geometry simulates a cross-sectional portion of the reactor. The geometry mesh in OpenFOAM consists of 3,322 points, 6,160 faces, and 1,500 cells. The maximum cell volume is 1.94×10^{-8} m^3 (19.4 mm^3). The geometry is set up as a quasi-3D simulation and the mesh is designed with the reactor specification in the x and y-directions with a minimal depth in the z-direction, which corresponds to 1/30th of the total reactor volume. The mesh uses a symmetry condition to mirror the reaction as if the mesh was a 3D cylinder. Boundary conditions are set on the reactor walls, the gas inlet and outlet, and the biomass inlet. The reactor walls are set to a no-slip velocity condition with a fixed value reaction temperature with zero gradient pressure and composition conditions. The gas outlet of the reactor maintains a fixed value pressure of 101,325

Pa with a zero gradient for the other conditions. The gas inlet at the bottom of the reactor has fixed values for velocity, temperature, and composition conditions. The gas inlet velocity depends on the Umf ratio for the simulation, the temperature is set to reaction temperature, and the gas composition contains 100% nitrogen. The biomass inlet has a zero gradient for each condition. All of the boundary conditions are listed in Table 3.5.

The time step for each simulation is to $1\text{x}10^{-5}$ s with a maximum residual tolerance of $1\text{x}10^{-5}$ for each chemical species and physical parameter and a maximum Courant number of one. The Courant number is a measure of how much information passes through a computational grid cell in a given time step. A Courant number greater than one signifies that information is propagating through multiple cells in one time step, which will cause the model to fail. Each simulation was carried out for a run time of 20 s. The geometry and fields are divided into 15 subdomains equidistant in the x-direction. The simulations are then carried out in parallel mode with one processor for each subdomain.

3.3. Results and discussion

The simulations show that biomass devolitilization begins to occur at temperatures lower than the specified operating temperatures. The first few seconds of the simulations mainly involved heating the biomass particles to the devolitilization temperature. After the initial devolitilization temperature was achieved, pyrolysis began while the biomass particles continued to heat up to reaction temperatures. The simulations began to reach steady-state at approximately eight seconds. All of the results presented from this point on will be after steady-state has been achieved.

Table 3.5. Simulation boundary conditions

Boundary	**Velocity**	**Temperature**	**Pressure**	**Gas Volume Fraction**	**Chemical Species**
Gas Inlet	Fixed value	Fixed value	Zero gradient	Fixed value	Fixed value
Walls	No slip	Fixed value	Zero gradient	Zero gradient	Zero gradient
Biomass Inlet	Zero gradient	Zero gradient	Zero gradient	Zero gradient	Zero gradient
Gas Outlet	Zero gradient	Zero gradient	Fixed value	Zero gradient	Zero gradient

3.3.1. Temperature, velocity, and void fraction

Biomass particles entered the reactor at room temperature (26 °C) at a mass flow rate of 10 g/min. A temperature profile of particles is shown in Figure 3.3. The temperature profile in the gas phase is uniform throughout the majority of the sand bed as well as near the reactor walls. This is due to the walls, sand particles, and the fluidization gas all being equated to the reaction temperature. The temperature of the gas phase begins to vary at the biomass inlet. This is due to the biomass entering at room temperature (300 K) and devolitilization beginning before the set reaction temperature. The vapor phase continued to heat up as they travel along the length of the reactor. As the biomass particles interacted with the sand, the particles heated up due to particle-particle conduction and convective heat transfer and began to react. The biomass pyrolysis reactions started once the devolitilization temperature, which was set to 126 °C (400 K), was acheived. This temperature allowed for drying to occur before any biomass decomposition started. Once the reactions started, biomass particles retained in the reactor until their size was reduced enough to be elutriated, or removed. As evidenced in Figure 3.3, the biomass particles approached the set reaction temperature prior to elutration indicating that the particle residence time was sufficient to allow heating to the desired reaction temperature.

The velocity of the gas phase was streamlined throughout the length of the reactor (Figure 3.4). Nitrogen was fed into the bottom of the reactor at rates between 0.5 and 1.8 m/s, which corresponds to 1.91 and 4.5 Umf, respectively. These values are slightly higher than reported fluidization velocities in other CFD works[5,6]. In the activated region where the void volume fraction was less than 0.5, the gas velocity increased and fluctuated as it passed through the dense solid region before returning to a steady flow rate (Figure 3.5).

The void fraction of the solid phase in the activated bed region for each simulation,

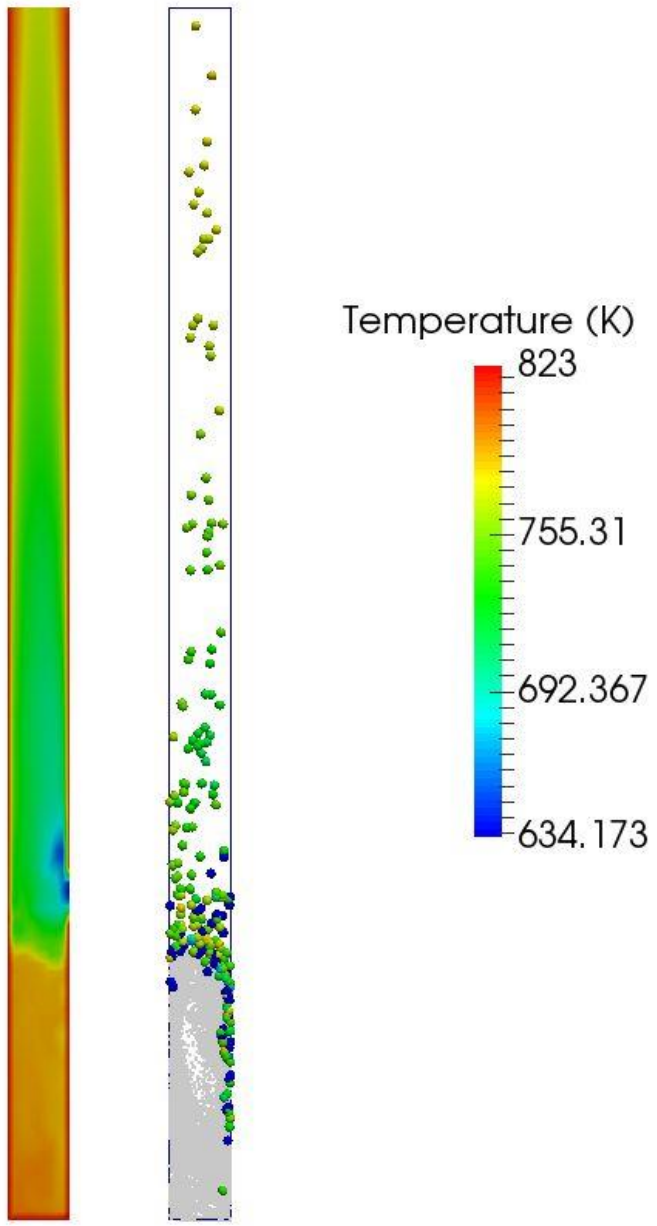

Figure 3.3. Temperature profile for the gas phase (left) and biomass (right) for 550 °C at 4.5 Umf at 18s.

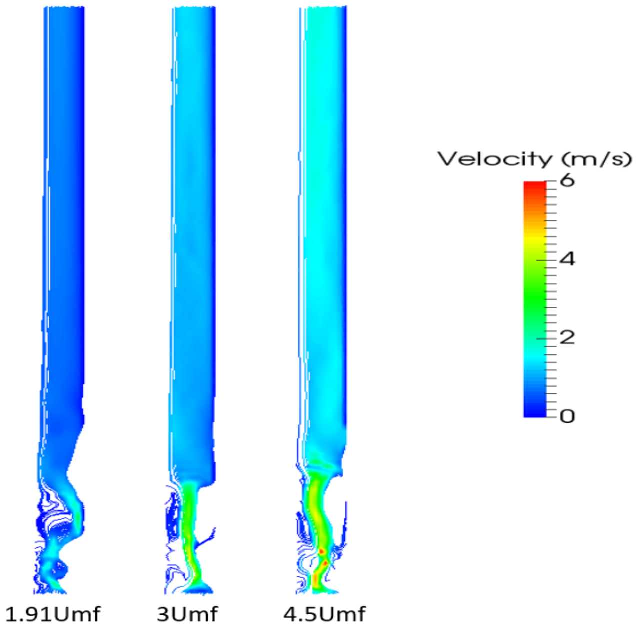

Figure 3.4. Gas velocity streamlines for each fluidization condition at 550 °C.

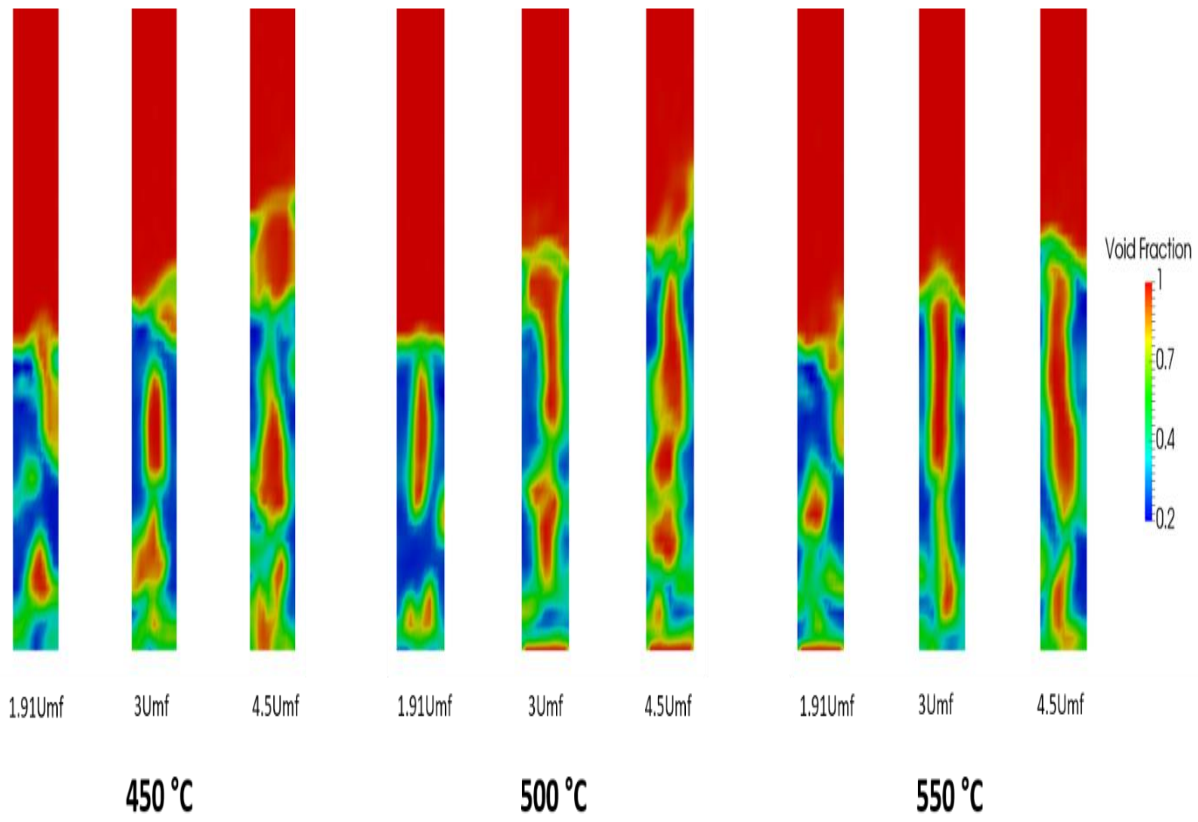

Figure 3.5. Void fraction in the activated bed region (bottom fraction of reactor).

presented in Figure 3.5, shows the difference in fluidization at the different velocities. The 1.91 Umf fluidization condition maintained a very dense solid region with a void fraction of less than 0.5, which does not provide adequate mixing for proper operation of a fluidized bed reactor. The red areas in the activated regions identified where the fluidization bubbles occur in the sand bed. This visualization confirms the simulations are operating in the bubbling regime. The fluidization behavior is in agreement with other CFD simulations[28]. One element to take note of is the mixing interaction between the sand and biomass particles. Despite significant fluidization, the majority of the biomass particles were retained on the top of the sand bed forming a layer of biomass particles. This can possibly be attributed to the stark density difference between the biomass and sand particles. Also, the activated bed height may not be reaching the biomass; therefore, when the biomass enters the system it is not immediately caught in the sand bed, but instead lands on top of the bed. The biomass particles mixed further into the sand bed on the sides of the reactor. As the fluidization velocity is increased, the size of the bubbles formed in the bed are larger and longer (4.5Umf). This may be an indication the simulation is approaching the slugging regime, which is not ideal for FBRS[29].

3.3.2. Solid particle residence time

One of the main characteristics of biomass fast pyrolysis is a short vapor residence time (< 2 s). Another important parameter, yet less investigated, is the solid biomass particle residence time. After the biomass has sufficiently undergone pyrolysis, the remaining char particles are elutriated, or removed, from the reactor. The solid particle residence time is an important aspect of pyrolysis and must be balanced to optimize the process. If the particles never elutriate, char will accumulate inside the reactor and significantly lower the efficiency of the fluidized bed reactor. On the other hand, if the fluidization velocity is large enough to quickly elutriate the particles, raw biomass will leave the reactor and will result in a loss of yield. At fluidization velocities greater than 3Umf, elutriation of the biomass began to occur as the particles underwent pyrolysis and lost mass. Solid particle residence time distributions (RTD) for multiple conditions are shown in Figure 3.6. Higher temperatures played a large role in the length of time each biomass particle stayed inside the reactor. An increase of temperature increased the rate of pyrolysis to vaporize the solid biomass, which led to faster elutriation. The 550 °C and 4.5 Umf case provided the shortest average particle residence time of approximately 7.5 s. Upon, decreasing temperature to 500 and 450 °C, the average RTD was increased to 12 s and 14 s, respectively.

3.3.3. Pyrolysis yields and composition

The distribution of the pyrolysis products is shown in Figure 3.7. The maximum bio-oil produced, including water, was simulated to be 47%. The 500 °C-3 Umf and 550 °C-4.5 Umf conditions provided the maximum bio-oil yields. The bio-oil yield is mainly affected by two parameters, temperature and velocity, or vapor residence time. Increased temperatures increase the rate of the pyrolysis reactions, which also increase the rate of cracking reactions that decrease the bio-oil yield. The gas velocity limits the residence time the reactions have to take place. Therefore, the temperature and velocity must be balanced to find the optimal operating conditions and maximize the bio-oil yield. The higher temperature conditions correlate to an increase in the non-condensable gas (NCG) yield and a decrease in char yield. The overall bio-oil yields, organic and aqueous, are lower than values typically reported from fast pyrolysis.[6,30]

For initial validation, experimental testing on the bench-scale reactor for the 450 °C and 3Umf conditions produced a maximum bio-oil yield of slightly less than 50%, which is comparable to the yields predicted in our simulations. Despite the fact the total bio-oil yields were similar, the composition is significantly different.

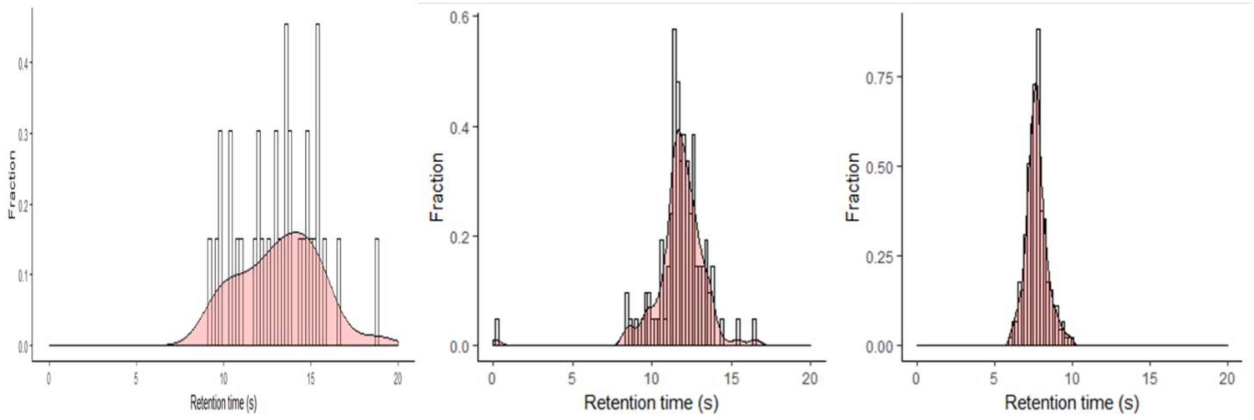

Figure 3.6. Residence time distributions (RTD) with histograms for the 4.5Umf condition at 450 (left), 500 (middle), and 550°C (right).

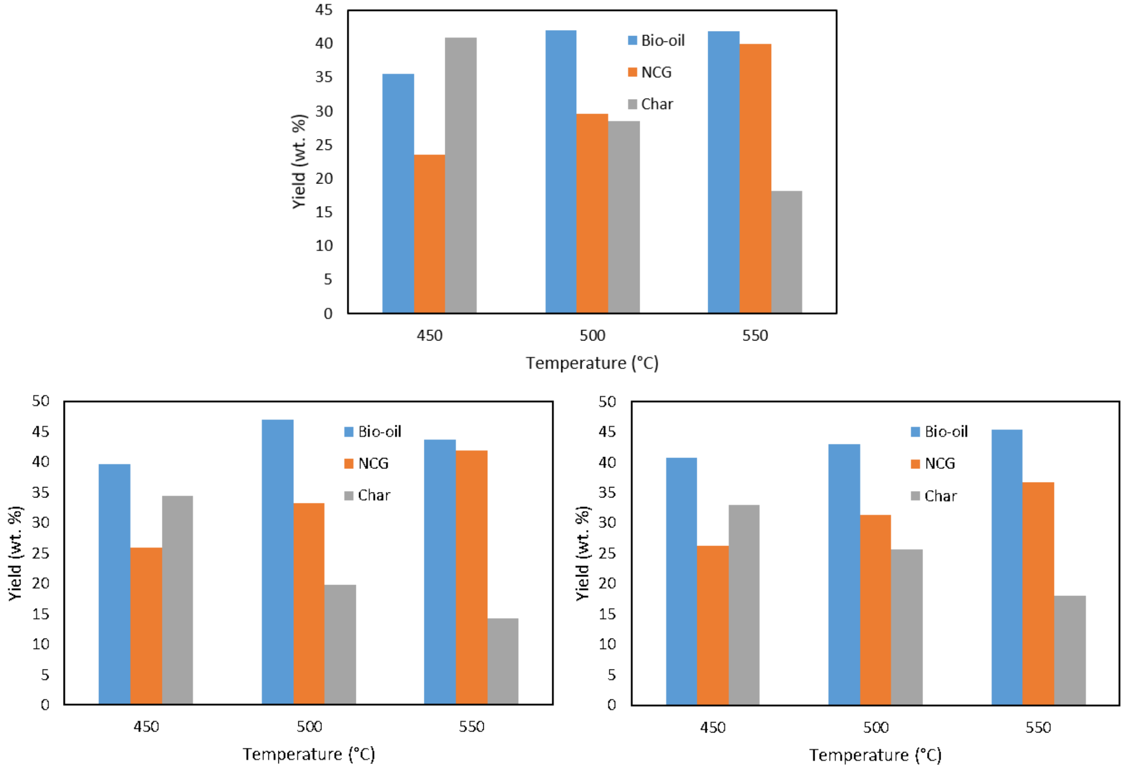

Figure 3.7. Simulated fast pyrolysis yields of bio-oil, non-condensable gases (NCG) and char for 1.91Umf (top), 3Umf (left), and 4.5Umf (right) at 450, 500, and550 °C.

In our simulations, there is significantly less water produced than expected. The simulated bio-oil produced has a water content (wt. %) of less than 7% compared to 20-30% observed experimentally, both on our bench-scale and in previous experimental work[31]. The original pyrolysis scheme includes a reaction step for liquid water to be converted into water vapor; however, this work made use of an existing water evaporation model built-in to OpenFOAM. This could be one of the reasons as to why the water content differs from other work done using this scheme. As mentioned in earlier studies, the secondary reaction scheme for each bio-oil species was based on a lumped pyrolysis model with kinetic parameters for each cracking reaction being the same[19,20,32].

The simulation results were further probed in this section to assess the impact of operating conditions of the oil quality and contrast the simulation findings with other works. The comparison between simulations and validation is possible because the fast pyrolysis reaction scheme allows for the determination of specific "model" components and their respective concentration in the bio-oil. The steady state breakdown of the bio-oil components for the 550 °C simulations is shown in Figure 3.8. The main component for each condition is levoglucosan with a weight percent between 39 and 50 wt. %. This large amount of levoglucosan can be somewhat expected since levoglucosan is the main bio-oil product from the cellulose branch of reactions in the scheme. This, coupled with the fact that cellulose is the largest component in switchgrass and levoglucosan has a higher density than other bio-oil components, lends to the bio-oil having a large fraction of levoglucosan. Reported experimental results differ with simulations and show levoglucosan yields ranging from 5 to 33 wt. % of the bio-oil[33-35]. The reason for this discrepancy is most likely due to the limitations of the kinetic scheme. While the comprehensive scheme is one of the most detailed

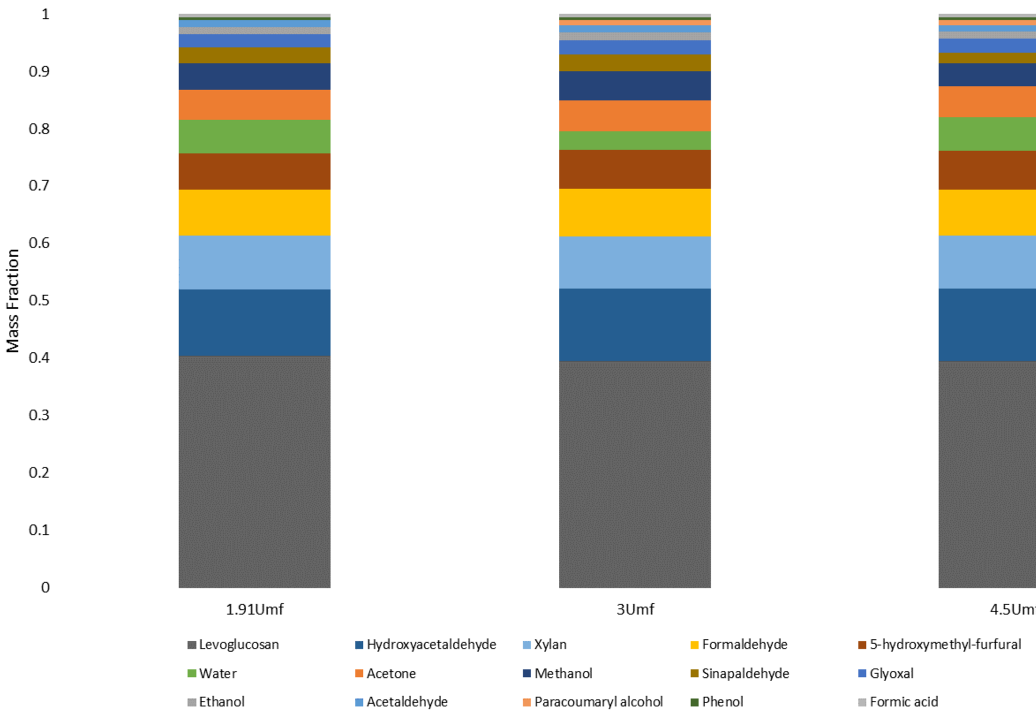

Figure 3.8. Steady-state bio-oil product composition at 550 °C.

schemes to date, it still utilizes the main “model” bio-oil compounds and does not fully capture the hundreds of bio-oil compounds that are observed experimentally. The simulated findings in this study on the yield of levoglucosan are larger than those reported by others where levoglucosan yields range from 22 to 40 wt. %[6,36]. The cellulose content used in this simulation is slightly higher than in other CFD models using the same pyrolysis scheme. Levoglucosan is a highly oxygenated compound which would necessitate downstream deoxygenation. The fluidization velocity does not appear to have a significant effect on the levoglucosan content of the bio-oil. This can be attributed to secondary cracking reactions all having the same kinetics; therefore, all reactions has the same reaction rate constant at each operating condition. As reaction temperature is increased, the levoglucosan content decreased. This trend can most likely be attributed to the rate of product formation in the primary pyrolysis kinetics and not the cracking reactions.

Simulated product yields predicted considerably more NCGs (25-40 wt. %) than is typically reported for biomass fast pyrolysis[5,6,37]. Simulations were carried out at 550 °C and 3Umf without the secondary cracking reactions and the bio-oil yield increased by approximately 10 wt. %. Apart from the overall bio-oil yield, the lack of secondary reactions had no real effect on the moisture content of the bio-oil. Previous work has shown that water is produced primarily from the secondary cracking reactions[38,39]. Therefore, the secondary cracking reactions in the simulations are not accounting for adequate water formation. Further work needs to be conducted to account for more water production in the kinetic scheme as well as a more robust experimental validation for the hydrodynamics and product yields of the simulations.

3.4. Conclusions

The present study outlines the findings of a computational fluid dynamics and discrete element modeling study of switchgrass fast pyrolysis in a bubbling fluidized bed reactor. The model included a detailed fast pyrolysis reaction scheme and its associated kinetics. The simulations produced results comparable to yields observed experimentally on an identical bench-scale system. The main difference between the simulation, the experimental results and previous work is the moisture content of bio-oil, which was 20-25 wt. % less than previous CFD studies and experimental work. Levoglucosan was the primary component of the predicted bio-oil ranging between 39 and 50 wt. %. At higher temperatures and higher fluidization velocities, solid biomass particles began to elutriate from the reactor. Lower temperatures resulted in high residence time and, as the temperature was reduced from 550 to 450 °C, the biomass particle RTD increased from 7.5 to 14 s, respectively. The secondary reactions have a significant effect on the bio-oil yield at 550 °C and 3Umf leading to a 10 wt. % increase in yield. The bio-oil is almost entirely made up on the organic fraction with a small moisture content. Future work needs to be done to investigate the discrepancy between the amount of water of the simulation and experimental pyrolysis tests.

List of references

(1) Cheng, J. *Biomass to Renewable Energy Processes, Second Edition*; CRC Press, 2017.

(2) Tidball, R. B., J. ; Rodriguez, N.; Knoke, S. . Cost and Performance Assumptions for Modeling Electricity Generation Technologies. **2010**.

(3) Dupont, C.; Chen, L.; Cances, J.; Commandre, J.-M.; Cuoci, A.; Pierucci, S.; Ranzi, E. Biomass pyrolysis: Kinetic modelling and experimental validation under high temperature and flash heating rate conditions. *Journal of Analytical and Applied Pyrolysis* **2009,** *85* (1), 260.

(4) Papadikis, K.; Gu, S.; Bridgwater, A. V. CFD modelling of the fast pyrolysis of biomass in fluidised bed reactors: Modelling the impact of biomass shrinkage. *Chemical Engineering Journal* **2009,** *149* (1), 417.

(5) Ranganathan, P.; Gu, S. Computational fluid dynamics modelling of biomass fast pyrolysis in fluidised bed reactors, focusing different kinetic schemes. *Bioresource Technology* **2016,** *213*, 333.

(6) Mellin, P.; Kantarelis, E.; Yang, W. Computational fluid dynamics modeling of biomass fast pyrolysis in a fluidized bed reactor, using a comprehensive chemistry scheme. *Fuel* **2014,** *117, Part A*, 704.

(7) Sharma, A.; Wang, S.; Pareek, V.; Yang, H.; Zhang, D. Multi-fluid reactive modeling of fluidized bed pyrolysis process. *Chemical Engineering Science* **2015,** *123*, 311.

(8) Bradbury, A. G. W.; Sakai, Y.; Shafizadeh, F. A kinetic model for pyrolysis of cellulose. *Journal of Applied Polymer Science* **1979,** *23* (11), 3271.

(9) Di Blasi, C. Analysis of Convection and Secondary Reaction Effects Within Porous Solid Fuels Undergoing Pyrolysis. *Combustion Science and Technology* **1993,** *90* (5-6), 315.

(10) Zhu, H. P.; Zhou, Z. Y.; Yang, R. Y.; Yu, A. B. Discrete particle simulation of particulate systems: Theoretical developments. *Chemical Engineering Science* **2007,** *62* (13), 3378.

(11) ASTM, 2015; Vol. E1758-01.

(12) Sluiter, A.; Hames, B.; Ruiz, R.; Scarlata, C.; Sluiter, J.; Templeton, D.; Crocker, D. Determination of structural carbohydrates and lignin in biomass. *Laboratory analytical procedure* **2008,** *1617*, 1.

(13) Corbetta, M. P., S.; Ranzi, E.; Bennadji, H.; Fisher, E. M. XXXVI Meeting of the Italian Section of the Combustion Institute, 2013.

(14) Ranzi, E.; Cuoci, A.; Faravelli, T.; Frassoldati, A.; Migliavacca, G.; Pierucci, S.; Sommariva, S. Chemical kinetics of biomass pyrolysis. *Energy & Fuels* **2008,** *22* (6), 4292.

(15) Ranzi, E.; Debiagi, P. E. A.; Frassoldati, A. Mathematical Modeling of Fast Biomass Pyrolysis and Bio-Oil Formation. Note I: Kinetic Mechanism of Biomass Pyrolysis. *ACS Sustainable Chemistry & Engineering* **2017,** *5* (4), 2867.

(16) Di Blasi, C.; Russo, G. In *Advances in Thermochemical Biomass Conversion*; Bridgwater, A. V., Ed.; Springer Netherlands: Dordrecht, 1993, DOI:10.1007/978-94-011-1336-6_70 10.1007/978-94-011-1336-6_70.

(17) Humbird, D.; Trendewicz, A.; Braun, R.; Dutta, A. One-Dimensional Biomass Fast Pyrolysis Model with Reaction Kinetics Integrated in an Aspen Plus Biorefinery Process Model. *ACS Sustainable Chemistry & Engineering* **2017,** *5* (3), 2463.

(18) Faravelli, T.; Frassoldati, A.; Migliavacca, G.; Ranzi, E. Detailed kinetic modeling of the thermal degradation of lignins. *Biomass and Bioenergy* **2010,** *34* (3), 290.

(19) Blondeau, J.; Jeanmart, H. Biomass pyrolysis at high temperatures: Prediction of gaseous species yields from an anisotropic particle. *Biomass and Bioenergy* **2012,** *41*, 107.

(20) Park, W. C.; Atreya, A.; Baum, H. R. Experimental and theoretical investigation of heat and mass transfer processes during wood pyrolysis. *Combustion and Flame* **2010,** *157* (3), 481.

(21) Di Renzo, A.; Di Maio, F. P. Comparison of contact-force models for the simulation of collisions in DEM-based granular flow codes. *Chemical Engineering Science* **2004,** *59* (3), 525.

(22) Hertz, H. Uber die Beruhrung fester elastischer Korper (On the contact of elastic solids). *Journal fur die reine und angewandte Mathematik* **1882,** *92*, 156.

(23) Mindlin, R. D. D., H. Elastic spheres in contact under varying oblique forces. *Journal of Applied Mechanics* **1953,** *20*, 327.

(24) Gidaspow, D. *Multiphase Flow and Fluidization: Continuum and Kinetic Theory Descriptions*; Academic Press, 1994.

(25) Lundberg, J. H., B.M. Proc. 49th Scand. Conf. Simulation and Modeling, Oslo, Norway, 2008.

(26) Richardson, J. F. Z., W. N. Sedimentation and fluidization: Part I. *Transactions of the American Institute of Chemical Engineers* **1954,** *32*, 35.

(27) Benzarti, S.; Mhiri, H.; Bournot, H. Drag models for simulation gas–solid flow in the bubbling fluidized bed of FCC particles. *World Academy of Science, Engineering and Technology* **2012,** *61*, 1138.

(28) Papadikis, K.; Gu, S.; Fivga, A.; Bridgwater, A. V. Numerical Comparison of the Drag Models of Granular Flows Applied to the Fast Pyrolysis of Biomass. *Energy & Fuels* **2010,** *24* (3), 2133.

(29) Ramirez, E.; Finney, C. E. A.; Pannala, S.; Daw, C. S.; Halow, J.; Xiong, Q. Computational study of the bubbling-to-slugging transition in a laboratory-scale fluidized bed. *Chemical Engineering Journal* **2017,** *308*, 544.

(30) Kan, T.; Strezov, V.; Evans, T. J. Lignocellulosic biomass pyrolysis: A review of product properties and effects of pyrolysis parameters. *Renewable and Sustainable Energy Reviews* **2016,** *57*, 1126.

(31) Bridgwater, A. V.; Meier, D.; Radlein, D. An overview of fast pyrolysis of biomass. *Organic Geochemistry* **1999,** *30* (12), 1479.

(32) Miller, R. S.; Bellan, J. A Generalized Biomass Pyrolysis Model Based on Superimposed Cellulose, Hemicelluloseand Liqnin Kinetics. *Combustion Science and Technology* **1997,** *126* (1-6), 97.

(33) Mullen, C. A.; Boateng, A. A. Chemical Composition of Bio-oils Produced by Fast Pyrolysis of Two Energy Crops. *Energy & Fuels* **2008,** *22* (3), 2104.

(34) Bennett, N. M.; Helle, S. S.; Duff, S. J. B. Extraction and hydrolysis of levoglucosan from pyrolysis oil. *Bioresource Technology* **2009,** *100* (23), 6059.

(35) Li, L. I. N.; Zhang, H. Preparing Levoglucosan Derived from Waste Material by Pyrolysis. *Energy Sources* **2004,** *26* (11), 1053.

(36) Mellin, P.; Kantarelis, E.; Zhou, C.; Yang, W. Simulation of Bed Dynamics and Primary Products from Fast Pyrolysis of Biomass: Steam Compared to Nitrogen as a Fluidizing Agent. *Industrial & Engineering Chemistry Research* **2014,** *53* (30), 12129.

(37) Trendewicz, A.; Braun, R.; Dutta, A.; Ziegler, J. One dimensional steady-state circulating fluidized-bed reactor model for biomass fast pyrolysis. *Fuel* **2014,** *133*, 253.

(38) Morf, P.; Hasler, P.; Nussbaumer, T. Mechanisms and kinetics of homogeneous secondary reactions of tar from continuous pyrolysis of wood chips. *Fuel* **2002,** *81* (7), 843.

(39) Zhang, X.; Yang, W.; Blasiak, W. Thermal decomposition mechanism of levoglucosan during cellulose pyrolysis. *Journal of Analytical and Applied Pyrolysis* **2012,** *96*, 110.

CHAPTER 4 COMPUTATIONALLY MODELING BIOMASS HYDROUS PYROLYSIS USING IN-SITU HYDROGEN GENERATION

This chapter has been prepared as a manuscript for submission to an academic journal upon completion of the thesis.

I am the primary author on this work. My responsibilities included finding existing kinetics reported for hydrodeoxygenation in literature. I also modified the simulation from Chapter 3 to simulate hydrous pyrolysis. I combined the reported kinetics as well as the determined kinetics from Chapter 2 into the new simulation. The other authors on this manuscript are Oluwafemi Oyedeji, Dr. Nourredine Abdoulmoumine, and Dr. Nicole Labbé.

Abstract

A computation fluid dynamics (CFD) model was developed with the intention of modeling biomass hydrous pyrolysis to produce refinery-ready bio-crude oil. The hydrous pyrolysis process replaces nitrogen with steam as the fluidizing gas to facilitate *in-situ* hydrogen generation to fulfill the hydrogen requirement of hydrous pyrolysis. This chapter combines experimentally derived water-gas shift kinetics from Chapter 2 with a CFD model of conventional biomass fast pyrolysis from Chapter 3. Hydrous pyrolysis simulations were carried out from 300 to 500 °C at 30 bar using a comprehensive pyrolysis scheme coupled with a global, lumped HDO kinetic scheme. Individual bio-oil components from pyrolysis were summed together in one lumped "Oil" component. The HDO scheme deoxygenizes the "Oil" component to produce either a heavy or light fraction of deoxygenated bio-oil. Simulations have proceeded for approximately sevon seconds of simulation time. The change in operating conditions increased the temperature uniformity in the reactor as well as increased the speed of particle elutriation. The simulations have not reached steady-state, therefore we are unable to conclude on the final product yields. But, the selectivity of the HDO kinetics appears to significantly favor production of the heavy oil fraction.

4.1. Introduction

Conventional fast pyrolysis is one of the few technologies that give us the opportunity to engineer in minutes what takes millions of years in nature – thermolytic (~400-600 ˚C) conversion of biological materials into an energy dense biocrude oil. This bio-based crude oil is commonly referred to as bio-oil and is regarded as a potential replacement for crude petroleum in refineries. In general, when bio-oil is produced through conventional fast pyrolysis, it contains high oxygen content (~40-50 wt. %), is immiscible with conventional hydrocarbon fuels, and has high acidity (pH 2–3 and total acid number (TAN) of 100–200)[1.] In contrast, crude petroleum oil contains less than 1 wt. % oxygen[2,3]. Indeed, while crude petroleum oils are composed mainly of hydrocarbons, bio-oils are primarily composed of oxygenates with reactive functional groups such as carboxylic acid, aldehydes, and ketones leading to polymerization reactions, which increases the viscosity over time.[2,4,5] The presence and higher proportion of these reactive compounds in bio-oils result in poor stability and lower temperatures (~ -20°C) are required to prevent these polymerization reactions.[6] Additionally, the high TAN limits the ability to process bio-oil in existing petrochemical refining infrastructures which require TANs less than 2 to avoid corrosion to construction materials used in transport vessels and refinery conversion equipment[1]. All of the aforementioned shortcomings effectively make bio-oil a low-value feedstock with little demand [7].

Over the past decades, there has been a concerted research effort aimed at improving bio-oil's chemical and physical properties. In particular, catalytic fast pyrolysis in the presence of a catalyst, usually zeolite catalysts, has been extensively investigated with the goal of producing hydrocarbons from biomass.[4,8-10] Through dehydration, decarboxylation, and decarbonylation reactions, catalytic fast pyrolysis vapors are partially stripped of their oxygen through release of water, carbon dioxide or carbon monoxide. Catalytic fast pyrolysis has been able to produce stabilized bio-oil.[11] However, significant challenges remain. The oxygen content is reduced but it still remains high around 20 wt. %.[4] Furthermore, at best, only 20–30% of the carbon in the biomass ends up in the liquid product and approximately 30% of the carbon forms into coke, causing catalyst deactivation.[10] After decades of intense catalytic fast pyrolysis research, it has become evident that lignocellulosic biomass's low hydrogen density cannot sustain bio-oil deoxygenation without additional hydrogen input. Bio-oil can be upgraded to have a lower oxygen content through hydrotreating. Hydrotreating of bio-oil involves re-evaporating and reacting bio-oil vapors with hydrogen gas over sulfide cobalt or nickel molybdenum catalysts (sulfide CoMo and NiMo, respectively) at very high pressures (100–170 bar), 310–375 °C [12], and low space velocities (0.1–0.2 LHSV) [13,14] . However, this approach has significant drawbacks: including i) low liquid yield (26–30 wt. % of the biomass)[1,15], and ii) formation of large quantities of coke, leading to rapid catalyst deactivation and reactor clogging [12] and a slow and overall expensive process. The shortcomings of catalytic fast pyrolysis and hydrotreating motivate exploration of biomass pyrolytic decomposition under hydrogen environments, an idea initially successfully tested for coal[16-18]. Biomass pyrolysis approaches under hydrogen environments have been labeled hydropyrolysis [1,7,19] or reactive catalytic pyrolysis, depending on the process hydrogen pressure requirement[20]. In these approaches, the reducing hydrogen gas is speculated to generate hydrogen radicals which react with pyrolysis volatiles, commonly in the presence of a catalyst, to remove oxygen, released in the form of water (H_2O), carbon monoxide (CO), and carbon dioxide (CO_2), and while yielding hydrocarbons. It is also speculated that many of the reactive pyrolysis volatile intermediates, which would otherwise undergo polymerization, leading to bio-oil instability as well as yield reduction and catalyst coking, are quenched by the hydrogen radicals[14,21]. Fast pyrolysis under hydrogen environments present several advantages including i) lower pressure requirements when compared to hydrotreating (80 % less) [7,19], and ii) lower energy demand due to the process exothermicity [7].

Since 2010, experimental research efforts in this area have focused on developing continuous processes with conditions analogous to fast pyrolysis, with the main difference being the presence of a hydrogen atmosphere[22-27]. One of the obstacles for hydrogen assisted pyrolysis is the hydrogen requirement to maximize the hydrogenation of vapors. Hydrogen is an expensive material to supply from an outside source. Therefore, it is potentially more economical and efficient to produce hydrogen on site using readily available starting materials. In this chapter, the WGS kinetics were combined with the CFD pyrolysis model and HDO bio-oil chemistry to computationally model a one-pot biomass hydrous pyrolysis bubbling fluidized bed system.

4.2. Modeling approach

Our catalytic fast hydrous pyrolysis model incorporates the previous fast pyrolysis model developed using OpenFOAM, an open-source C++ software. The catalytic fast hydrous pyrolysis (CFHP) model uses the same modeling approach outlined in detail in Chapter 3, section 2. CFHP is simulated at temperatures from 300 to 500 °C, a pressure of 30 bar, and two different fluidization velocities. Furthermore, our boundary conditions (BC) remain largely unchanged from the fast pyrolysis simulations with changes only coming in reaction pressure, temperature, and fluidization gas composition. The reaction pressure is set at the reactor outlet BC to 30 bar from atmospheric. Based on hydropyrolysis, we assume that the reaction temperatures for CFHP are typically lower than that for fast pyrolysis, so the reaction temperature (wall and gas inlet BCs) are set to lower temperatures, 300-500 °C. Whereas our fast pyrolysis simulations used 100 % nitrogen as an inert fluidizing gas, we replaced nitrogen with steam (with 1% nitrogen) while maintaining the same fluidization velocities as the fast pyrolysis simulations. The two velocities used in the simulations correspond to the same velocities for the 3 and 4.5 Umf pyrolysis conditions. The biomass feedstock used is switchgrass with a 10% moisture content, see Chapter 3 for biomass composition.

4.2.1. Reaction scheme and kinetics

The hydrous pyrolysis maintains the same comprehensive pyrolysis reaction scheme used in Chapter 3, section 2.2. The reaction scheme and kinetics proceed through a first-order Arrhenius reaction rate that does not take pressure into account[28]. Previous studies have shown a hydrogen environment and moderate pressures do not greatly affect the composition of the bio-oil, and the decrease in overall yield is attributed to cracking reactions[29,30]. Therefore, it is assumed that the pyrolysis kinetics from Chapter 3 are applicable to the hydrous pyrolysis model. In Chapter 3, section 2.2, the individual components of biomass, i.e. cellulose, hemicellulose, ligninH, ligninC, and ligninO, undergo reactions to produce char, non-condensable gases (CO, CO_2, H_2, CH_4, C_2H_4), and bio-oil. The bio-oil is comprised of several different "model" bio-oil compounds, e.g. levoglucosan, glyoxal, and hydroxyl methyl furfural (HMFU). This work combines a comprehensive, detailed pyrolysis scheme with a global, lumped kinetic model for HDO. In order to incorporate the global, lumped model, the detailed pyrolysis compounds are summed into one "oil" species to undergo the HDO reactions. The hydrous pyrolysis simulation does not account for the secondary cracking kinetics that were in the fast pyrolysis simulations of Chapter 3 as it is hypothesized that in a one-pot process, cracking reactions are replaced by HDO reactions. By assuming the pyrolysis cracking reactions have a negligible impact on the overall reaction, the hydrous pyrolysis simulations will model ideal process conditions that minimize the occurrence of secondary cracking reactions and maximize the amount of pyrolysis oil produced. The oil will then undergo HDO reactions to produce light and heavy fractions of deoxygenated bio oil as well as more non-condensable gases and char.[31,32]

$$Oil + H_2 \xrightarrow{k_1} Light + H_2O$$

$$Oil + H_2 \xrightarrow{k_2} Heavy + H_2O$$

$$Oil + H_2 \xrightarrow{k_3} H_2O + Gas + Char$$

$$Heavy \xrightarrow{k_4} H_2O + Gas + Char$$

$$Heavy \xrightarrow{k_5} Light$$

The rate of these reactions is dependent on the concentration of the oil as well as the partial pressure of hydrogen.[33]

$$r = kC_{oil}P_{H_2}$$

$$k = k_0 e^{-\frac{E_a}{RT}}$$

Much of the kinetic work done on HDO of pyrolysis typically use highly empirical approaches.[34] The Arrhenius parameters adopted for this hydrous pyrolysis model, using a lumped kinetic model, are shown in Table 4.1.[31] The partial pressure and concentration of each gas species are related through the assumption of ideal gas behavior where the subscript i represents the chemical species index.

$$C_i = \frac{p_i}{RT}$$

The kinetics for hydrogen production through the WGS were determined to proceed via an empirical power law in Chapter 3. The model assumes an adequate amount of active catalyst is in the reactor so that the kinetics from a weight hourly space velocity (WHSV) of 1,220 $cm^3/(min\text{-}g_{cat})$ were adopted into the code (Chapter 2). WGS is a reversible reaction; therefore, the rate of

Table 4.1. Kinetic rate constant parameters for the lumped HDO scheme.[31]

Parameters	**k_1**	**k_2**	**k_3**	**k_4**	**k_5**
k_0	35.8	367	16.0	0.07	4180
E_a (kJ/mol)	64.8	75.4	66.3	27.9	97.1

hydrogen production is dependent on the partial pressure of each species involved in the reaction (CO, H_2O, H_2, and CO_2). The β term represents the approach to equilibrium.[35]

$$r = 1.424e^{-\frac{20.208}{RT}} P_{CO}^{1.029} P_{H_2O}^{0.634} P_{CO_2}^{-0.498} P_{H_2}^{-0.669} (1 - \beta)$$

$$\beta = \frac{P_{CO_2} P_{H_2}}{P_{CO} P_{H_2O}}$$

4.2.3. Simulation analysis

4.2.3.1. Hydrodynamics

In the original fast pyrolysis simulations (Chapter 3), the fluidization velocity and reactor temperature had a large effect on the elutriation and solid residence time distribution. CFHP simulations replace the fluidizing gas species as well as increase the reaction pressure from atmospheric to moderate hydrogen pressure (30 bar). The effects of these variable on the solid particle residence time (RTD) as well as velocity and temperature profiles were investigated.

4.2.3.2. Product distribution

The final bio-oil can be classified into three subgroups: deoxygenated light fraction oil, deoxygenated heavy fraction oil, and oxygenated pyrolysis oil (unreacted oil). Due to the use of a lumped kinetic model for HDO reactions, a detailed analysis of the bio-oil composition cannot be achieved directly. Analysis will also be done to visualize where in the reactors, HDO begins to occur.

The maximum bio-oil yield from the fast pyrolysis simulations with and without secondary cracking reactions was 47% and 55%, respectively. This chapter aims to determine the effects of hydrous pyrolysis conditions on the overall yield of bio-oil. The bio-oil will be comprised of deoxygenated oil (light and heavy fractions) as well as the bio-oil that did not undergo HDO.

Upgrading of pyrolysis vapors usually results in an overall reduction of liquid oil yield in exchange for a less oxygenated oil.[36] Bio-oil and non-condensable gas (NCG) yields will be determined from the mass fraction of each species leaving the top of the reactor with char being calculated by difference.

4.3. Results and discussion

Hydrous pyrolysis simulations were run on the Joint Institute of Computational Sciences (JICS) High-Performance Computer (HPC). Most cases have reached approximately seven seconds of simulation time. Biomass hydrous pyrolysis began to take place shortly after three seconds. The process did not reach steady-state, therefore the results reported here are from an unsteady-state. The effects of hydrous pyrolysis conditions on process hydrodynamics and product yields were investigated.

4.3.1. Hydrous pyrolysis hydrodynamics

To reduce the overall simulation time, the biomass particles for this chapter were simulated with an initial temperature just below the devolatilization point (390 K). There first few simulated seconds of the pyrolysis model is just heating the biomass from their initial temperatures to the devolatilization temperature. This change allows for the simulation to save a few seconds of simulated time and steady-state to be reached faster, however, it makes it more difficult to directly compare certain hydrodynamic properties such as particle residence time. An RTD for the 500 °C condition is shown in Figure 4.1. The residence time is significantly shorter than seen in the pyrolysis simulations at the same temperature and gas velocity. One of the causes for this, apart from the initial biomass temperature, is the difference in fluidizing gas upon heating. The density of steam is more variable at higher temperatures than that of nitrogen, which translates to the same superficial velocities equating to a higher Umf ratio. Figure 4.2 shows the void fraction for

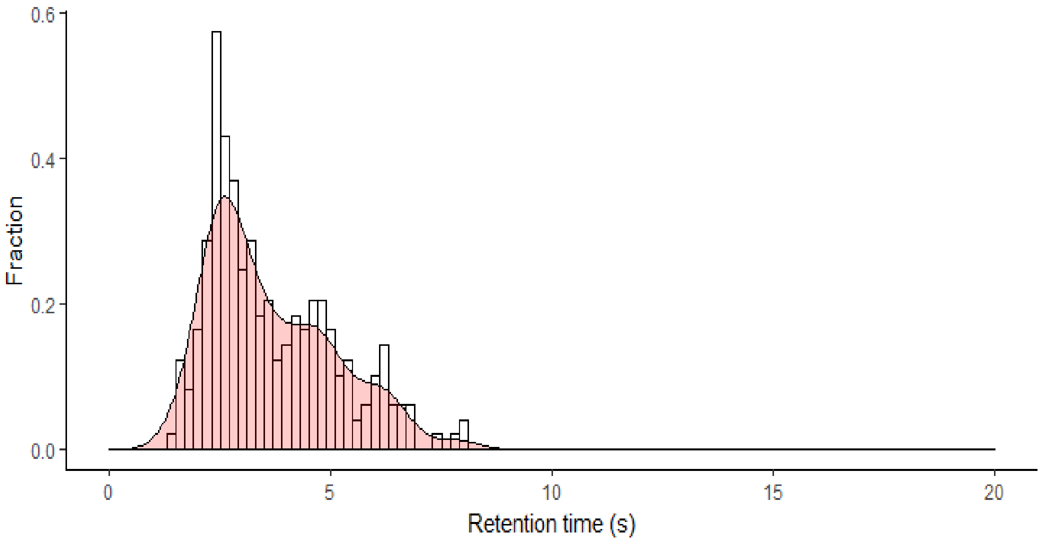

Figure 4.1. Residence time distribution for 500 °C at a velocity comparable to 3 Umf in pyrolysis.

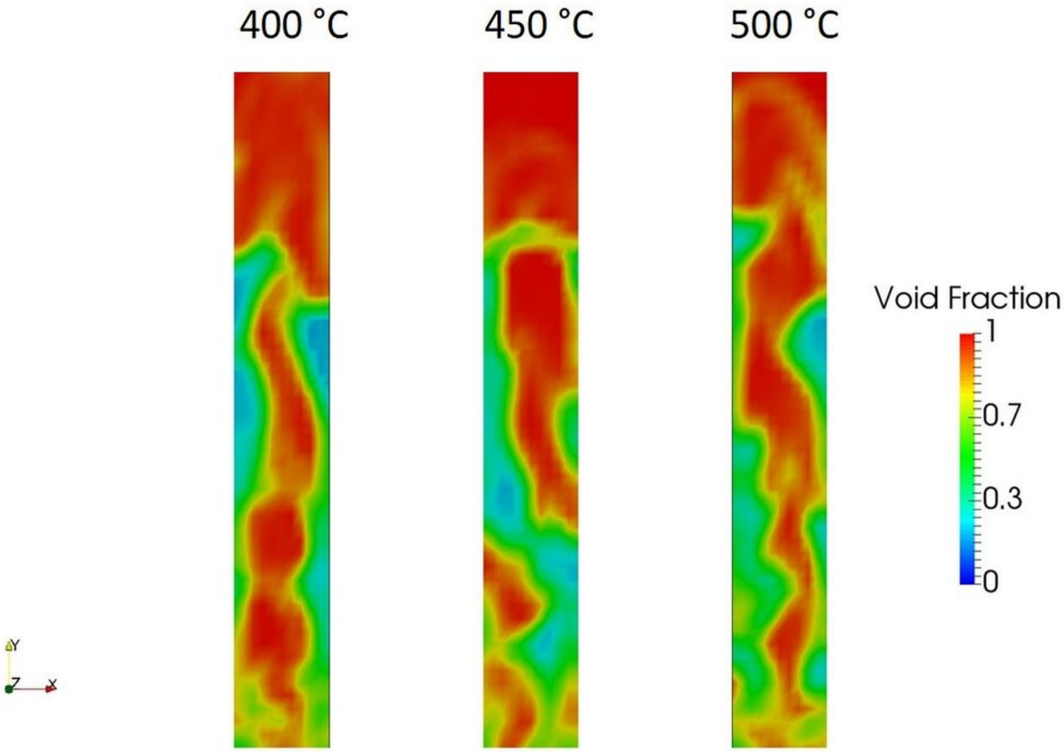

Figure 4.2. Void fraction for the bottom half of the reactor for 0.786 m/s at 30 bar.

conditions from 400 to 500 °C. Temperature does not appear to have a significant effect on the void fraction of the bed. One significant difference between the simulations is in the temperature profile of the gas phase between pyrolysis and hydrous pyrolysis. Figure 4.3 shows the temperature during hydrous pyrolysis is kept much more uniform inside the reactor than during pyrolysis and is not significantly affected by the vapors released during devolatilization.

4.3.2. Hydrous pyrolysis selectivity

An important aspect of hydrous pyrolysis, which is important for future optimization, is the selectivity of the process. The knowledge of which bio-oil compounds are more likely to be deoxygenated during hydrous pyrolysis can be very helpful in understanding the overall process. This work used a lumped kinetic scheme; therefore, the selectivity of the hydrous pyrolysis process can only be compared between two products: heavy oil and light oil. Due to the unsteady-state nature of the simulations, we must report on the trend of selectivity of HDO. The hydrogen selectivity is determined using the amount of hydrogen consumed to produce both light and heavy fractions. Based on the kinetics, the selectivity is of hydrogen in the HDO scheme significantly favors the heavy fraction over the light fraction.

4.3.3. Hydrous pyrolysis yields

Based on modeling assumptions, there are five main products in hydrous pyrolysis compared to the three main products in conventional fast pyrolysis. The oil is further broken down to oxygenated oil, heavy, and light fraction of deoxygenated oils. In Chapter 3, the highest bio-oil yield, without secondary cracking, was reported to be 54 wt. %. From previous upgrading work, we expect the overall liquid yield to decrease compared to fast pyrolysis due to coking of the catalyst, which negatively affects the catalytic pyrolysis process[19]. Hydrous pyrolysis simulations have only recently begun to

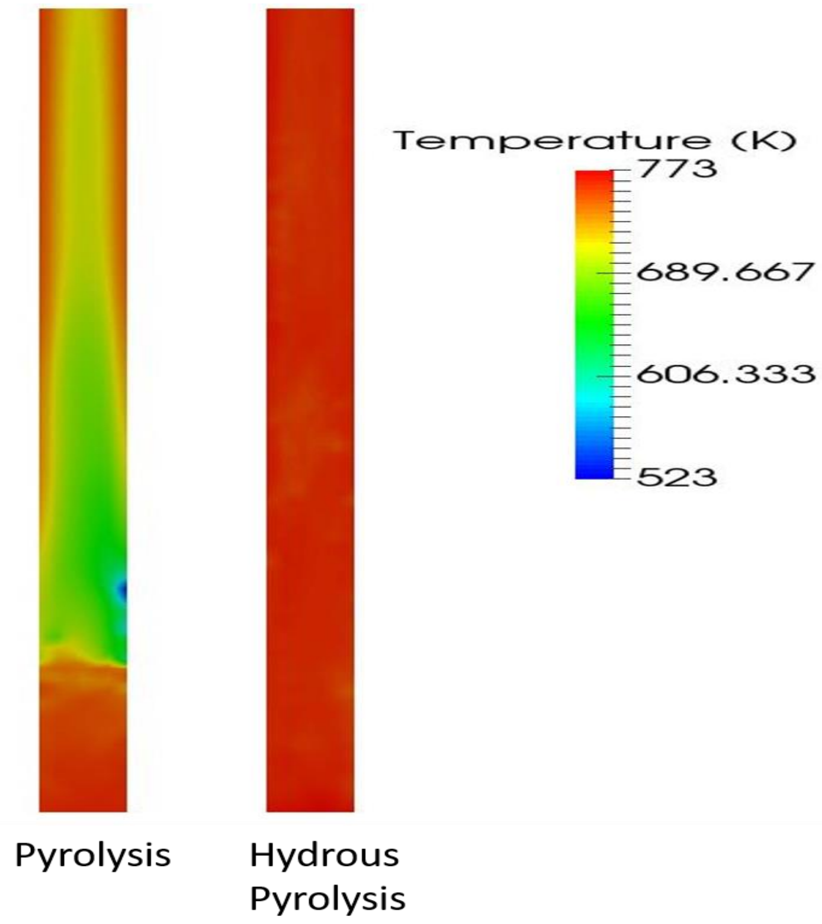

Figure 4.3. Comparison of temperature profile for the pyrolysis and hydrous pyrolysis case at 500 °C and 3 Umf.

undergo pyrolysis and the HDO. Therefore, there is no reportable data on the yield of the hydrous pyrolysis process. The vapor evolution of the oily products is shown in Figure 4.4. The “Oil” fraction is spotty compared to other evolution profiles. Due to the summation of pyrolysis vapors and the reactions just starting, the highest fraction peaks are where the most pyrolysis oil is being generated. As HDO reactions occur to produce light and heavy fractions, the compounds diffuse and spread out. The mass fraction of light and heavy fractions leaving the reactor is significantly less than the mass of the summed “Oil” (Figure 4.4). This indicates that the kinetics of the implemented HDO kinetics are not fast enough to deoxygenate a significant amount of the oil in the fluidized bed reactor at the simulated fluidization velocities.

4.4. Conclusions

Biomass fast pyrolysis is an attractive substitute for petroleum fuels. However, the bio-oil requires significant upgrading to be comparable in quality. Hydrous pyrolysis is a state-of-the-art process that combines pyrolysis, HDO, and the WGS into a one-pot solution to produce deoxygenated, refinery-ready bio-crude oil. The change in fluidizing gas from nitrogen to steam and the increase in operating pressure had a significant effect and predicted a more uniform temperature profile of the gas phase. Biomass particles’ elutriation began quicker than in conventional pyrolysis simulations. In the case of the 4.5 Umf simulations, biomass particles elutriated from the reactor before the significant devolatilization occurred, reducing the overall oil yield. The implemented HDO kinetics are not fast enough to adequate deoxygenate the bio-oil before leaving the reactor. Due to these short particle residence times, the overall yield of the hydrous pyrolysis simulations is significantly less than predicted from the pyrolysis simulations. Further simulation time and modifications to HDO kinetics is required before a decision can be made on the validity of the simulations.

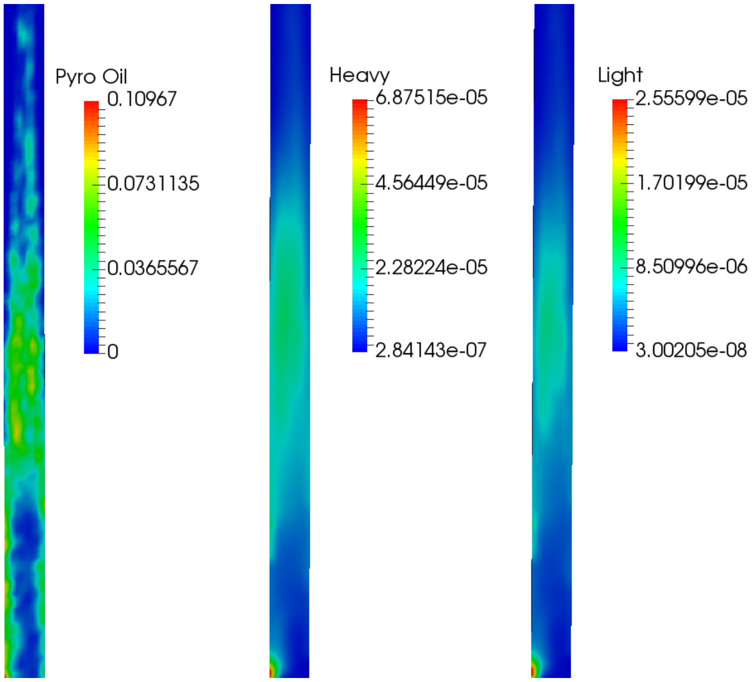

Figure 4.4. Mass fraction (per surface area) of summed oil, heavy fraction, and light fraction products for 450 °C and 3Umf at three seconds.

List of references

(1) Tan, E. C.; Marker, T. L.; Roberts, M. J. Direct production of gasoline and diesel fuels from biomass via integrated hydropyrolysis and hydroconversion process—A techno-economic analysis. *Environmental Progress & Sustainable Energy* **2014,** *33* (2), 609.
(2) Oasmaa, A.; Czernik, S. Fuel Oil Quality of Biomass Pyrolysis OilsState of the Art for the End Users. *Energy & Fuels* **1999,** *13* (4), 914.
(3) Dayton, D. C.; Carpenter, J.; Farmer, J.; Turk, B.; Gupta, R. Biomass Hydropyrolysis in a Pressurized Fluidized Bed Reactor. *Energy & Fuels* **2013,** *27* (7), 3778.
(4) Agblevor, F. A.; Beis, S.; Mante, O.; Abdoulmoumine, N. Fractional catalytic pyrolysis of hybrid poplar wood. *Industrial & Engineering Chemistry Research* **2010,** *49* (8), 3533.
(5) Bridgwater, A. V. Renewable fuels and chemicals by thermal processing of biomass. *Chemical Engineering Journal* **2003,** *91* (2), 87.
(6) Diebold, J. P. “A review of the chemical and physical mechanisms of the storage stability of fast pyrolysis bio-oils,” National Renewable Energy Lab., Golden, CO (US), 1999.
(7) Marker, T. L.; Felix, L. G.; Linck, M. B.; Roberts, M. J. Integrated hydropyrolysis and hydroconversion (IH2) for the direct production of gasoline and diesel fuels or blending components from biomass, part 1: Proof of principle testing. *Environmental Progress & Sustainable Energy* **2012,** *31* (2), 191.
(8) French, R.; Czernik, S. Catalytic pyrolysis of biomass for biofuels production. *Fuel Processing Technology* **2010,** *91* (1), 25.
(9) Mullen, C. A.; Boateng, A. A. Catalytic pyrolysis-GC/MS of lignin from several sources. *Fuel Processing Technology* **2010,** *91* (11), 1446.
(10) Agblevor, F. A.; Mante, O.; Abdoulmoumine, N.; McClung, R. Production of stable biomass pyrolysis oils using fractional catalytic pyrolysis. *Energy & Fuels* **2010,** *24* (7), 4087.
(11) Thangalazhy-Gopakumar, S.; Adhikari, S.; Gupta, R. B.; Tu, M.; Taylor, S. Production of hydrocarbon fuels from biomass using catalytic pyrolysis under helium and hydrogen environments. *Bioresource Technology* **2011,** *102* (12), 6742.
(12) Elliott, D. C. Historical Developments in Hydroprocessing Bio-oils. *Energy & Fuels* **2007,** *21* (3), 1792.
(13) Huber, G. W.; Iborra, S.; Corma, A. Synthesis of transportation fuels from biomass: chemistry, catalysts, and engineering. *Chemical reviews* **2006,** *106* (9), 4044.
(14) Thangalazhy-Gopakumar, S.; Adhikari, S.; Gupta, R. B. Catalytic pyrolysis of biomass over H+ ZSM-5 under hydrogen pressure. *Energy & Fuels* **2012,** *26* (8), 5300.
(15) Bridgwater, A. Production of high grade fuels and chemicals from catalytic pyrolysis of biomass. *Catalysis Today* **1996,** *29* (1-4), 285.
(16) Snape, C.; Bolton, C.; Dosch, R.; Stephens, H. P. High liquid yields from bituminous coal via hydropyrolysis with dispersed catalysts. *Energy & Fuels* **1989,** *3* (3), 421.
(17) Canel, M.; Mısırlıogˇlu, Z.; Sınagˇ, A. Hydropyrolysis of a Turkish lignite (Tunçbilek) and effect of temperature and pressure on product distribution. *Energy Conversion and Management* **2005,** *46* (13), 2185.
(18) Steinberg, M. The flash hydropyrolysis and methanolysis of coal with hydrogen and methane. *International Journal of Hydrogen Energy* **1987,** *12* (4), 251.
(19) Marker, T. L.; Felix, L. G.; Linck, M. B.; Roberts, M. J.; Ortiz-Toral, P.; Wangerow, J. Integrated hydropyrolysis and hydroconversion (IH2®) for the direct production of gasoline and diesel fuels or blending components from biomass, part 2: Continuous testing. *Environmental Progress & Sustainable Energy* **2014,** *33* (3), 762.

(20) Wang, K.; Dayton, D. C.; Peters, J. E.; Mante, O. D. Reactive catalytic fast pyrolysis of biomass to produce high-quality bio-crude. *Green Chemistry* **2017**.

(21) Melligan, F.; Hayes, M. H. B.; Kwapinski, W.; Leahy, J. J. A study of hydrogen pressure during hydropyrolysis of Miscanthus x giganteus and online catalytic vapour upgrading with Ni on ZSM-5. *Journal of Analytical and Applied Pyrolysis* **2013,** *103* (Supplement C), 369.

(22) Resende, F. L. P. Recent advances on fast hydropyrolysis of biomass. *Catalysis Today* **2016,** *269* (Supplement C), 148.

(23) Balagurumurthy, B.; Bhaskar, T. Hydropyrolysis of lignocellulosic biomass: state of the art review. *Biomass Conversion and Biorefinery* **2014,** *4* (1), 67.

(24) Balagurumurthy, B.; Oza, T. S.; Bhaskar, T.; Adhikari, D. K. Renewable hydrocarbons through biomass hydropyrolysis process: challenges and opportunities. *Journal of Material Cycles and Waste Management* **2013,** *15* (1), 9.

(25) Stummann, M. Z.; Høj, M.; Schandel, C. B.; Hansen, A. B.; Wiwel, P.; Gabrielsen, J.; Jensen, P. A.; Jensen, A. D. Hydrogen assisted catalytic biomass pyrolysis. Effect of temperature and pressure. *Biomass and Bioenergy* **2018,** *115*, 97.

(26) He, S.; Boom, J.; van der Gaast, R.; Seshan, K. Hydro-pyrolysis of lignocellulosic biomass over alumina supported Platinum, Mo2C and WC catalysts. *Frontiers of Chemical Science and Engineering* **2018,** *12* (1), 155.

(27) Gamliel, D. P.; Bollas, G. M.; Valla, J. A. Two-stage catalytic fast hydropyrolysis of biomass for the production of drop-in biofuel. *Fuel* **2018,** *216*, 160.

(28) Corbetta, M. P., S.; Ranzi, E.; Bennadji, H.; Fisher, E. M. XXXVI Meeting of the Italian Section of the Combustion Institute, 2013.

(29) Resende, F. L. P. Recent advances on fast hydropyrolysis of biomass. *Catalysis Today* **2016,** *269*, 148.

(30) Venkatakrishnan, V. K.; Degenstein, J. C.; Smeltz, A. D.; Delgass, W. N.; Agrawal, R.; Ribeiro, F. H. High-pressure fast-pyrolysis, fast-hydropyrolysis and catalytic hydrodeoxygenation of cellulose: production of liquid fuel from biomass. *Green Chemistry* **2014,** *16* (2), 792.

(31) Zhang, S.; Yan, Y.; Li, T.; Ren, Z. Lumping Kinetic Model for Hydrotreating of Bio-oil from the Fast Pyrolysis of Biomass. *Energy Sources, Part A: Recovery, Utilization, and Environmental Effects* **2009,** *31* (8), 639.

(32) Bridgwater, A. V. Production of high grade fuels and chemicals from catalytic pyrolysis of biomass. *Catalysis Today* **1996,** *29* (1), 285.

(33) Bykova, M. V.; Zavarukhin, S. G.; Trusov, L. I.; Yakovlev, V. A. Guaiacol hydrodeoxygenation kinetics with catalyst deactivation taken into consideration. *Kinetics and Catalysis* **2013,** *54* (1), 40.

(34) Chaudhari, R. V.; Torres, A.; Jin, X.; Subramaniam, B. Multiphase Catalytic Hydrogenolysis/Hydrodeoxygenation Processes for Chemicals from Renewable Feedstocks: Kinetics, Mechanism, and Reaction Engineering. *Industrial & Engineering Chemistry Research* **2013,** *52* (44), 15226.

(35) Ayastuy, J. L.; Gutiérrez-Ortiz, M. A.; González-Marcos, J. A.; Aranzabal, A.; González-Velasco, J. R. Kinetics of the Low-Temperature WGS Reaction over a CuO/ZnO/Al2O3 Catalyst. *Industrial & Engineering Chemistry Research* **2005,** *44* (1), 41.

(36) Marker, T. L.; Felix, L. G.; Linck, M. B.; Roberts, M. J. Integrated hydropyrolysis and hydroconversion (IH2®) for the direct production of gasoline and diesel fuels or blending

components from biomass, part 1: Proof of principle testing. *Environmental Progress & Sustainable Energy* **2012,** *31* (2), 191.

CONCLUSION AND FUTURE WORK

This research developed a computational fluid dynamics model to simulate biomass hydrous pyrolysis in a bubbling fluidized bed reactor. Hydrous pyrolysis combines biomass fast pyrolysis with hydrodeoxygenation for upgrading and the water-gas shift for hydrogren generation. Hydrous pyrolysis has the potential to be a single reactor solution to producing a drop-in bio-crude replacement to petroleum fuels. The overall goal was broken down and achieved through three objectives. The first consisted of deriving experimental water-gas shift kinetics over a commercial catalyst at operating conditions close to hydrous pyrolysis. A Langmuir-Hinshelwood model and an empirical power law model provided the best first to the experimental data. In the power law, as the catalyst weight was increased, the overall conversion increased and the activation energy required decreased. The power law was adopted for the subsequent objectives.

The second objective consisted of developing a computational fluid dynamics model for conventional biomass fast pyrolysis in a bubbling fluidized bed reactor. The model adopted an Eulerian-Lagrangian approach for individual particle tracking as well as a comprehensive kinetic scheme for pyrolysis. Simulations were carried out from 450 to 550 °C and at three fluidization velocities (1.91, 3, and 4.5 Umf). The fluidization velocity had a significant effect on biomass particle residence time and particle elutriation. The largest bio-oil yield, with and without secondary cracking, was 47 and 54 wt. %, respectively. The water content in the bio-oil was significantly lower than the 20-25 wt. % seen from experimental pyrolysis regardless if the secondary cracking reactions were incorporated into the simulation or not. Further work needs to be done on the kinetics of the secondary cracking reactions to account to produce more water.

The third and final objective consisted of combining the work from the previous two objectives to create a model for biomass hydrous pyrolysis. The change of fluidizing gas from nitrogen to steam as well as the increased reactor pressure in the hydrous pyrolysis simulations influenced the temperature profile as well as particle dynamics. These changes caused the particles to elutriate much faster than in the fast pyrolysis simulations while using the same superficial gas velocity. The quicker elutriation reduced the overall yield of bio-oil due to the lack of devolatilization. The selectivity of hydrogen significantly favored the production of the heavy fraction over the light fraction (90 %) in the HDO scheme. The pyrolysis vapors did not undergo significant amounts of deoxygenation before leaving the reactor; therefore, the HDO kinetics are assumed to be too slow to significantly deoxygenate the pyrolysis vapors. Without the simulations being completed, we cannot determine if the hydrous pyrolysis model is adequate to simulate the one-step pyrolysis and deoxygenation of bio-oil.

Overall, this is a good first step towards modeling and understanding the hydrous pyrolysis process. However, there is still significant work needed in this area to accurately model biomass hydrous pyrolysis. The kinetics of the HDO scheme have been altered to increase the speed of deoxygenation reactions to determine the effect of the new kinetics. Moving forward, experimental work will be performed to develop individual HDO kinetics for the model compounds of the comprehensive pyrolysis scheme and remove the model’s dependence on a global, lumped HDO model. Additionally, the simulations assume all biomass particles have a uniform particle size. Simulations will be carried out using different particle sizes, with differing physical properties, as well as hopefully incorporating a particle size distribution.

VITA

Ross Houston was born in Sweetwater, TN on August 17, 1993. He graduated with a Bachelor of Science in Chemical Engineering from The University of Alabama in December of 2015 with Summa Cum Laude honors. He is currently finishing his Master of Science degree at The University of Tennessee, Knoxville in the Biosystems Engineering Program and plans to graduate in August 2018.